THE PRODUCTION OF HYPERON ANTIHYPERON PAIRS IN THE INTERACTIONS OF FAST ANTIPROTONS WITH PROTONS

by

D. H. Miller

A Thesis presented

for the

Degree of Doctor of Philosophy

University of London

Department of Physics,
Imperial College,
London.S.W.7.

September, 1963.

CONTENTS

ABSTRACT

In this thesis complete results are presented on the production of hyperon antihyperon pairs in the interactions of fast antiprotons within a hydrogen bubble chamber.

The thesis is in the chronological order in which the experiment took place. The setting up of the beam and the bubble chamber operation was common to all groups. The following chapters on Scanning, measuring and analysis, refer to work carried out by the author, or under his direct supervision. The final results are those combined from all groups, the interpretation of these results coming in the main from discussion amongst the collaborating physicists.

Definitions of the terms used can be found in Appendix 3.

PREFACE

The work presented in this thesis was undertaken by the author whilst a member of the bubble chamber film analysis group of Imperial College under the direction of Professor C. C. Butler.

The experiment represents an extension of work completed elsewhere at lower energies and an extension of our knowledge of elementary particle interactions. The 81 cm hydrogen bubble chamber built at Saclay, was exposed to a high energy separated beam of antiprotons ($\bar{p}$'s) from the CERN Proton Synchrotron. The beam being designed and laid down at CERN in 1961.

The author was one of a team of physicists responsible for optimizing this beam and bringing into commission the large electrostatic separator needed. During the operation of the experiment the same team was responsible for control of the beam and the chamber.

Approximately 100,000 pictures were taken at each of three momenta 3, 3·6 and 4 Gev/c. These were divided among five groups at Birmingham, CERN, Ecole Polytechnique, Imperial College and Saclay in order to study strange particle production.

The first analysis has been on hyperon, antihyperon production and partial results have been published. The results presented here represent the combined data from the five groups; the experimental techniques described are those which have been used by this group.

The film analysed at Imperial College consisted of equal amounts at 3·6 and 4 Gev/c. The author was responsible for the analysis and book-keeping of the 3·6 Gev/c film, S. Borenstein acting in a similar capacity for the 4 Gev/c film. The author's particular interest was in hyperon antihyperon pair production and results have been combined for all energies.

The final results will be presented at the Sienna Conference, September 1963, and published in Nuovo Cimento.

CHAPTER I

HISTORICAL BACKGROUND AND DESCRIPTION OF THE BEAM AND CHAMBER OPERATION

1.1 Introduction

The existence of antiparticles was first predicted as a consequence of Dirac's theory of the electron and its natural extension to other particles.

At the present time an antiparticle has been observed for nearly all known particles and it is expected that this symmetry holds completely. Appendix 1 shows the relationship between the properties of a particle and its antiparticle, in general these have been predicted theoretically and observed experimentally.

When a particle and its antiparticle interact annihilation can occur. This can be thought of as a 'ball' of energy left by the annihilation which can break up into any final state obeying the conservation laws of elementary particle interactions. This type of interaction, in general leaving a final state of only mesons, is the most common at the energies so far explored.

The interactions to be discussed however, are those which are in the main peripheral. Within this category we will discuss those interactions of the type $\bar{p} + p \rightarrow H + \bar{H} + n\pi$. where H is a hyperon and $\bar{H}$ is an antihyperon not necessarily of the same type as H. Appendix 2 lists for the energy available in this experiment the interactions possible in this class.

FIG 1·1

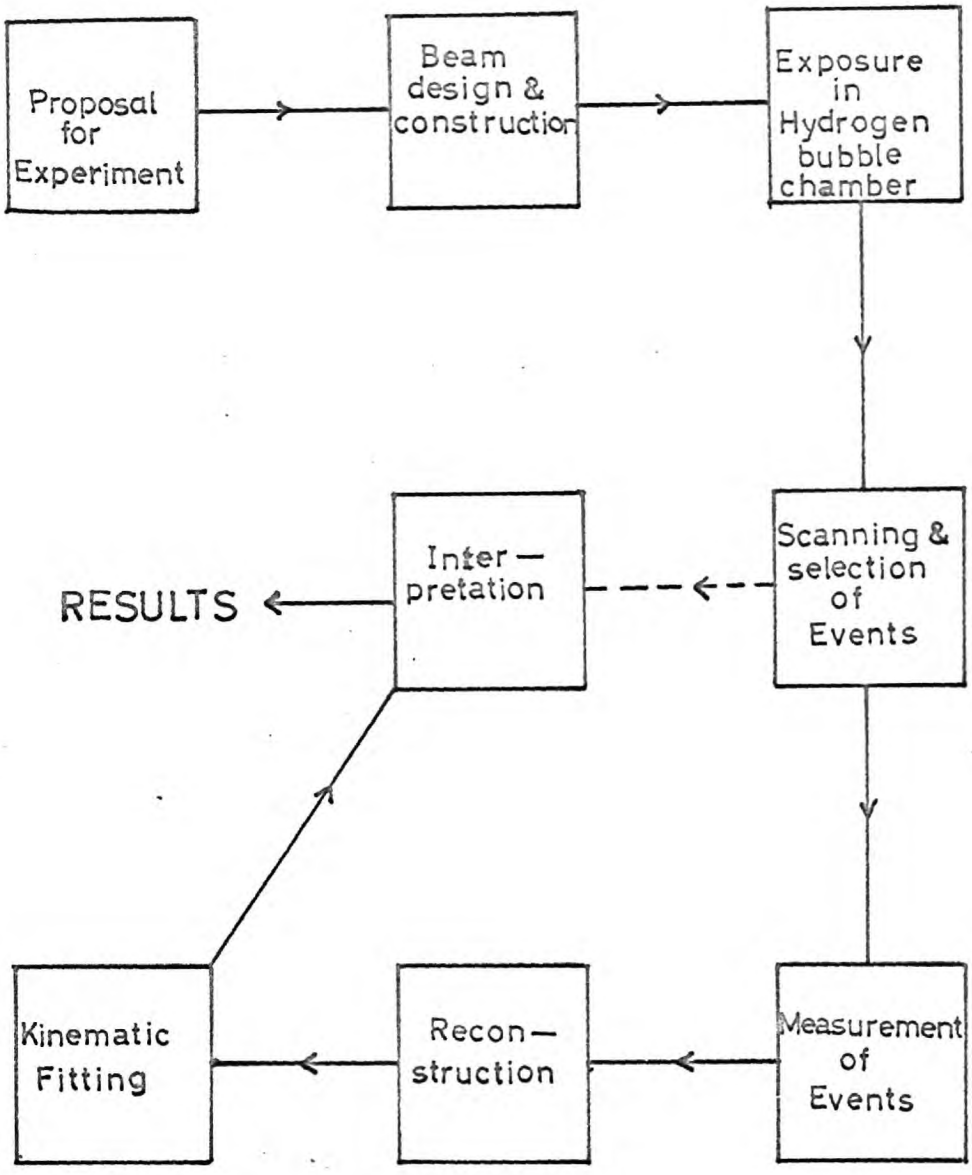

FLOW DIAGRAM OF A TYPICAL BUBBLE CHAMBER EXPERIMENT

Figure 1.1 shows a flow diagram of a typical bubble chamber experiment which has been closely followed in this experiment and as far as possible each section will be dealt with in chronological order.

1.2 Historical Background

The properties of antiprotons have been studied only since the advent of large accelerators. Their existence had been predicted but until the Bevatron came into operation in 1955 they had not definitely been observed.

Using time of flight techniques Chamberlain et al[1] were able to show the existence of antiprotons in a beam of negative particles from the Bevatron. During the years following some experiments were done using beams of negative particles usually containing less than one per cent antiprotons. These were sufficient to determine some gross features of antiproton interactions and to confirm some of it's properties (e.g. its mass). Very little could be done to study its detailed properties until larger accelerators were built to increase the flux of antiprotons and methods could be found to separate these from a large background of Pi-minus mesons.

There was, however, one very good bubble chamber run with an antiproton beam at the Bevatron in 1959[2]. This was the first experiment utilizing the seventy two inch hydrogen bubble chamber built by Alvarez and his associates. The most important results from

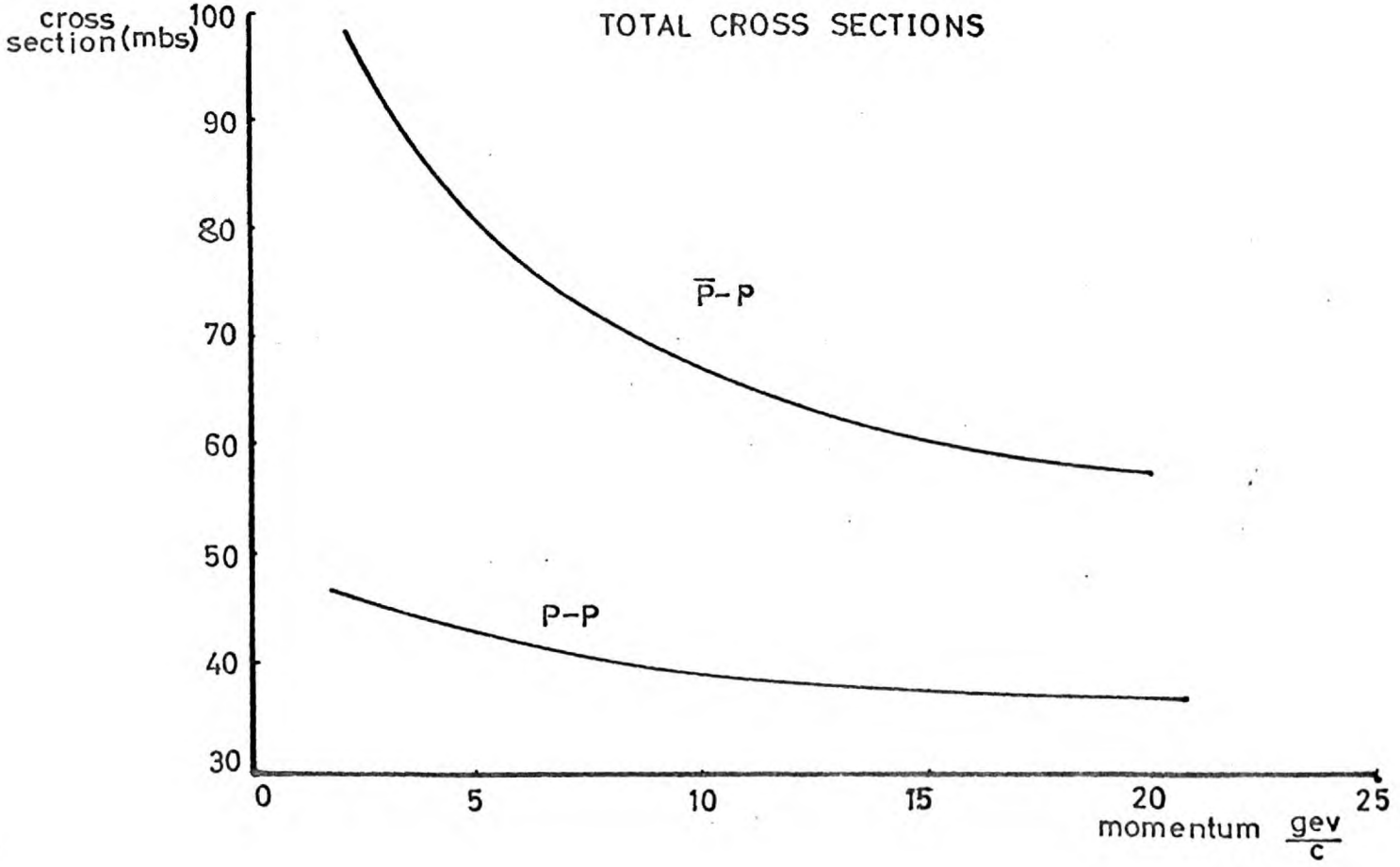
TOTAL CROSS SECTIONS
cross section (mbs)
100
90
80
70
60
50
40
30
0
5
10
15
20
25
momentum gev/c
$\bar{P}$-P
P-P

FIG 1.2

this run were obtained from the annihilation events, e.g. the discovery of the ρ and ω particles. Very few examples of hyperon antihyperon pair production were observed there being only eleven events of the class $\bar{p} + p \longrightarrow \Lambda + \bar{\Lambda}$. The total cross-section is the only property which has been determined over a wide energy range[3] (using counter techniques). Figure 1.2 shows the total cross-section for $\bar{p} + p$ from 0 $\longrightarrow$ 20 Gev/c. The cross-section for $p + p$ is also shown, being much lower than that for $\bar{p} + p$ even at the higher momentum.

1.3 Recent Developments

With the coming into operation of the CERN Proton Synchrotron at Geneva and coupled with this the construction of large electrostatic separators, it became clear that beams containing a large percentage of antiprotons were feasible.

The first such beam (not utilizing electrostatic separators) was used to study the interactions at rest of antiprotons with protons[4]. This was done by extracting a low momentum beam from the CERN P.S. and degrading the energy of the antiprotons so that at the entry point to the bubble chamber used, their momentum was not enough to carry them through the chamber. This experiment was below the threshold for hyperon production and therefore cannot be compared with the one under discussion.

The second experiment followed a proposal to study all aspects

of antiproton interactions in a hydrogen bubble chamber in a momentum range around 3 Gev/c. In particular the five groups, Birmingham, CERN, Ecole Polytechnique (Paris), Saclay and Imperial College would study the strange particle production. It was hoped that the reaction

$$\bar{p} + p \longrightarrow \bar{\Xi}^- + \bar{\bar{\Xi}}^{=}$$

would have a high enough cross-section so that useful statistics could be obtained (at this time the $\bar{\bar{\Xi}}^{=}$ had not been observed).

1.4 Beam Design

The beam (designated the symbol m_7 by the CERN Committee) was designed by S van de Meer[5]. It was a single stage separated beam suitable for antiprotons up to a momentum of 4 Gev/c or with slight modifications Pi plus or minus mesons up to 6 Gev/c. The latter beam due to the enormous flux of $\pi^{\pm}$ available was designed to have a very small momentum spread ($<$ 1%). The length of the beam was approximately one hundred and twenty metres and this made it unsuitable for providing beams of short lived particles e.g. $K^{\pm}$. Figure 1.3 shows a schematic diagram of the beam as it was used in this experiment.

An unfortunate feature of the beam was that it collected particles emitted at rather a large angle to the circulating beam of the P S. At the energy of the circulating protons (normally 20 Gev) the production of secondary particles after the beam has collided with a

Fig. 1·3

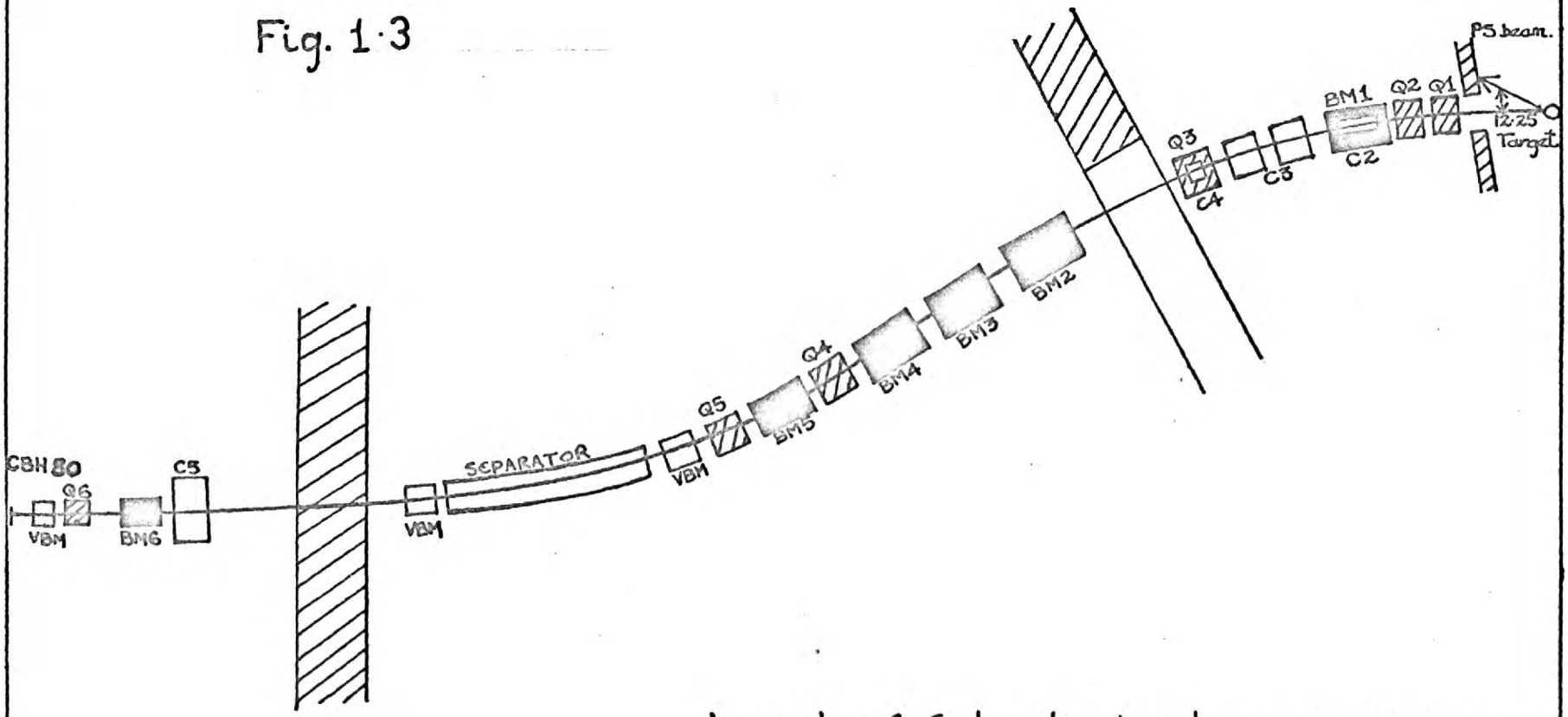

Lay-out of fast antiproton beam – CERN Geneva.

target is very strongly collimated in the forward direction. The flux of particles emitted falls off rapidly as the angle to the circulating beam increases. This caused some difficulty during the running of the experiment as any loss in the intensity of the P.S. beam decreased the flux of antiprotons to below the desired level. The reason for this large angle was shortage of experimental areas at CERN and consequently several beams were being fed from the same target area.

1.5 Detailed description of Beam

The quadrupoles Q_1 and Q_2 were used to accept and focus as large a cone of particles as possible. These then passed through the bending magnet BM1 which provided the initial momentum analysis. The collimator C3 was then used to select a narrow band of particles having a small spread in momentum around the value wanted. The beam equipment between C3 and the separator was used to further momentum analyse and collimate the beam. One horizontal focus was necessary between BM1 and BM2 in order that the dispersion produced by the former could be compensated by the dispersion produced in BM2 $\longrightarrow$ 5.

The separator consisted of two large polished plates in a vacuum tank between which an electric gradient of 50 kV/cm was maintained. The beam up to this point contained a mixture of antiprotons and Pi mesons; as it passed through the separator each of these components experienced different forces acting on them.

A particle entering an electric field starts to move in a parabolic orbit, the deflection y after moving a distance z being

$$y = - \frac{e}{2m} F \left(\frac{z}{v}\right)^2 = - e \frac{F z^2 m}{2p^2}$$

(for a definition of terms see Appendix 3).

In the case under consideration all particles in the beam have the same P, therefore, the deflection is proportional to the different masses. The separator was fifteen metres long and this produced a separation between the main peaks of antiprotons and background of 20 mm. A lead collimator was the next element of the beam; this was placed so as to accept as high a proportion as possible of antiprotons while absorbing as much as possible of the background. The purified beam passing through the collimator was then directed into the 81 cm hydrogen bubble chamber built at Saclay by R Florent et al[6] and run jointly by Saclay and Ecole Polytechnique.

The beam entering the chamber was only about 85% pure, the remaining 15% being mainly μ mesons coming from the reactions

$$\pi^- \longrightarrow \mu^- + \nu \ .$$

These μ mesons make the angular spread of the beam before and after the separator larger than it would be if the original pi mesons had not decayed. This causes the separation not to be as clean as one would desire, the image of the beam at the mass slit being as shown in Figure 1.4.

FIG 1·4

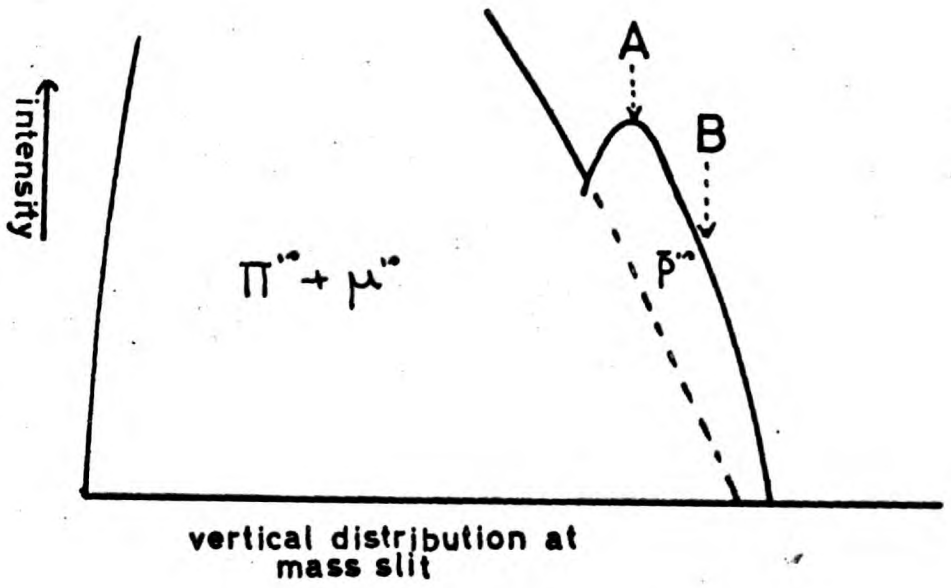
A
B
intensity
$\pi^- + \mu^-$
$\bar{p}^-$
vertical distribution at
mass slit


beam
separator
mass slit

During the initial runs at momenta of 3 and 3·6 Gev/c only 50% of the P.S. beam was being used to provide antiprotons and it was necessary to have the mass slit at the point A in order to get sufficient intensity of antiprotons into the chamber. At 4 Gev/c, however, although the separation of the two peaks was less, 100% of the P.S. beam was being used and it was possible to have the slit at the point B in order to have the same intensity in the chamber. The contamination at 4 Gev/c was therefore, less than at the other momenta even though the separation was less.

1.6 Experimental techniques used to set up beam

Originally while the beam was being designed nominal currents for all the elements were calculated using a tracking and matching programme[7]. Due to fluctuations in construction of beam elements and approximations used in the programme these are accurate only to a few per cent.

An experimental technique was used after the beam had been set up to check these nominal values and to improve upon them. This consisted of passing a current carrying wire into each beam element, this situation being a strict analogy of a beam of particles passing through the field.

Consider an element of this field carrying a current i (amps) and under tension T (dynes). If the wire is in equilibrium $B\rho = 10T/i$. The path of a particle of momentum P(Gev/c) entering the magnetic field with the same initial direction as the wire is an arc of a circle whose

radius is given by

$$P = {}^{P \times 10^6}/_{300H}$$

therefore if ${}^{3T}/_{i} = P \times 10^3$ the trajectory of the particle and wire are identical. If the momentum required is known wire measurements can check the path of the particles all along the beam. Extraneous forces do affect the wire thus spoiling complete accuracy; some of these are, gravitation, proximity to pole faces and convection currents due to heating.

The final technique used is to look with counters at each part of the beam to see that foci etc. are in the correct positions and to optimize the flux of wanted particles. Approximately a month was spent on the m1 using scintillation counters to optimize the beam. In particular the sizes of all the collimators were adjusted to give the highest possible purity of beam together with the smallest possible momentum spread.

By far the most difficult piece of equipment to bring into commission was the electrostatic separator, although more time was available for this as it was only needed during the run and not in optimizing the beam.

The electric field between the plates of the separator had to be very stable as any fluctuation would spoil the trajectory of the beam. In general only two effects spoilt stability, one being a continuous discharge, the other intermittent sparks. The former was very serious

as at each end of the discharge the plates could become permanently damaged. This would mean either running at a lower electric field or in repolishing the plates (a major task). During the experiment only intermittent sparks occurred these being kept down to a rate of about two per hour, with an intensity of 50 kV/cm.

1.7 Control of the Experiment

The values of the currents for all the elements previously determined by the above analysis were automatically monitored during the actual run. The operating conditions of the P.S. changed from time to time, particularly the position of the target. When such changes did occur it was necessary to alter the currents to maintain optimization.

Apart from this the other most important facet of the run was to maintain the quality of the [redacted] PICTURES. The bubble chamber [redacted] was run by a group of technicians with a physicist in overall charge but the responsibility for informing the chamber crew of changes needed lay with a small group of physicists who examined test strips from each roll of film as it came from the chamber. [redacted] The last 10 frames of each roll were developed and scanned for the following things:

(a) Illumination system working correctly.

(b) Number of bubbles/cm was approximately 16 for a beam track.

(c) Fiducial marks could be clearly seen.

(d) Number of interactions compatible with the known cross-sections for

antiprotons.

(e) Number of particles/frame about 12.

(f) Frame numbers could be clearly seen and were being increased by one each frame.

(g) Spacing of frames was constant.

(h) Number of delta rays compatible with incident antiprotons.

(i) Spatial distribution of beams in chamber correct.

As well as this a constant check was kept on the magnetic field and also by visual inspection of the illuminated chamber a watch was kept for possible failure of flash tubes. Polaroid pictures were also taken frequently to check on the number of beam tracks etc.

During the period January to April 1962, over 100,000 pictures were taken at each of three momenta, 3, 3·6 and 4 Gev/c. This film, containing approximately three million antiproton tracks, was divided equally among the five groups, each group in general having film from two of the three momenta.

A small portion of the film was given to another collaboration who were to study the more common processes of charge exchange and elastic scattering[8].

CHAPTER 2

SCANNING

The scanning of the film was a very important part of the experiment as a whole and it can be conveniently split up into the following sub-divisions.

(a) To find and classify all events of the types to be studied.

(b) To calculate the efficiencies of observing these types.

(c) To record the total number of beam tracks on the film.

(d) To calculate the purity of the beam, i.e. the ratio of antiprotons to unwanted particles present.

In order to calculate all these quantities the film was scanned three times.

2.1 General Information available at the Scanning Table

(a) Ionization

The number of bubbles/cm formed by the passage of a charged particle through liquid hydrogen is proportional to E^2/p^2; in the case of a bubble chamber the operating conditions affect this number as well.

The curves showing relative bubble density versus momentum are shown in Figure 2.1 for the four most common particles in this experiment. Above about 1·8 Gev/c it is seen that one can no longer distinguish between these particles. The number of bubbles/cm above this is constant

FIG 2·1
RANGE VERSUS MOMENTUM

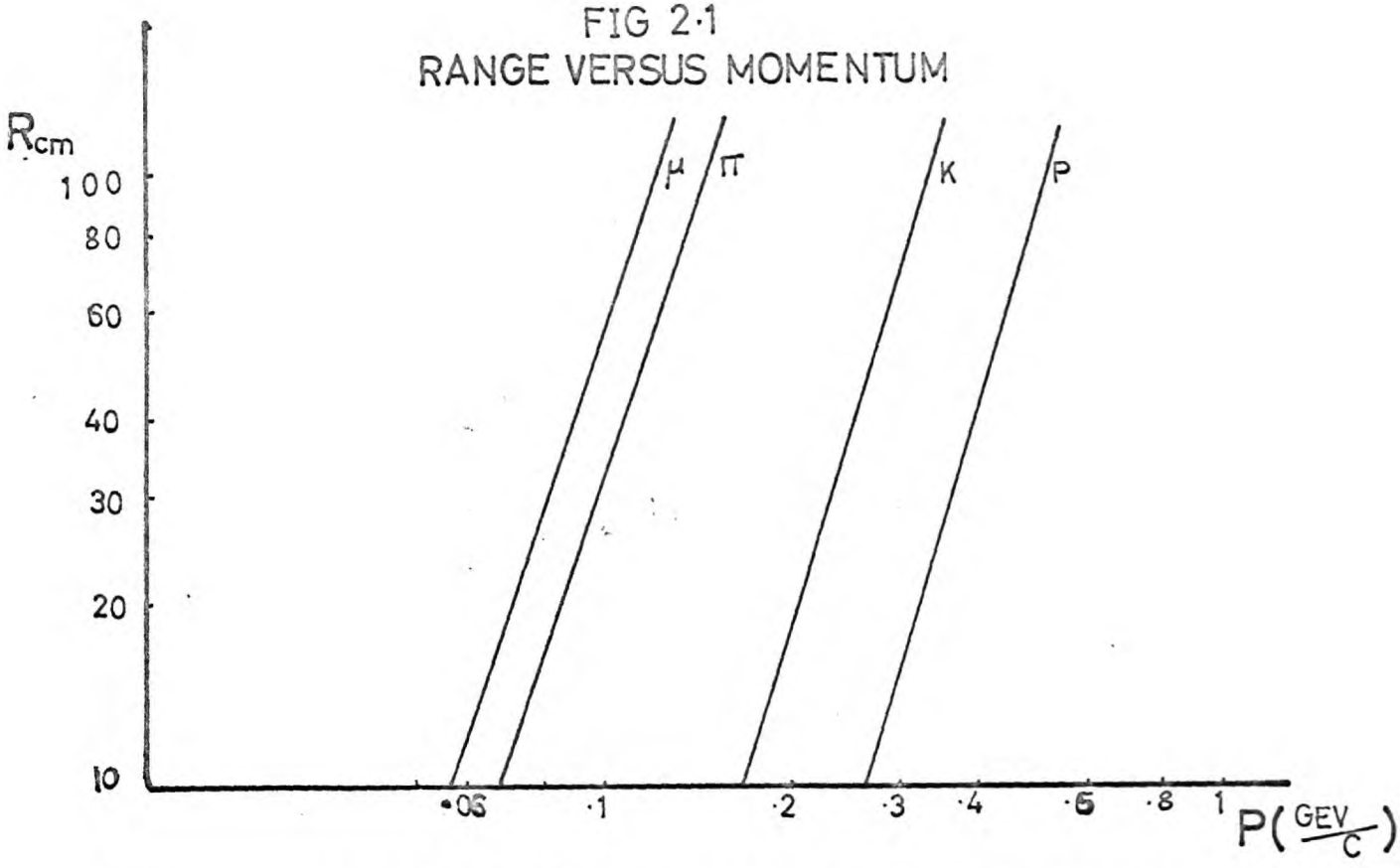

RELATIVE IONIZATION VERSUS MOMENTUM

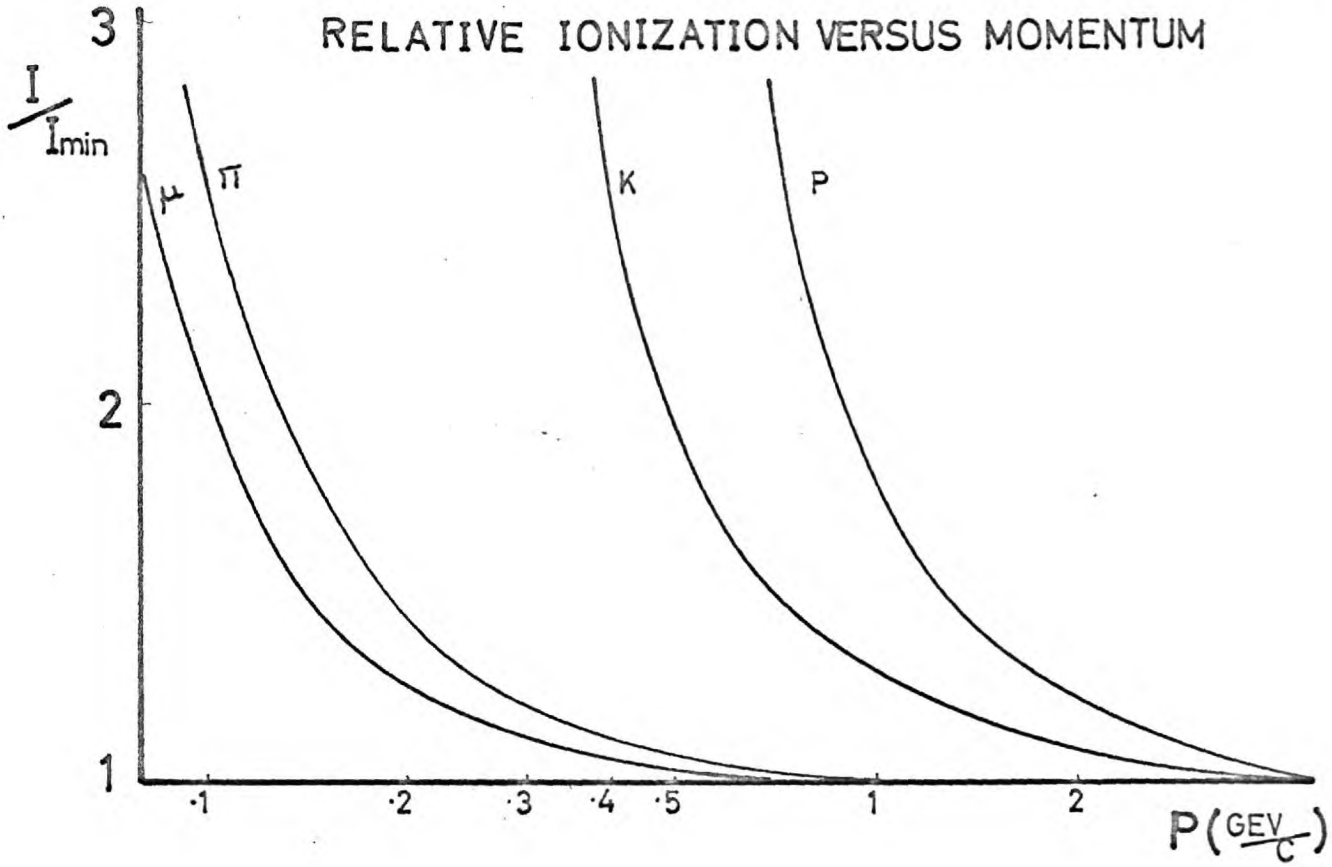

and this condition is known as minimum ionization.

In general it is safe to assume that when a particle has an ionization (number of bubbles/cm) twice minimum, one can see on the scanning table that it is above minimum. The dependence on chamber conditions is nullified by comparing the track in question with a beam track on the same frame.

(b) Range

The range of a singly charged particle in hydrogen is proportional to $mF(p/m)$ [9] the curves showing this dependence being shown in Figure 2.1. This can be used in two ways; for a track which terminates in the chamber a measurement of its curvature and length will determine the mass of the particle which left it, or for a track which terminates at a chamber wall a measurement of its length and curvature may put restrictions on what the mass of the particle which left the track could have been.

2.2 Scanning Procedure

It had been decided by the collaborating groups to scan for all events exhibiting one or more decays. It was further decided to sub-divide these events as far as possible into two classes, one containing decays positively identified as K mesons, the other containing possible hyperon decays. Events were noted irrespective of their position in the chamber; no restricted region (fiducial volume) was chosen due to the

expected lowness of the cross-section for strange particle production.

2.3 Criteria used to Select and Classify Events

The decision to select only those events having a visible decay was the main criterion in selecting the events to be studied. The only class practically excluded by this was that containing only charged K mesons. This is because their lifetime is about one hundred times longer than the other strange particles under consideration and the majority leave the chamber before decay. Within the chosen class of events a further set of criteria was applied to provide a cleaner sample of strange particles and to split the events into possible hyperon events and K meson events.

(a) Criteria applied to Charged Decays

A possible charged decay fell into one of three categories:

(1) Possible Hyperon.

(2) K meson.

(3) Non-strange particle decay (e.g. $\pi \rightarrow \mu + \nu$) or a scatter with a low energy recoil.

The first test applied was to see if the primary track of the decay could be classified by its ionization, providing this track had a length greater than about 5 cm this was a very good means of classifying the decay, particularly in the case of $\pi \rightarrow \mu + \nu$.

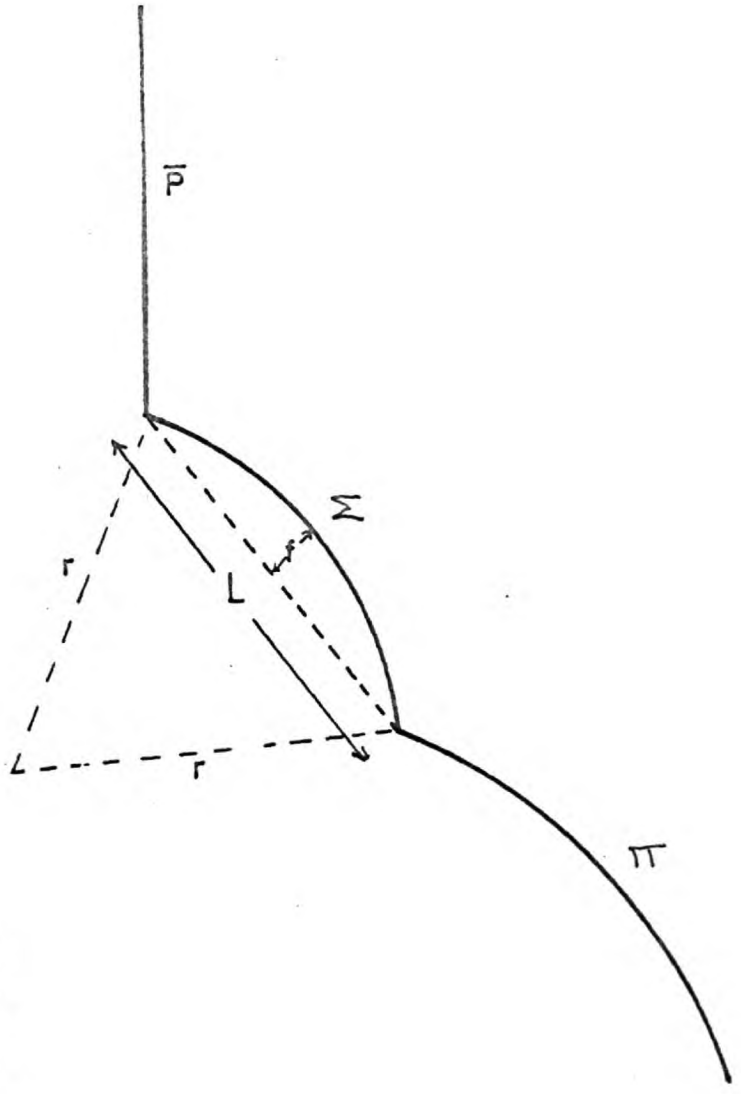

$$P = 300 H r \times 10^{-5} \quad (1)$$

$$(r-f)^2 + \frac{L^2}{4} = r^2 \quad (2)$$

$$\therefore \quad \frac{L^2}{4} \approx 2rf \quad (3)$$

$$\therefore \quad \frac{L}{P} = \frac{f}{L} \times \frac{2}{75H} \quad (4)$$

$$\therefore \text{ Probability of decay in } \frac{f}{L} = 1 - e^{-\frac{2fm \times 10^5}{75LHc\tau_0}}$$

$H = 20 \cdot 7$ kG
L, f = cms
P, m = gev

THE ABOVE HOLDS FOR PROJECTED QUANTITIES AS WELL

FIG 2·2

The separation between K meson decays and hyperon decays was ACCOMPLISHED on the basis of their difference in lifetimes.

The probability of decay of a particle in a time t, with a mean life in its own rest system of τ_o is

$$1 - e^{-t/\tau_o\sqrt{1-\beta^2}} \qquad (1)$$

where β is the velocity (in units of c) of the frame of reference in which the decay is observed relative to the particle.

The probability of decay in a distance L is found by substituting in (1)

$$t = L/v \quad \text{and} \quad P = mvc/\sqrt{1-\beta^2}$$

giving $$1 - e^{-Lm/Pc\tau_o} \qquad (2)$$

A typical decay is shown in Figure 2.2; using the notation shown there the following can be derived.

$$r^2 = (r - f)^2 + \frac{L^2}{4}$$

if f is rather small in comparison to L or r then

$$\frac{f}{L} = \frac{L}{8r} = \frac{L \times 300H}{8P} = \frac{\cdot00621\ L}{8P}$$

therefore

$$\frac{L}{P} = \frac{8f}{\cdot00621 \times L}$$

Substituting this in (2) gives

$$\text{Prob}^y = 1 - e^{-\frac{m}{c\tau_o}\frac{8f}{\cdot00621\ L}}$$

Putting in the mass and lifetime values for K mesons, Σ^+ and Σ^+ hyperons gives the respective probabilities as

$$1 - e^{-1\cdot75 \frac{f}{L}}, \quad 1 - e^{-345 \frac{f}{L}}, \quad 1 - e^{-670 \frac{f}{L}}$$

All charged decays with f/L smaller than $1/100$ were classed as hyperons, all others as K mesons. This meant that $\sim 3\%$ Σ^+ (or $\overline{\Sigma^+}$) and $< \frac{1}{4}\%$ Σ^+ ($\overline{\Sigma^+}$) were classed as K mesons and $\sim \cdot 02\%$ K mesons were classed as hyperons.

The above criteria were sufficient to separate charged decays quickly and unambiguously into the various classes.

(b) Criteria used for Neutral Decays

The decay of a neutral particle is observed in the chamber as two tracks of opposite curvature emanating from a common point (vertex, apex). To be associated with an event the line joining the VERTEX of the event to the vertex of the decay must lie between the two tracks of the decay. [redacted] providing the neutral particle decayed into only two particles. If a third (neutral) particle was present in the decay this condition could be violated. Such decays are relatively rare and also difficult to interpret, therefore, decays violating the condition were not noted.

Within this accepted class several possibilities existed for the interpretation of each decay.

(a) Possible hyperon.

(b) K meson.

(c) Electron pair (coming from $\gamma \rightarrow e^+ + e^-$).

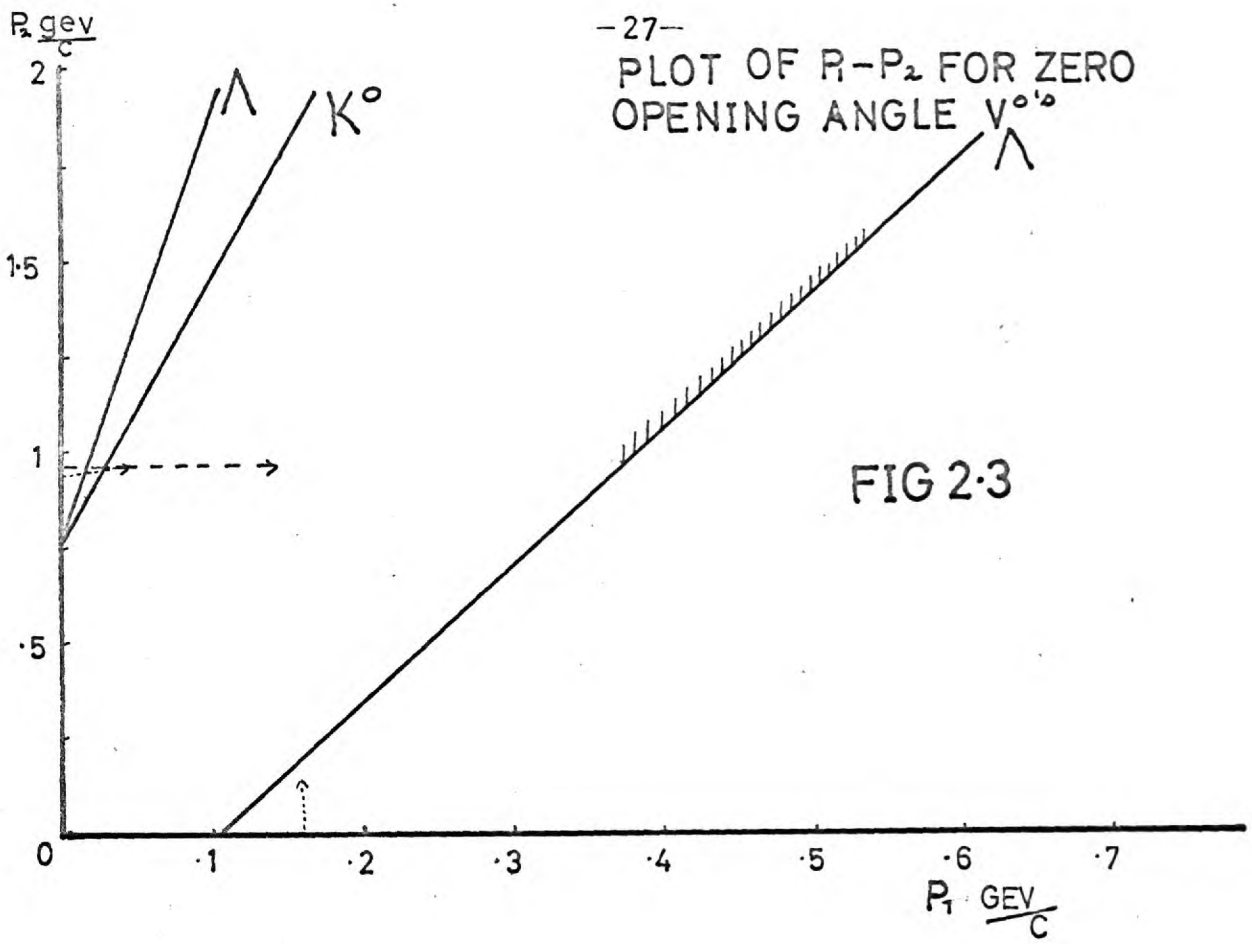

PLOT OF $P-P_2$ FOR ZERO OPENING ANGLE $V^{\circ}{}_{\Lambda}^{\circ}$

FIG 2·3

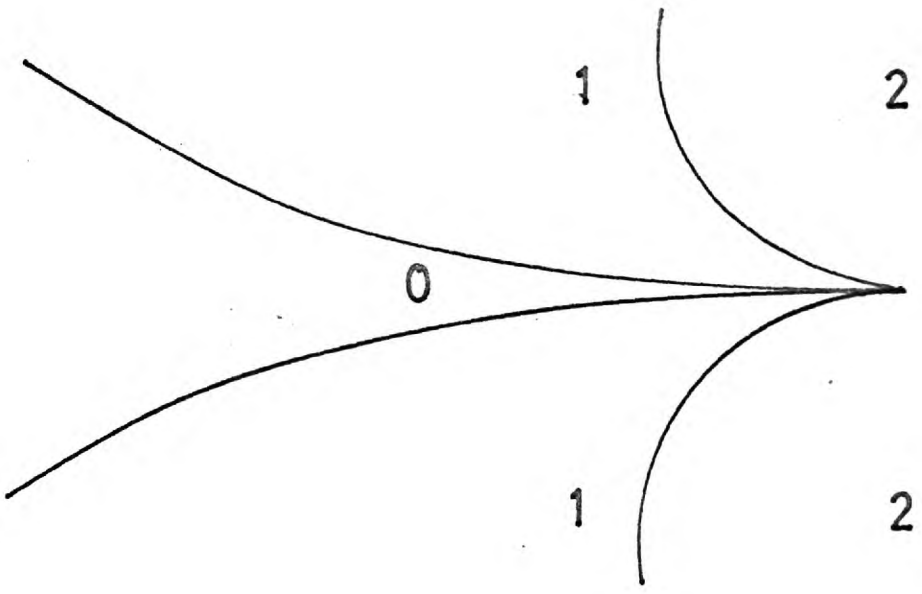

ELECTRON PAIR TEMPLATE

FIG 2·4

Each decay was classified using the known kinematics of such decays.

(c) Electron pairs

Electron pairs have an opening angle which is essentially zero and can only be confused with strange particle decays having this feature. These come from decays in which the line of flight of the two decay products in the rest system of the parent lies within a narrow cone forwards and backwards around the line of flight of the parent in the laboratory. Figure 2.3 shows a plot of P_1 versus P_2 for K mesons and lambdas, these being the momenta of the two decay products for a zero opening angle decay. Two lines are shown for lambda decays one for the proton being emitted along the line of flight the other for it against the line of flight. The dotted lines indicate the momenta at which it is possible to decide by ionization whether the two decay products are electrons or not. The template in Figure 2.4 was used for all ambiguous zero opening angle decays. This was placed on the scanning table over the images of the tracks of the decay in question, if the sum of the reference numbers of the two areas in which the tracks lay was ≤ 1 it was classed as a hyperon otherwise as an electron pair. Referring now to Figure 2.3 the shaded portion indicates the momentum range excluded by this template. The only decays rejected which were in fact strange particles were those of lambda's (or antilambda's) in the momentum range $P_\Lambda = 1{\cdot}4 \rightarrow 2$ Gev/c in which the proton (or antiproton) was in the forward direction, this being a small fraction of those produced.

(d) Non-zero opening angle decays

These were classified using ionization as the sole criterion. If one of the tracks was possibly a proton (or antiproton) then the decay was treated as a hyperon, if not it was a K meson.

2.4 General Procedure

The scanning was carried out using new machines commercially built, which projected an image of approximately chamber size onto a horizontal table. The machines were equipped with motorized film transport and facilities for superimposing two views to determine the depth in the chamber at which any particular bubble had been formed.

Scanning normally utilized two people at any one time, a physicist and a 'scanning girl'. The image of each frame in turn was examined by these two sitting at opposite ends of the scanning table. The physicist was responsible for final identification of any interaction found. In general although three views of each interaction were available for inspection one only was used; only in cases of ambiguity were the other two used.

During the first scan the criteria already described were used fairly loosely but always erring on the safe side. The author was then responsible for checking each interaction found and applying these rigourously. The film was then rescanned using as far as possible a different view than that for the first scan, the criteria being now used exactly in the form described.

2.5 Results obtained from Scanning

In referring to event types we use the following notation. An event is defined by a three digit number, the first digit denoting the number of charged particles emanating from the interaction, the second the number of charged decays and the third the number of neutral decays. The event numbers found are tabulated below.

1st Scan

Type	001	002	201	202	210	211	220	401	402	410	411	420	601	602	610	810
Numbers	76	24	155	18	52	26	11	125	12	54	8	1	9	2	10	1

2nd Scan

Type	001	002	201	202	210	211	220	401	402	410	411	420	601	602	610	810
Numbers	72	22	160	19	50	28	12	119	12	66	9	1	8	1	16	2

Combined

Type	001	002	201	202	210	211	220	401	402	410	411	420	601	602	610	810
Numbers	86	26	184	21	65	30	12	141	14	86	9	1	12	2	22	2

The efficiencies of observation were then calculated using the formulae

$$N\varepsilon_1 = N_1$$

$$N\varepsilon_2 = N_2$$

$$N\varepsilon_1\varepsilon_2 = N_{12}$$

Where N is the true number of events produced εn and Nn are the efficiency and number of events found in scan n and N_{nI} is the number of events common to scans n and I. This is not too rigourous in this type of experiment as it is implicit that within a given class of events all events are equally likely to be observed and an event missed in one scan is no less likely to be seen on the next. In fact this does not always hold particularly in the case of sigma decays when the decay occurs quickly or the decay angle is very small. These efficiencies are:-

Type	001	002	201	202	210	211	220	401	402	410	411	420	601	602	610	810
Per Cent Effcy.	96	98.5	97	99	93	99	99.9	98	98	78	99.9	100	75	100	52	100

[redacted] Estimation of Beam density

A third scan of three quarters of the film was undertaken to find the total number of beam tracks and to find the ratio of antiprotons to other particles present in the beam. Beam tracks were counted on every

tenth frame; if a possible beam track deviated by more than one seventieth of a radian from the mean beam direction it was not included. The average beam density was found to be 8·5 tracks per picture.

2.6 Estimation of Beam contamination

The maximum energy that can be transferred to an electron by an incident particle is a function of the mass of the particle and its velocity. For particles in the beam hitting the bound electrons in the hydrogen this is given by

$$Em \simeq \frac{2m_e p^2}{m^2}$$

For $\bar{p}$'s of 3·6 Gev/c Em = 15 Mev, therefore, all knock-on electrons (delta rays) with an energy greater than 15 Mev were produced by particles lighter than antiprotons contaminating the beam.

The number of delta rays with an energy greater than E, produced by a particle of charge z travelling through a medium of atomic number A and nuclear charge Z while traversing x gm/cm^2 is

$$N = \frac{\cdot 15\ Z\ z^2 x}{\beta^2\ A\ E(\text{mev})} \qquad (10)$$

In the case of hydrogen and incident singly charged particles

$$Z = z = A = 1$$

and $x = Lp$ where L is the length traversed and p is the density of liquid hydrogen

$$\therefore \quad N = \frac{\cdot 15\ L\ \cdot 057}{E\beta^2} \qquad (1)$$

The beam is known to be composed of antiprotons, pi mesons and mu mesons and at the incident momentum, β for all these particles is essentially one.

The technique adopted at the scanning table was to count (in a fiducial volume 54·5 cms long) all delta rays having a curvature corresponding to a momentum greater than 15 Mev produced by beam particles . All such delta rays were produced by particles other than antiprotons. The number of such delta rays found was 760 from 149,000 $\pm$ 1200 beam tracks scanned. A separate count was kept of delta rays ($\geq$ 15 Mev) occurring on tracks which further down the chamber also had an interaction. This was done because the interaction cross-sections for the two types of particles expected to be contaminating the beam is widely different. These two types of particles, pi and mu mesons, have cross-sections of approximately 30 mb and zero respectively.

Only two such delta rays were seen and this makes $<$ 1% Pi mesons in the beam. This is very important as pi mesons can produce interactions such as $\pi + p \rightarrow \Lambda + K$ which could simulate those being studied.

The length of track scanned has to be corrected for interactions occurring on contaminating tracks which shorten the length available for observing delta rays $\geq$ 15 Mev. As the cross-section for mu mesons is essentially zero, however, in this case no correction need be made. The total track length scanned was 149,000 x 54·5 cm. Substituting

for N in (1) gives $L = 1{\cdot}333 \times 10^5$ cm as the length of track formed by particles other than antiprotons. The percentage contamination is therefore:-

$$100 \times \frac{1{\cdot}333 \times 10^6}{78 \times 10^5} = 17\%$$

Putting in Poisson errors on the number of beam tracks, interactions and delta rays counted gives a final answer of

$$(17 \pm 1\%) \ .$$

2.7 General Features

As scanning proceeded it became evident that the most difficult events to observe were those involving sigma decays. It had been fairly evident also that the interactions were very peripheral. That is if a hyperon antihyperon pair were produced the antihyperon kept the character of the incident antiproton in having a high momentum. This had a bearing on the observation of sigmas. In general the antisigmas were very fast, the sigmas rather slow. In the former case due to the relativistic increase in lifetime they travelled further away from the production apex, but because of the high velocity of the sigma the angle between it and its visible decay product was often very small and so difficult to detect. When slow sigmas were produced the decay angle was larger, but the decay often took place within a few mms. of the production vertex again making detection difficult.

It was decided to look closely at all the interactions found having one or more decays to see if any of the other tracks could be reinterpreted as having been left by sigmas. In this way a few events were reclassified.

CHAPTER 3

MEASUREMENT AND COMPUTATION

3.1 Measuring technique

The measuring machine and technique used for measuring events has been described previously[11]. In essence the machine consisted of a stage capable of movement in a horizontal plane. This stage was motorized and its motion was digitized in two directions at right angles (x and y) using the principle of Moiré Fringes, counted by a high speed bi-directional counter designed by Messrs. Ferranti Ltd.

The three films corresponding to the views of an event were held by suction onto the stage and projected images of them were cast in turn onto a glass screen. X and Y coordinates of points along each track of the event and for each apex were then punched onto paper tape taking each view in turn. This was done by bringing the projected image of the point to be measured into coincidence with an engraved spot on the screen. A button was then pressed which actuated the electronic circuits concerned with transferring these coordinates to paper tape. A reference frame was set up for each view by measuring the positions of four fiducial marks, these being the images on the film of engraved crosses on the chamber windows whose positions relative to each other were accurately known. Approximately ten points per track per view were measured these in general being different points on each view.

Photographs of all events had been taken after scanning and these prints were available to the measurer for reference in cases of difficulties. Special features relating to an event were written by a physicist onto a form which was filed with the relevant print. These were noted by the measurer who added to them any comments necessary regarding difficulty of measurement.

The machine described above was superceded during the experiment by two new commercially built machines whose schematic outline is, however, exactly the same.

Techniques applicable to measurement

Due to equipment failure and mistakes by the operators each event had to be measured twice on the average before a tape was obtained with no mistakes on it. Typical mistakes were due to misidentification of tracks, inaccurate setting by the operator, and mispunching by the machine.

Difficulties peculiar to this experiment in general came from the tracks and apices of charged decays. Sigmas normally decayed within one or two centimetres of their point of production, thus leaving a track length whose curvature could not be measured. The decay apex was very often indistinct as well, because of small decay angles. The technique adopted was to consider the sigma track as being straight measuring only three points on it and in cases of difficult apices a physicist told the measurer the exact point to measure.

In order to minimize the number of events needing remeasurement and to obtain good measurements of the curvatures of tracks measured, only those events occurring at least four centimetres away from the chamber walls were measured. A further restriction was also used that the decay tracks of a decaying particle had to be longer than 4 mm on the film. A decay not satisfying this was not measured and the event with which it was associated was reclassified.

3.2 Programming System

The system used to calculate from the measurements of an event a complete spatial and kinematical interpretation of it is described below. This system came into operation in our group during the course of this experiment. The system was, however, formulated by groups at CERN who wrote all the programmes used, except for slight modifications carried out to enable them to work with the facilities available at Imperial College.

A flow diagram of the system is shown in Figure 3.1. The full lines indicate the links between the various parts. The dotted lines show what happened to events which failed and at which stage they were re-fed in.

All the collaborating groups differed in their means of processing the events except that the last stage was always the same (GRIND).

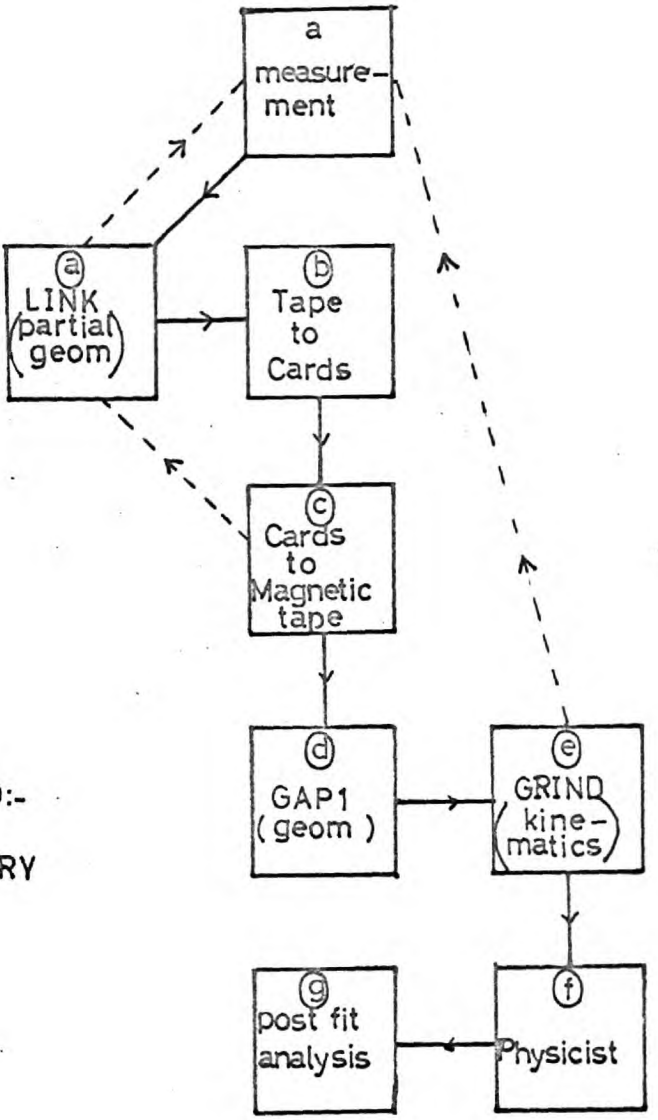

COMPUTERS USED:-

ⓐ FERRANTI MERCURY

ⓑ IBM 045

ⓒ IBM 1401

ⓓ IBM 7090

ⓔ IBM 7090

ⓕ —

ⓖ ELLIOT 803

FLOW DIAGRAM OF COMPUTING SYSTEM

FIG 3·1

(a) Link Programme

This consisted of a truncated version of the geometry programme described in CERN 60-33[12] (Moorhead Geom). Its main function was to check all the measurements for accuracy and to complete the first approximate helix fit for each track. It was necessary to supply as data for this programme the known positions of the cameras and fiducial marks, thicknesses and refractive indices of all media interposed between the liquid hydrogen and the cameras. These were then used to set up a reference frame to which any point in the chamber could be referred. Using the measured fiducial mark positions for each view of an event, the transformation coefficients necessary to change film coordinates to space coordinates were found.

The measurements of each track on each view were then checked by fitting an arc of a circle through them, if more than one point was over 200 microns off this arc the event as a whole was rejected. After this, apex positions were reconstructed and the first approximate helix fit was obtained for each track.

A paper tape was then punched out consisting of the above partial geometry results plus all the original measured coordinates.

Throughout the whole of the above, checks were made to ensure that all quantities and errors were within preset tolerances (read in as data for the programme).

Failure at this stage in general meant remeasurement.

(b) and (c) Translation

The information from the LINK programme had to be converted into a suitable form so that it could be used as data for GAP, an IBM 7090 programme. This was done in two stages, firstly by transmitting it from paper tape to cards and then from cards to magnetic tape. The cards were permanently stored, but both the paper tape and magnetic tapes were discarded after events had successfully been passed through the system.

(d) Geometry

This programme known as GAP 1[13] consisted of a Fortran version of the Moorhead Geometry from that point already reached by the LINK programme.

The magnetic tape containing the LINK results was used as data for this programme together with a set of constants similar to those used at the LINK stage (camera positions etc.).

The final least squares helix fits were then calculated for all tracks together with the final positions of all apices (using convergence of tracks as well as measured positions). No account was taken in this fitting of possible deviation from a helix which can occur due to, Coulomb scattering, variation of magnetic field and energy losses. Any track which deviated grossly from a helix therefore could not be reconstructed correctly. This only occurs for tracks having a large curvature, however, and by measuring only the first portion of such curves accurate reconstruction could be obtained.

This geometry programme had been thoroughly tested over a number of years, and for this reason all output from it was stored and kept after it had been used as data for GRIND. This was in case, due to any initial difficulties with GRIND, events had to be run again. On several occasions in fact this proved to be necessary.

(e) Kinematic Fitting

This was done by a programme consisting of a series of logical routines known collectively as GRIND[14].

It firstly required as data information relating to the experiment as a whole. This consisted of:-

(a) Magnetic field table and an interpolation equation to enable the field at any point in the chamber to be calculated.

(b) A range momentum table suitable for all particles.

(c) A series of hypotheses (Appendix 4) for each event topology which the experimenter wished to be tried on the events.

(d) The shape and size of the chamber and minimum track lengths which were measured.

(e) A series of constants relating to the mathematical processes of fitting, e.g maximum allowable value of chi squared, maximum permissible number of steps in various iterations.

Once this data had been read in by the computer the geometry results which were stored on magnetic tape were read in event by event.

At this point the geometry results for each event consisted of

numerical values for the positions of apices, and positions, directions and curvatures of tracks as well as the uncertainties in these quantities due to measurement errors.

GRIND then used these values as a starting point to find, if possible, a unique interpretation of the event in terms of the known elementary particles and their conservation laws. If such an interpretation was possible the geometrical values were corrected according to the method of least squares in order to make them obey the constraints of momentum and energy conservation.

There is one general principle which applies to all fitting processes of the type above and provides a fundamental limitation on finding a unique interpretation. This limitation is energy and momentum conservation. At each interaction or decay point there are four equations available to find unknown parameters corresponding to the separate conservation of each of the three components of total momentum and the conservation of energy. With each particle in the event four quantities can define it, e.g. m, Px,Py,Pz. For all visible tracks, therefore, which are measured m is the only unknown, but this is assumed for each hypothesis tried. If all tracks are seen, then we have four equations and no unknowns; this being known as a four constraint fit. If there is one missing neutral then we have only a one constraint fit; it is impossible to fit more than one missing neutral.

In each hypothesis used masses are assigned to the seen particles,

and the fitting process is carried out at each apex in the event. The geometrical momentum, however, for each particle is given at the centre of the track. It is, therefore necessary each time a new mass is assigned to a particle to take account of the energy loss between apex and centre of the track. This process is known as 'swimming' and utilizes the range-momentum table.

At any apex which is to be fitted the hypothesis in hand gives rise to a unique interpretation for each seen particle. It is important at this point to define variables specifying each track which as far as possible are normally distributed. These are $\frac{1}{P}$, λ, ψ (P - momentum, λ = dip angle, ψ = azimuthal angle).

The decays of the strange particles in each event were fitted first, each V^o was tried to see if it was compatible with any or all of the hypotheses $\Lambda \longrightarrow p + \pi$ $\bar{\Lambda} \longrightarrow \bar{p} + \pi$

$K \longrightarrow \pi + \pi$ $\gamma \longrightarrow e^+ + e^-$.

Values at the apex of $\frac{1}{P}$, $\tan \lambda$, ψ were found for each track and then the missing momentum energy and mass were calculated. Provided this momentum vector passed within a small preset distance of the overall event apex then the neutral decay was considered to be associated with the event. This meant the line of flight of the neutral was specified and only its momentum was not known, the fit being, therefore, a three constraint fit. For each of the possibilities above the geometrical values were moved until either the fit was successful or failed because

it had reached a physical or mathematical impossibility. Each charged decay was then fitted in a similar way except that here in general measurements of the momentum and angles of the decaying particle were present making it a one constraint fit. If the track left by the decaying particle was short, only its angles were measured meaning zero constraints. In such a case no fit can be done as such, but interpretation can be achieved for every mass hypothesis tried, except in cases of imaginary solutions.

The overall event was then fitted using only those hypotheses which contained the successful fits at the decay vertices. For each event two possibilities existed these being, that all final state particles had been seen or that one or more neutrals had been present. For each event $\sum E$ and $\sum \vec{P}$ were moved in such a way so as to see if a fit to one or both of these hypotheses was possible.

All successful 'fits' at each stage were printed out together with the reasons for failure of the other hypotheses. The most common reason for failure was that in order to obtain a fit, quantities had to be moved on improbable amount judging from the known average uncertainty of the measurements and the rules of statistical fluctuation. A measure of this was the value of a function known as chi squared[14] which is a function composed of terms such as

$$\frac{(\text{Observed quantity} - \text{Expected quantity})}{(\text{Error matrix})^2}$$ and is

a measure of by how much quantities have been corrected. This is a well known mathematical function and its distribution for a large number of events is also known. The value of any chi square can be turned into a probability and in practice all fits which were less than one per cent probable were rejected. This chi squared function was used in the actual fit in the sense that from the many possible combinations of corrections which could produce a given fit that set which minimized chi squared was chosen. This corresponds to the highest probability obtainable. Other failures generally occurred because of non-convergence in the iterative processes used to obtain a fit, which indicated the impossibility of satisfying energy and momentum conservation, while at the same time approaching a minimum value of chi squared.

3.3 Errors present in Events

It is very important when using a fitting programme to be able to estimate accurately all sources of errors present in the measurements of events. Otherwise the main criterion for rejecting fits, that measurements have to be moved on improbable amount, is meaningless.

The errors inherent in the design of the bubble chamber used were the largest single source of inaccuracy in this experiment. The other main source, that of the measuring system was approximately on order of magnitude smaller.

The errors introduced by the chamber are two-fold, the first being

due to Coulomb Scattering as the particles pass through the hydrogen, the second is due to the liquid motion after expansion carrying away the bubbles from their initial position.

The measuring technique also introduced two errors, a random one due to setting on the tracks and apices and a systematic one in that the movement of the stage introduced an extra curvature into each track.

All these errors had been measured prior to this experiment during previous bubble chamber runs. In particular the chamber distortions had been estimated by several laboratories and the results combined,[15] while those due to the measuring machine were estimated within our group[16]. The distortions due to the chamber do tend to vary from time to time depending on the exact conditions. The results from previous runs indicated however that this variation was not too large and it has been ignored.

The measurement of these errors consisted of several stages. Firstly an image on film of a stretched fibre of glass was obtained and placed along the x axis of the measuring machine and measured 100 times: it was then reversed and the process repeated. Using the method of least squares parabolas were fitted to all these measurements and for each of the two sets a root mean square sagitta was found. Any curvature introduced could come from the image itself or the machine but by reversing the image these two could be found, i.e. in terms of sagittas

1st set S_{RMS} = S machine + S fibre

2nd set S'_{RMS} = S' machine - S fibre

$\therefore$ S_{RMS} and S'_{RMS} = 2 S machine.

In this way it was found that for a track of 60 cm

$$S_{\text{machine}} = 5 \text{ microns}$$

This was also done for the y axis. During past experiments film was obtained at frequent intervals with no magnetic field present in the chamber. Any curvature present in tracks on this film was due purely to distortions. Measurements of these tracks were made and parabolas fitted. It was found that the root mean square sagitta was different from zero by 75 microns and that the spread due to Coulomb scattering about this point was also 75 microns.

These errors were used in the fitting programme together with the reconstruction errors. The correlation between errors in curvature and angles being calculated (partly empirically) by the programming group at CERN[17].

The accuracy with which a track curvature can be measured depends on the size of its sagitta. For a given length of track the sagitta (s) varies as the reciprocal of the momentum of the particle which left that track. The higher the momentum therefore, the greater effect the distortions have on the accuracy of measurement.

Another limit on accuracy is for short tracks where distortions are not so important, but measurement errors are decisive.

CHAPTER 4

TECHNIQUES OF ANALYSIS

4.1 Interpretation of Events

The processing of the measurements to provide possible kinematical interpretation of events has been described in the previous chapter. After this it was necessary to try and assign a unique interpretation to each event using physical facts not included in the fitting programme.

The main information used at this stage was the relative ionization of each track of the event. This was used in two ways, firstly to see if for events having only one interpretation (fit) the fitted momenta were compatible with the ionization values, secondly for an event with several fits, if the observed ionization was incompatible with any of these fits. In general only one hypothesis was successful in the fitting and this agreed with visual ionisation estimates. Of the remainder visual estimation of ionization was sufficient to classify a large number and quantitative microscope measuremonts of ionization resolved all but a few ambiguities. Overall only about one per cent of events were not fitted uniquely when account was taken of ionization.

In order to achieve such a high percentage of unambiguous events some post GRIND analysis was done on events with good geometry results but which for one reason or another were not capable of interpretation by GRIND. This analysis was done using programmes written by the author

DIFFICULTIES

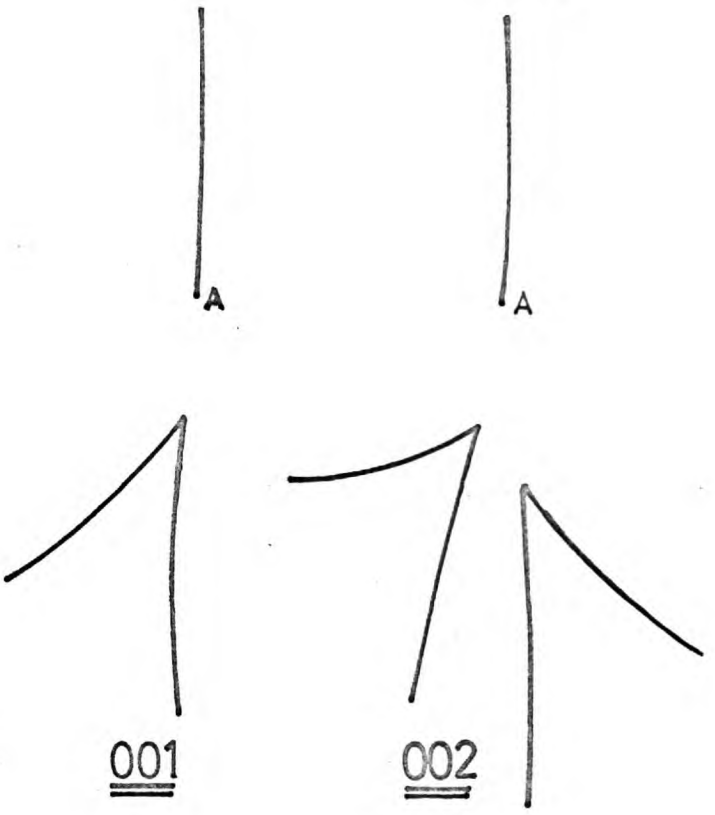

uncertainty in position of apex A

FIG 4-1

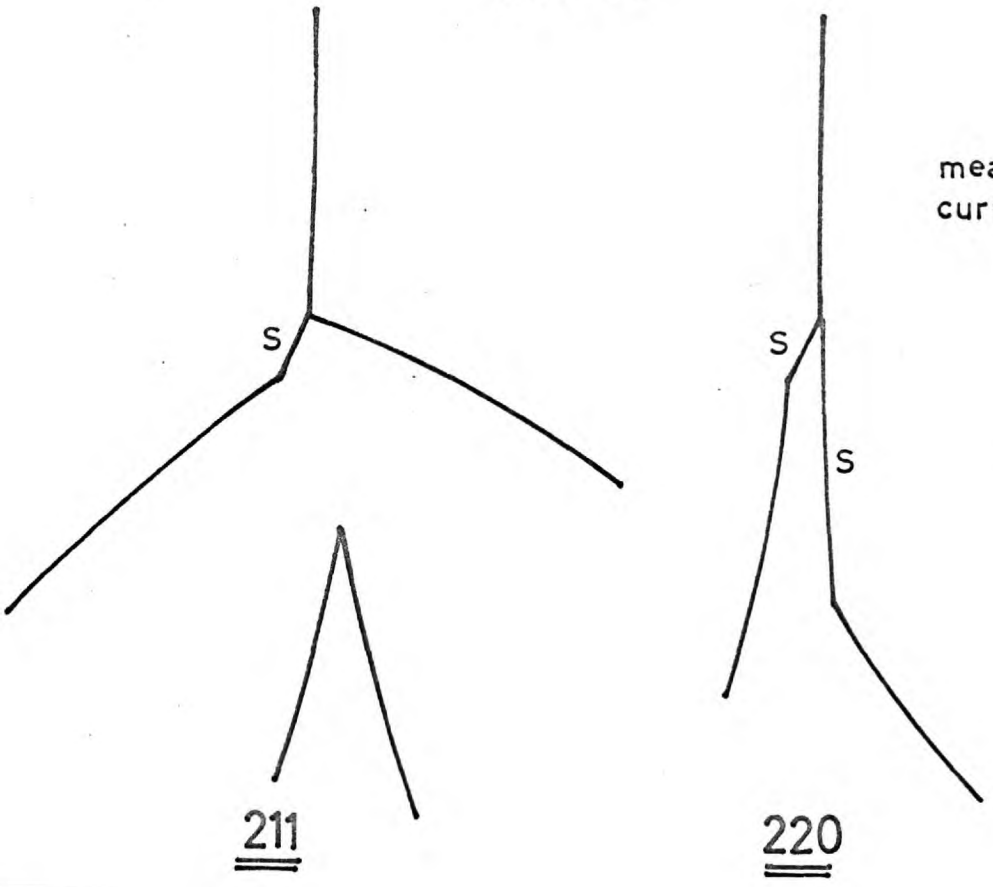

measurement of curvature of S

and his associates. The type of analysis done and the reasons why varied from one event topology to another. These topologies with these features indicated are shown in Figure 4.1.

001's and 002's

As no visible secondary tracks occur in these event types the interaction apex is not well defined. Normally the last visible bubble was taken as being this point but in a few cases particularly when the mean gap length was high this point was significantly different from the true apex. In such cases the V^0's measured with the event were considered to be unassociated (by GRIND) with the event apex measured. All cases of unassociated neutral decays were therefore checked to see if they could be associated with a point near the apex measured. Using the axes defined in Figure 4.1 it can be easily seen that the only error in the apex can occur in the +x direction; therefore, if the line of flight of the neutral found from the single vertex fit was compatible with passing through a point having a higher x coordinate but the same y and z coordinates as the measured apex it was considered to be associated and included in the overall analysis. Provided always that the deviation of the apex position was consistent with the observed mean gap length of the incident track.

211's

The short lived sigmas were the cause of difficulties with this class of event due to the poor estimation of their momentum. In one mean

life a particle travels a distance $L = \frac{Pc\tau_0}{m}$ and at this point the probability that it has decayed is 67%. Typically sigmas had momentum of about •5 Gev/c and antisigmas > 3 Gev/c corresponding to lengths as defined above of

2 cm and 12 cm - Σ^+ $\overline{\Sigma}^+$

1 cm and 6 cm - Σ^+ $\overline{\Sigma}^+$

The sagittas of such tracks being

41μ and 360 μ - Σ^+ $\overline{\Sigma}^+$

8 μ and 90 μ - Σ^+ $\overline{\Sigma}^+$

Thus it can be seen accurate curvature measurements were not possible in a large number of cases (cf P 48). The kinematics of the decay can be used, however, to find this momentum. If the momentum and angle of the decay product (relative to its parent) are known then for each parent mass assumed two momentum values for the parent can be found. Very often therefore eight momentum values were found for a charged decay corresponding to

$$\Sigma^c \rightarrow N^c + \pi^o, \quad \Sigma^c \rightarrow \pi^c + N^o$$
$$K^c \rightarrow \pi^c + \pi^o, \quad K^c \rightarrow \mu^c + \nu^o .$$

Fitting the event as a whole and ionization estimates were usually sufficient to uniquely determine the event. Approximately 10% of this class of events were fitted by 'hand' from the geometry results. These were usually those with short dipping primary sigma tracks.

A saving feature of this type of event was that in nearly all cases no neutral pi mesons were produced, the events being predominantly $Y\bar{Y}\pi$ with all particles 'seen'. It was therefore sufficient in the difficult cases to leave out the charged decay altogether and to re-compute it using the other known values of mass, angles and momentum of the remaining particles. The known decay product was then used to check that it was consistent with the decay of the sigma whose angles and momentum had been computed. This resulted in all events of the type $Y\bar{Y}\pi$ being successfully analysed.

220's

This was by far the most difficult class of event to analyse due to the large uncertainties in the momenta of the final state products. It was realized that in all probability the decays in these events corresponded to sigma decays. The lifetime of a K^c meson is over a hundred times larger than that for sigmas and the chance of two decaying in such short distances as were observed is very small. It was decided, therefore, to see if the events were compatible with being

$$\bar{p} + p \longrightarrow \Sigma + \bar{\Sigma}$$

with no extra neutrals.

The author wrote a programme to calculate for this reaction the momentum and angular distributions possible theoretically. The quantities used (see Figure 4.2) were P_1, P_2, θ_1, θ_2, and θ^*, the first four being

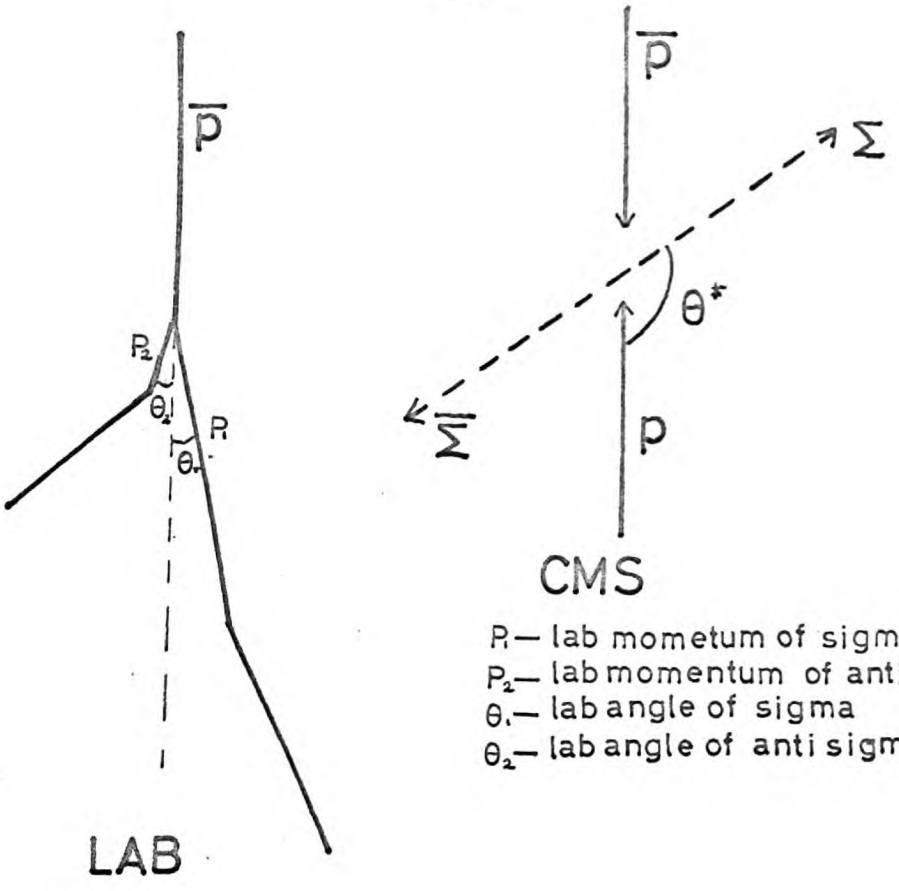
$\bar{p}$
P_2
θ_2
P_1
θ_1
LAB
$\bar{p}$
Σ
θ^*
$\bar{\Sigma}$
p
CMS
P_1 — lab mometum of sigma
P_2 — lab momentum of anti sigma
θ_1 — lab angle of sigma
θ_2 — lab angle of anti sigma

FIG 4.2

calculated at intervals of one degree in θ^* from $0^\circ \longrightarrow 180^\circ$. A further programme was then written to take the geometrical values of azimuth and dip for each event and calculate the measured θ_1 and θ_2. In general one of these was much more accurate than the other having been calculated from a longer track. This more reliable one (θ_1) was used together with the theoretical table to give P_1. For any value of θ_1 there exists two possible values of P_1 so the measured θ_2 was used as a guide to rejecting one of these.

Then using the measured λ and ϕ and calculated P_1, plus the incident antiproton parameters, the λ and ϕ of the missing particle were found (having momentum P_2). These two sigmas were then used with their respective decay products to determine if in fact they were compatible.

In all cases not fitted by GRIND a very good fit was found using the above technique. It is possible that the reaction

$$\bar{p} + p \longrightarrow \Sigma + \overline{\Sigma} + \pi^\circ$$

could be misinterpreted using the above but it is thought that for the events discussed such ambiguity is not present as such good agreement was found with two body final states.

Other Classes

The 210 class was not analysed as it suffered from the disadvantages of poorly measured charged decays with no possibility of computing it as there was always one missing neutral.

The 201 class had no difficulties except that it contained a large background of K meson decays. Similarly with all four prong events except that here there were essentially no hyperons, so the analysis of this class was stopped at an early stage.

4.2 Effect of Peripheral Interactions

It was realized at the scanning stage that the interactions were strongly peripheral and that because of this it would be difficult to determine accurately the momenta of the anti-particles and their subsequent decay products.

Typically a lambda was produced with a momentum of •6 Gev/c while an antilambda normally carried momentum of about 3 Gev/c. If such a pair were produced at the midpoint of the chamber each in one mean life would travel 4•5 cm and 22•5 cm respectively, thus leaving 30 cm and 12 cm of chamber for decay products. The nucleons in the decay products carry nearly all the momentum and this means that typically the tracks left by the nucleons had sagittas of 7500 microns and 500 microns respectively. The size of this sagitta is an indication of the accuracy to which a curvature can be measured and, therefore, it can be seen how the accuracy of measurement of antiparticles was much lower than that for particles.

To some extent this was smoothed out in the single vertex fitting process in which a direction and mass for the decaying particle is known.

DISTRIBUTION OF MASS SQUARED BEFORE FITTING OF $V^{o's}$

FIG 4·3

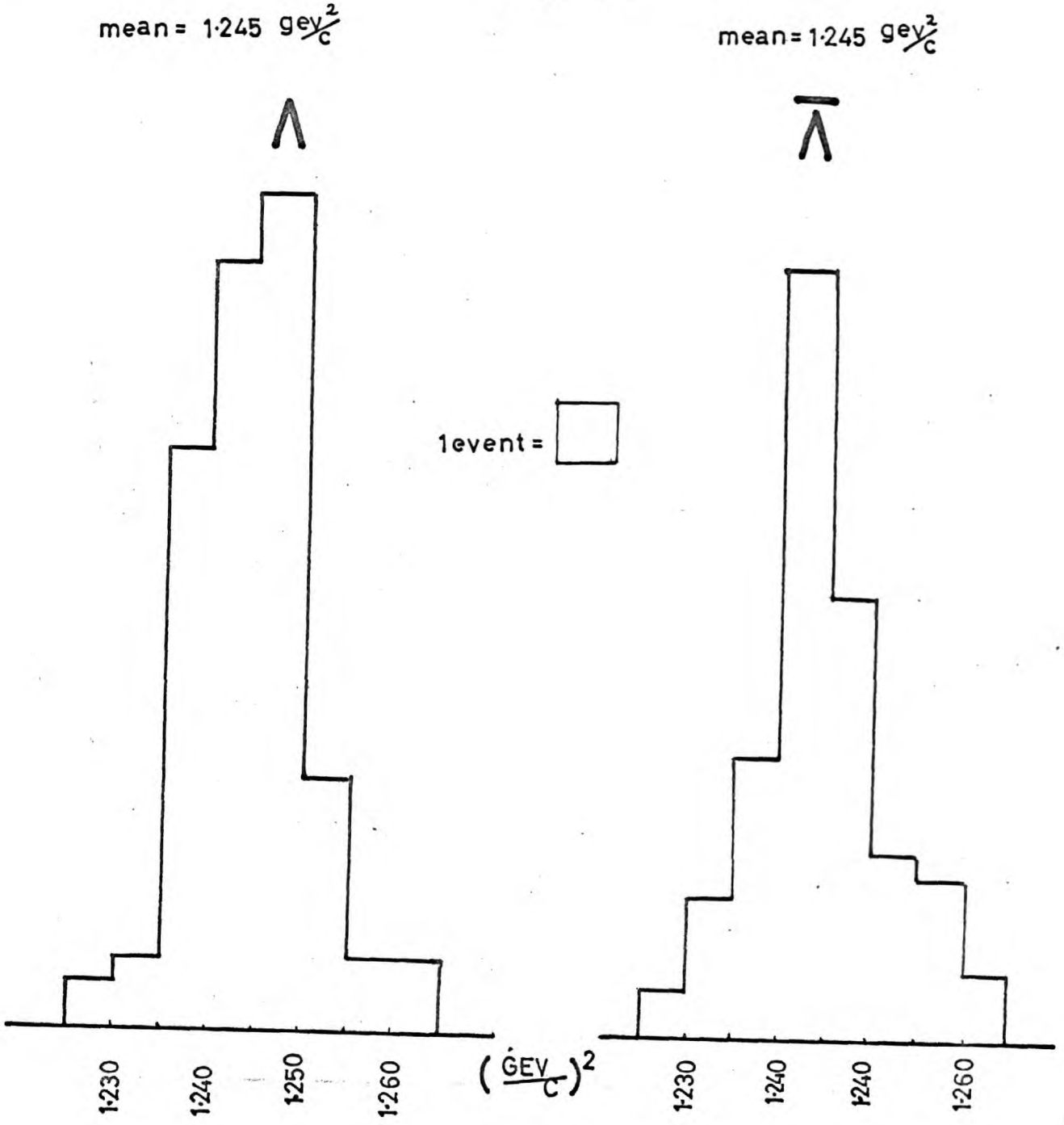

If an overall fit for the event was obtained then a very true picture of the interaction emerged. For the two outgoing particles of each decay the quantity

$$m^2 = (\sum E)^2 - (\sum \vec{P})^2$$

was calculated using measured values. The distributions obtained from this are shown in Figure 4.3 for lambdas and antilambdas separately.

The mass of these particles is well known and the central value found is exactly this value. This to some extent tests the reconstruction programme. The width of these two distributions is very similar which at first sight considering the relative inaccuracy of antilambda measurements is surprising. For a antilambda decay we have, however,

$$(\sum E)^2 - (\sum \vec{P})^2 = (\sqrt{P\bar{p}^2 + m\bar{p}^2} + \sqrt{P\pi^2 + m\pi^2})^2 - (\vec{P\bar{p}} + \vec{P\pi})^2$$

$$\therefore M^2_{\bar{\Lambda}} = m\bar{p}^2 + m\pi^2 + 2\sqrt{P\bar{p}^2 + m\bar{p}^2}\sqrt{P\pi^2 + m\pi^2} - 2P\bar{p}\,P\pi\,\text{Cos}\,\theta$$

To a first approximation the only error occurs in the measurement of $P\bar{p}$.

$$\therefore \frac{d(M^2_{\bar{\Lambda}})}{d\,P\bar{p}} = \frac{2P\bar{p}\sqrt{P\pi^2 + m\pi^2}}{\sqrt{P\bar{p}^2 + m\bar{p}^2}} - 2\,P\pi\,\text{Cos}\,\theta$$

Putting in typical values of

$$P\bar{p} = 2{\cdot}5\ \text{Gev/c} \qquad P\pi = 400\ \text{Mev/c} \qquad \text{Cos}\,\theta = 5^\circ$$

one obtains $\dfrac{d(M^2_{\bar{\Lambda}})}{d\,P\bar{p}} = -\ {\cdot}01$ which is a very small dependence.

This means, however, that it is very easy to obtain a fit for

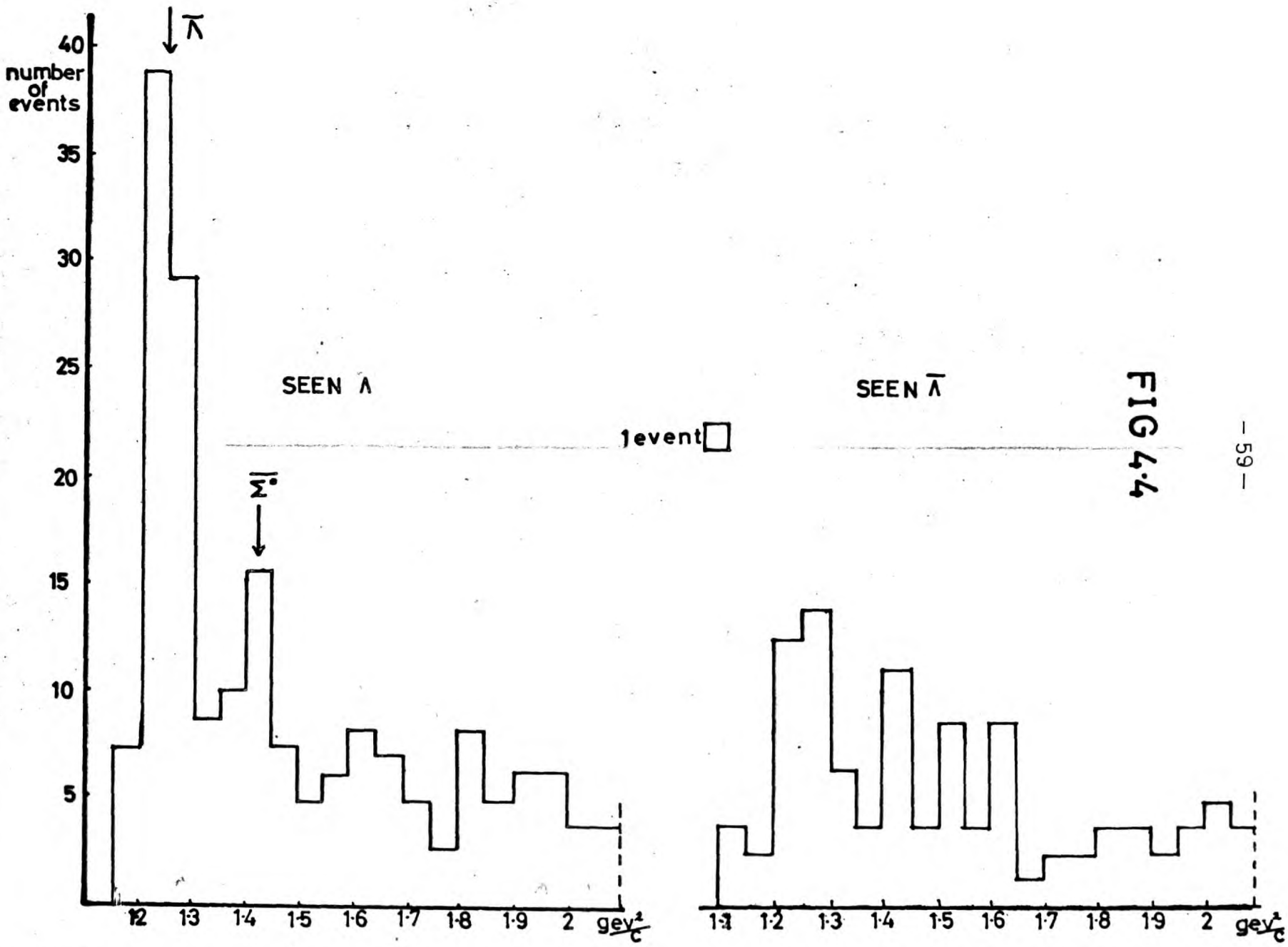
40
number of events
35
30
25
20
15
10
5
$\bar{\Lambda}$
$\bar{\Sigma}^0$
SEEN Λ
1 event
SEEN $\bar{\Lambda}$
1·2
1·3
1·4
1·5
1·6
1·7
1·8
1·9
2
gev/c

FIG 4.4

an antilambda which is wrong by approximately the error in $P\bar{p}$. At such high momenta, the antiproton carries nearly all the momentum, and an error in the antiproton momentum does not really change the antilambda line of flight significantly. So although a direction of flight is known for the antilambda, in this case it is very little use in obtaining the correct fit.

If we now look at the plots in Figure 4·4 which are the missing mass squared at the production apex for 001's in the cases for a seen lambda and seen antilambda, the effect of the errors clearly shows up. In the case of a seen lambda the distribution shows clearly two peaks corresponding to a missing antilambda and antisigma zero; this is not so for the antilambda distribution which is smeared out. Following a similar line as before,

$$(M\,M)^2 = (E_I - \sqrt{P_{\bar{\Lambda}}^2 + M_{\bar{\Lambda}}^2})^2 - (\vec{P_I} - \vec{P_{\bar{\Lambda}}})^2$$

$$= E_I^2 - 2E_I\sqrt{P_{\bar{\Lambda}}^2 + M_{\bar{\Lambda}}^2} + P_{\bar{\Lambda}}^2 - P_I^2 + 2\,P_I\,P_{\bar{\Lambda}}\,\mathrm{Cos}\,\theta$$

$$\therefore \frac{d(MM)^2}{d\,P_{\bar{\Lambda}}} = -\frac{2\,E_I\,P_{\bar{\Lambda}}}{\sqrt{P_{\bar{\Lambda}}^2 + M_{\bar{\Lambda}}^2}} + 2\,P_I\,\mathrm{Cos}\,\theta$$

Typical values are $P_{\bar{\Lambda}} = 2{\cdot}6$ Gev/c $\quad \mathrm{Cos}\,\theta = 5^\circ$

$$\therefore \frac{d(MM)^2}{d\,P_{\bar{\Lambda}}} = {\cdot}3$$ i.e. thirty times more than for the previous case.

This was also seen in the fitting process where in general if the reaction $\bar{p} + p \rightarrow \bar{\Lambda} + \Lambda$ could be fitted so could $\bar{p} + p \rightarrow \bar{\Lambda} + \Sigma^0$.

DISTRIBUTION OF PRIMARY MOMENTUM FOR FITTED EVENTS

FIG 4·5

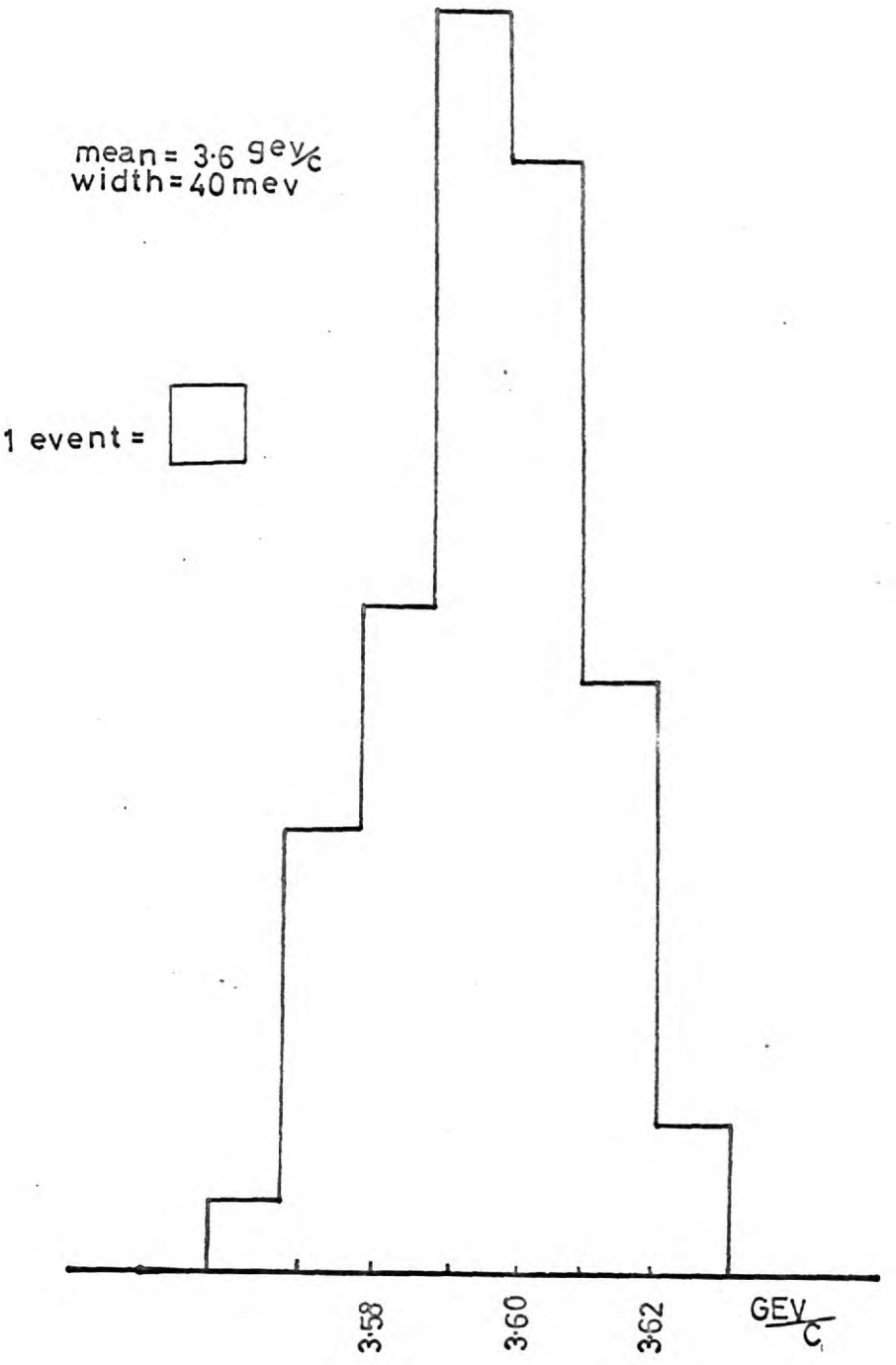

In the main only those 001's with a visible lambda were used for analysis.

4.3 Beam momentum and Spatial Distribution

The beam momentum as determined by the beam designers was (3·6 ± ·022) Gev/c. This value was much more accurate than could be determined in a single interaction by measurement. This value was, therefore, set in the programme and used as a starting value in the overall fit. To check that this value was correct a plot of the final value of the beam momentum after fitting in each interaction was made. This is shown in Figure 4·5 and agrees very well with the above.

The spatial distribution at entry to the chamber was also checked to see if the beam was well centred. This was done by taking the reconstructed apices of events and correcting their position due to the curvature introduced on the tracks by the magnetic field. A scatter diagram is shown in Figure 4·6 of z - y with arrows showing the fiducial volume used.

Fiducial Marks

The positions of all fiducial marks, camera positions etc. were measured and calculated at CERN. The fiducial mark positions were checked, however, by taking several sets and measuring the remainder as points. These were then reconstructed and checked against the given positions. These measurements all agreed with the given positions within the reconstructed errors.

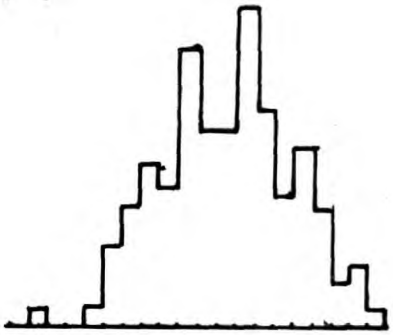

projection on z axis

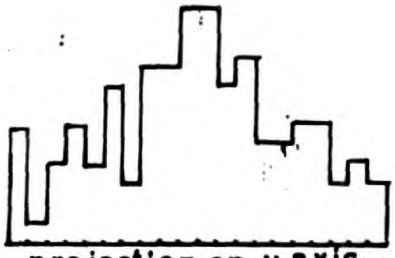

projection on y axis

FIG 4·6

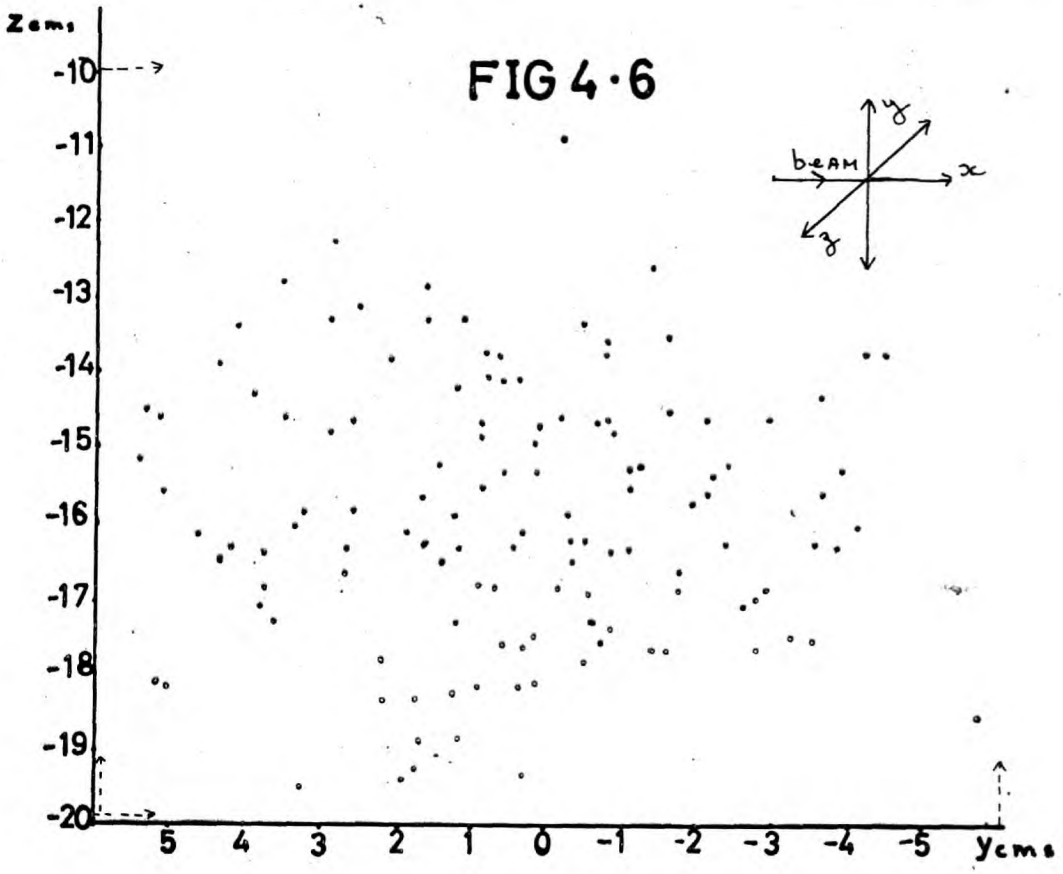

DISTRIBUTION OF BEAM AT ENTRY TO CHAMBER

CHAPTER 5

ESTIMATION OF EVENT LOSSES AND CALCULATION OF CROSS-SECTIONS AND BRANCHING RATIOS

5.1 Event Types

The events discussed in the following sections are those in which a hyperon and an antihyperon were produced. In general these events included an extra pi meson about 50% of the time and rarely two pi mesons. The techniques described are general ones used to detect and estimate losses but specifically orientated to this experiment.

5.2 Lifetime Losses

Due to the finite size of the chamber some decays take place outside the illuminated region. In practice curvature measurements can only be made on tracks having a sagitta larger than the errors present in the measurement. In order to facilitate this only those decays having secondary tracks greater than four millimetres on the film were measured. This of course further restricted the volume in which decays were considered to be 'visible'. As well as this a decay which occurs very close to the production apex is difficult to detect whilst scanning. In this respect a neutral particle decay is easier to observe than a charged decay. The latter needs a primary length sufficient so that a change of direction on decay is obvious whilst the former is indicated by lack of a track between apices. Only those neutral particle decays whose inter apex distance was greater than 3 mm (1σ, in space) and charged decays

having $l_o > 5$ mm were measured.

It was, therefore, necessary to estimate from the observed distribution of decays the total number of particles of each type produced.

The probability of a particle of momentum P, mass m and mean life τ_o decaying in a distance L is

$$1 - e^{-Lm/Pc\tau_o},$$

therefore the probability of decay between $L = l_o$ mm and $L = L$ is

$$\left(e^{-l_o m/Pc\tau_o} - e^{-Lm/Pc\tau_o}\right).$$

If N decays are observed in the chamber then it is easily seen

$$\sum_{1}^{N} \frac{1}{e^{-l_o m/Pc\tau_o} - e^{-Lm/Pc\tau_o}}$$ particles

must have been produced. This process is known as weighting, and the quantity $\frac{1}{e^{-l_o m/Pc\tau_o} - e^{-Lm/Pc\tau_o}}$ for a decay is known as its weight (>1). In order to correct for those decays seen but not measured, L (potential length) was calculated for each decay from the production apex to that point along the flight path of the particle where if it had decayed with the observed characteristics one of the decay tracks would have been less than 4 mm on the film.

5.3 Branching ratio losses

These are two-fold, one being neutral decay modes of neutral

FIG 5·0

PLOT OF DECAY ANGLE OF SIGMA VERSUS MOMENTUM(Σ)

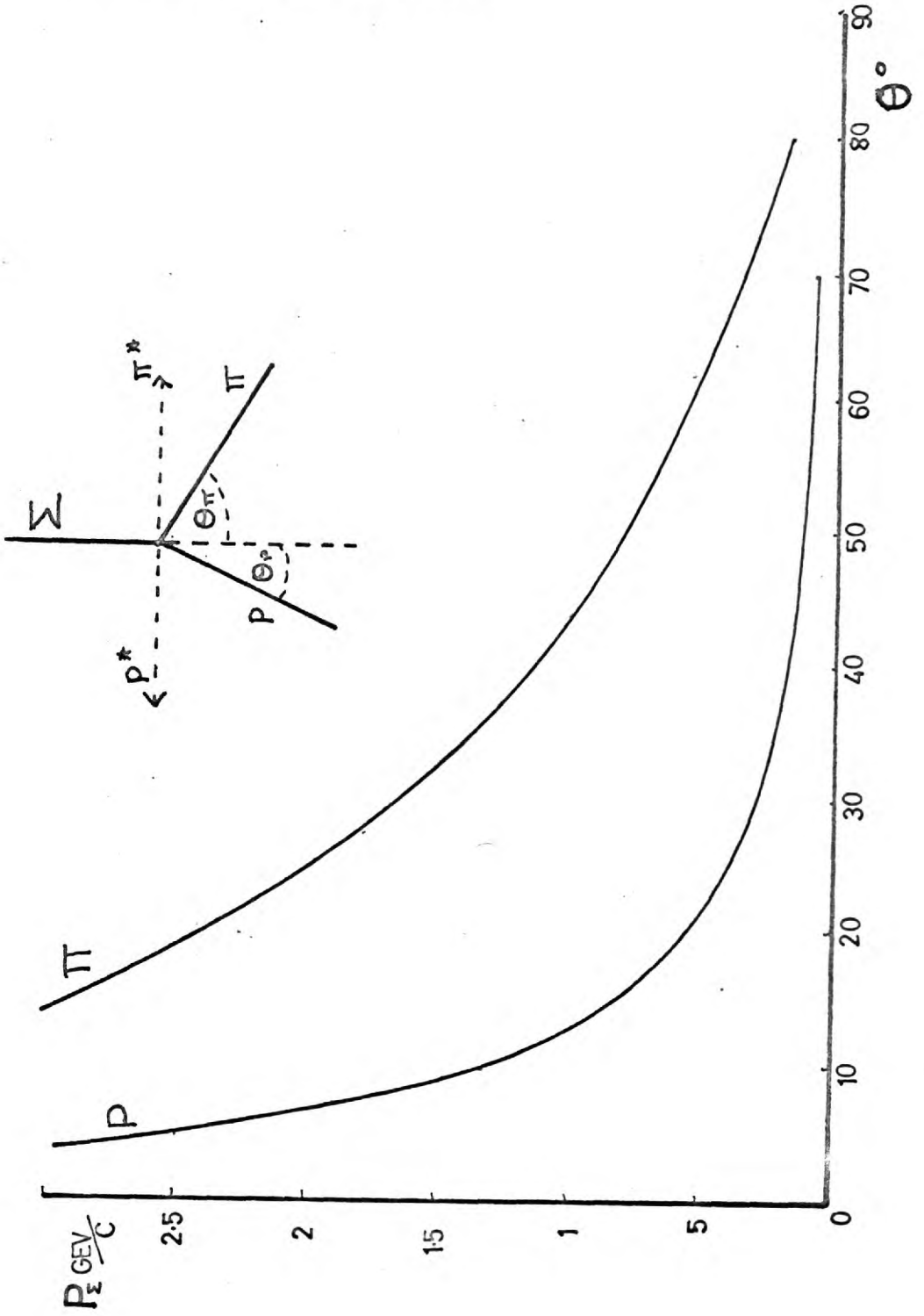

particles which are not visible even if they occur in the chamber, the other that one decay mode is easier to detect than another.

In the case of lambdas this ratio of $\frac{\text{charged}}{\text{neutral}}$ decays is well known and it is expected to be identical for antilambdas. In this experiment they can both be calculated from the observed numbers of 002's and 001's.

Sigma pluses can decay into one of two modes $\Sigma^+ \rightarrow p + \pi^0$ $\rightarrow n + \pi^+$. Figure 5•0 shows such a decay and for these two cases a plot of the opening angle versus sigma momentum. This angle certainly has a bearing on the ease of observing a decay although it is difficult to determine quantitatively. One would expect that losses would occur more easily when the nucleon rather than the pi meson was visible.

5.4 Scanning Biases

These can occur because of criteria adopted to chose a certain event class or in the preferential observation of a given class.

Of the criteria already described only the one used to chose electron pairs provided any bias. This was due to the fact that although the $^f/_L$ criteria was used, for the event classes under discussion all events were measured.

The electron pair criteria caused 1% of all $\Lambda + \overline{\Lambda}$'s in the momentum range 1•4 $\rightarrow$ 2 Gev/c to be rejected as electron pairs. It was found however that only a few percent of $\Lambda + \overline{\Lambda}$'s had such a momentum. This correction was negligible compared with the Poisson errors.

FIG 5·1

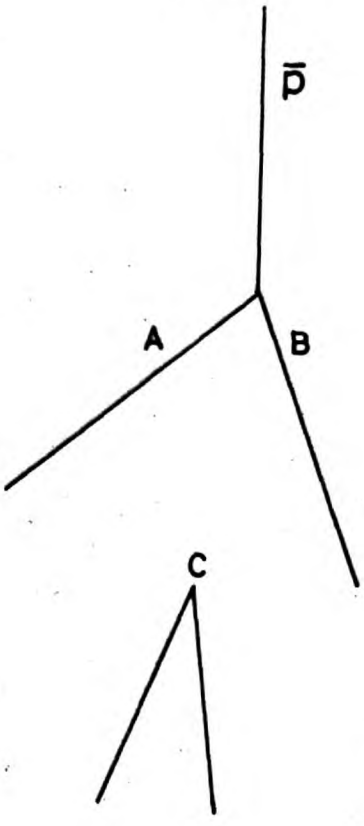
$\bar{p}$
A
B
C


1 event

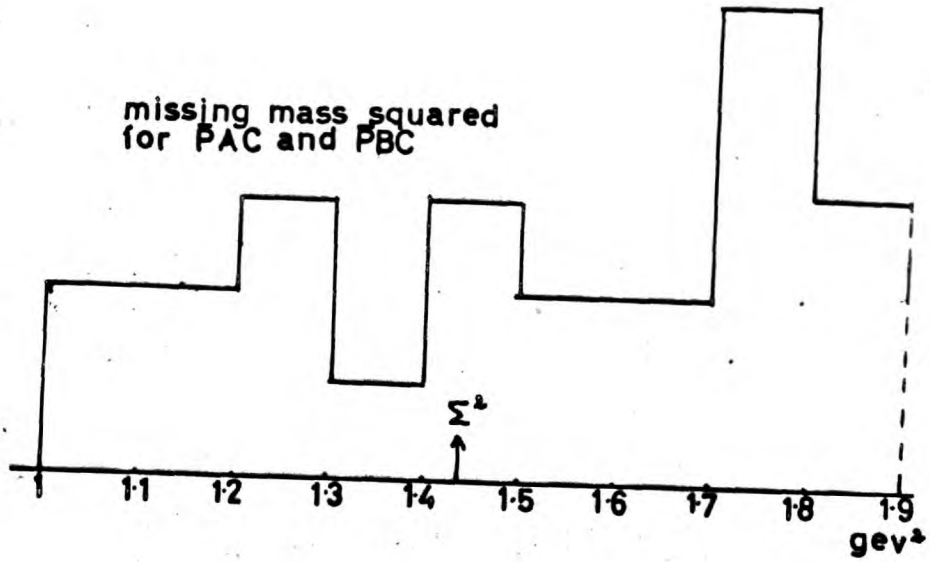
missing mass squared
for PAC and PBC
Σ^2
1
1·1
1·2
1·3
1·4
1·5
1·6
1·7
1·8
1·9
gev²

Each event with one visible decay was carefully examined for other possible associated decays. In this way it was hoped that no event with two decays was lost.

A further check on this was made in the 201's to see if any could be interpreted as 211's in which the sigma had decayed in an unobservable manner. As the majority of 211's were interactions involving no missing neutrals, the 201's were checked to see if one of the charged particles emanating from the event could be interpreted as a sigma or its decay product. This was done by calculating a missing mass squared using the neutral particle decay, the initial state particles, and one of the charged final state particles as a pi meson. This was done twice for each event taking firstly the positive, then the negative particle. Figure 5.1 shows a plot for all 201's containing a hyperon decay. No clustering of values is seen at the sigma squared mass and indeed only one event was consistent with being in effect a 211. In this particular case the event was compatible with the charged particle decay having taken place within one millimetre of the production apex. Such events had already been taken account of in the weighting applied to the 211's.

No such technique could be applied to look for 220's in the 210 class, as the latter class had not been analysed. It was hoped, however that no serious losses had occurred.

A check was then made to see if biases existed in the observation

FIG 5·2

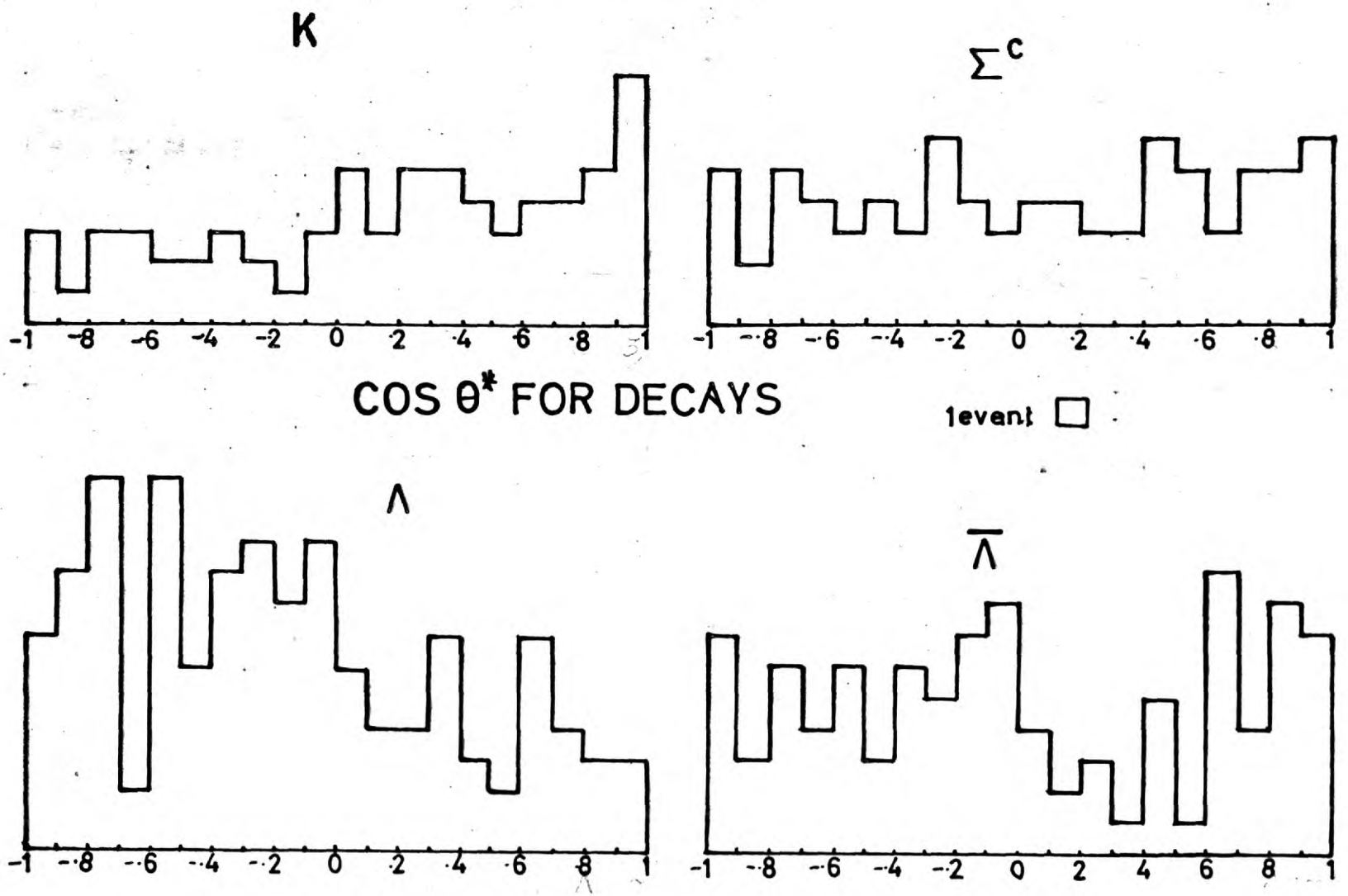

of particular particles. This was done by plotting histograms of the decay angles of the observed particles. In a two body decay the two particles are emitted in the 'parent' particles rest system in opposite directions. The angle between this direction and the 'parents' line of flight in the laboratory is the decay angle.

For the hyperon decays the angle of the nucleon with respect to the line of flight was always taken, and the π^+ was used for the K^o decays. The distributions obtained are shown in Figure 5.2. These contain all the events of our group, sufficient statistics not being available to look at different event types and decay modes separately.

Distributions of decay angles from particles produced in strong interactions are isotropic in units of Cos θ^* providing parity is conserved at production. (cf Appendix 5). Parity conservation is expected to hold[18] and previous experimental evidence has been in agreement with this. Any deviation from symmetry, therefore, is expected to reflect biases in the data.

As can be seen both the lambda and K^o distributions do differ significantly from the expected distributions. This suggested possible misinterpretation between these two classes. A thorough check was made of all fits to see if this was the case: it was proved conclusively that no misinterpretation had occurred.

The author was then responsible for combining all the data from all groups in order to investigate these deviations further. Unfortunately

FIG 5·3

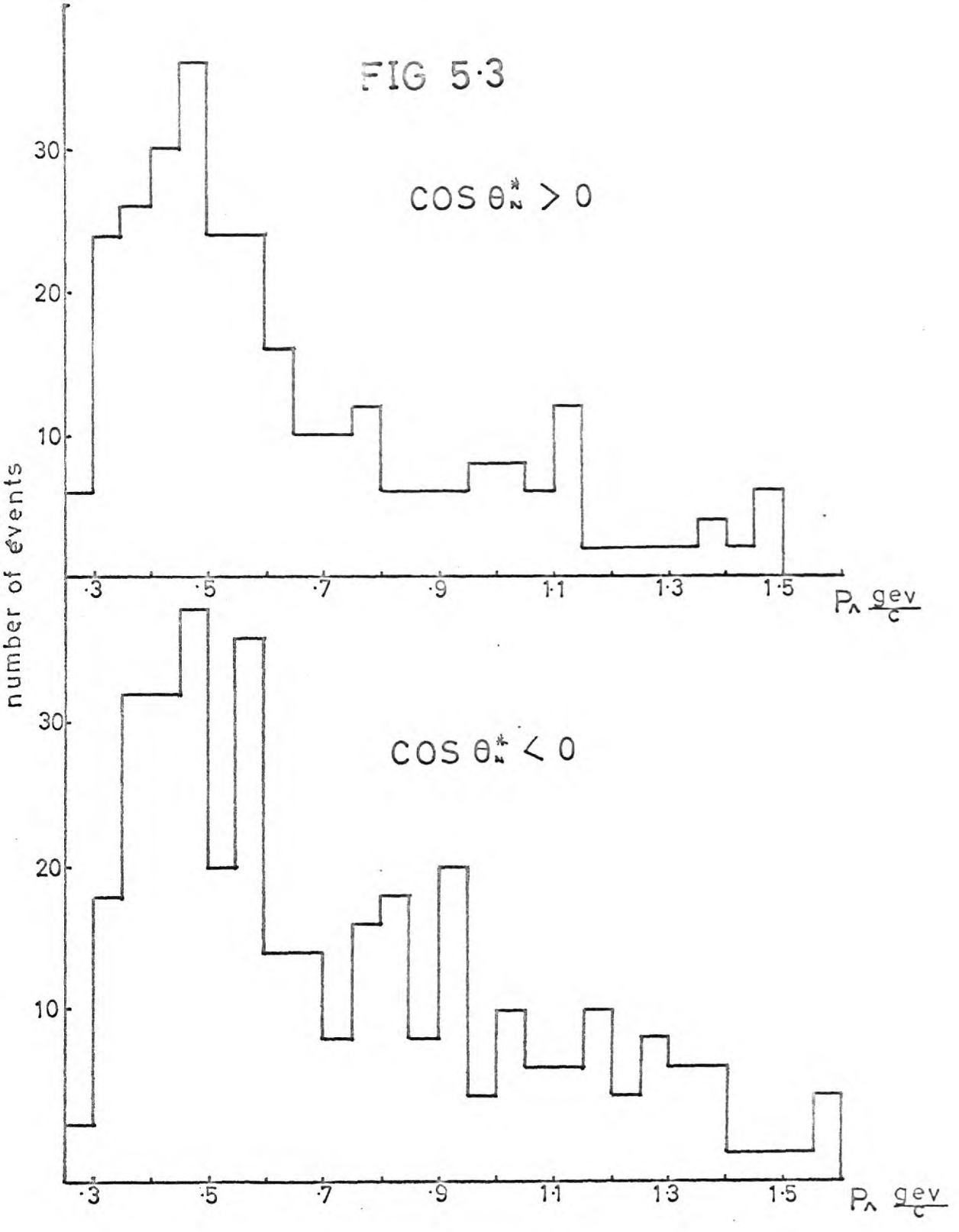
$\cos\theta^*_N > 0$
$\cos\theta^*_N < 0$
number of events
30
20
10
·3
·5
·7
·9
1·1
1·3
1·5
P_Λ $\frac{gev}{c}$

only the data for the hyperons was accessible but as no correlation between these and the K^{O} distributions had been found, this was not too serious. The combined data exhibited similar deviations as those of Figure 5.2.

It was possible that during scanning particular configurations could have been missed, e.g. wide opening angle decays. If this had been the case losses would tend to occur in particular regions of lambda momentum. Figure 5.3 shows the distributions of lambda momentum for $\text{Cos } \theta^{*} \geq 0$ and $\text{Cos } \theta^{*} < 0$. These are very similar in shape, differing in magnitude more or less equally over the whole range of momentum. This seemed to exclude the possibility of scanning losses accounting for the whole deviation.

Another possibility was that incorrect reconstruction of the decays could have caused such a shift. The lambdas having an average momentum of •5 Gev/c give rise to decay protons of $\sim$•4 Gev/c. At this latter momentum the residual track is beginning to differ significantly from a true helix. In such circumstances the reconstruction was known to be incorrect, the momentum as calculated from the reconstructed curvature being $\sim$20 Mev/c too small. The kinematics of the lambda decay at •5 Gev/c indicate that if the decay proton's momentum is underestimated, so will the lambda momentum be, by almost the same amount. In such a case the calculated decay angle will shift away from its true value towards negative $\text{Cos } \theta^{*}$, the shift in θ^{*}

FIG 5·4

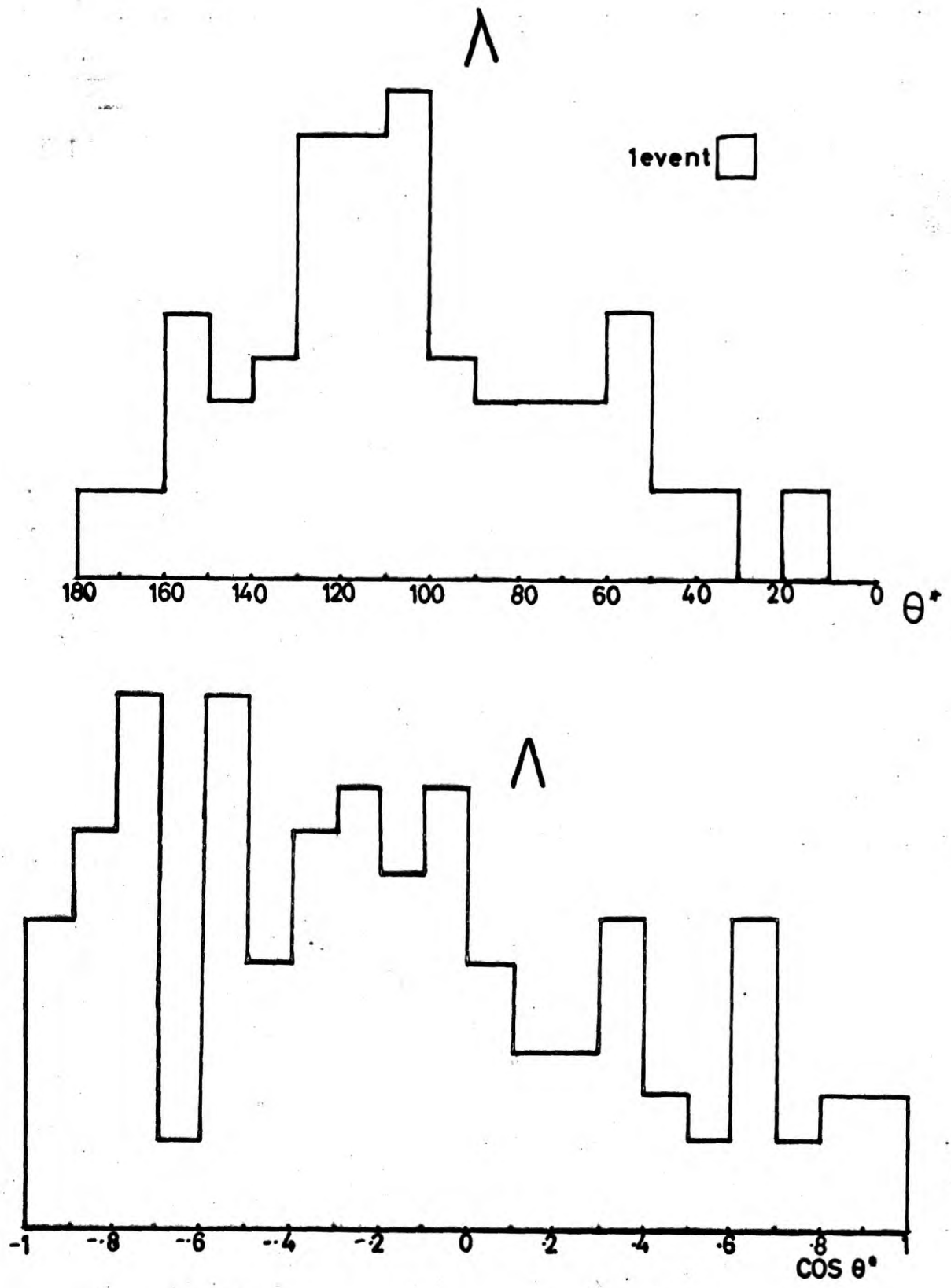

being proportional to the underestimation in momentum. Figure 5.4 shows the lambda decay angle in units of θ^* the maximum occurring at 117^o instead of 90^o. Such a shift implies an underestimation of 150 Mev/c which cannot be attributed to the reconstruction error. It was concluded, therefore, that incorrect reconstruction was not the cause of the observed deviation.

The K^o distribution of decay angle is also difficult to interpret as it has a symmetrical decay $K^o \rightarrow \pi^+ + \pi^-$. It would be expected, therefore, that any bias would also be symmetrical. The only apparent difference is that for low momentum a π^+ decays, $\pi^+ \rightarrow \mu^+ + \nu$ whereas a π^- is captured in the hydrogen. This gives rise to different configuration of decays one of which could be more difficult to observe. The available phase space for producing low energy pi mesons in the K^o momentum spectrum observed is very small, however, and does not seem capable of accounting for the observed deviation.

The above analysis seems to indicate that although some scanning losses could have occurred these are probably masked by a statistical fluctuation.

5.5 Check on Correct Weighting

The probability of an unstable particle decaying in an interval dt is independent of how long it has already lived. If N particles are produced, therefore, the number decaying at any point is just proportional

to the number still 'alive' at that point. The probability of a particle not having decayed after a time $^{Lm}/_{Pc}$ is $e^{-Lm/Pc\tau o}$.·. if N particles are produced, N' are left after a time $^{Lm}/_{Pc}$, $N' = Ne^{-Lm/Pc\tau o}$. A histogram of Log N' versus $^{L}/_{P}$ should, therefore, have a slope of $^{m}/_{Pc\tau o}$. Figure 5.5 shows these histograms for lambdas and antilambdas, the dotted lines showing the expected slopes. Because decays were only measured within the chamber and at distances further from the production apex than 3 mm, the losses at high and low $^{L}/_{P}$ were expected. These event losses are taken into consideration in the weighting process. It was verified that the lost portions of these histograms were equal, within the errors, to those events added by weighting.

5.6 Branching Ratio Calculations

The number of events available in this experiment were not sufficient to improve upon previous determinations of the hyperon branching ratios. The observed events were used to check that our data was consistent with previous determinations and that no biases had occurred in the observation of any particular decay mode. A check was also made to see that the antihyperon branching ratios were in agreement with the predictions of charge conjugation[19], i.e. in having the charge conjugate decay modes of the hyperons with the same branching ratios.

(a) Sigma, Antisigma branching ratios

These were obtained from the reaction $\bar{p} + p \rightarrow \sum + \sum + n\pi^{o} (n=0,1)$.

FIG 5·5

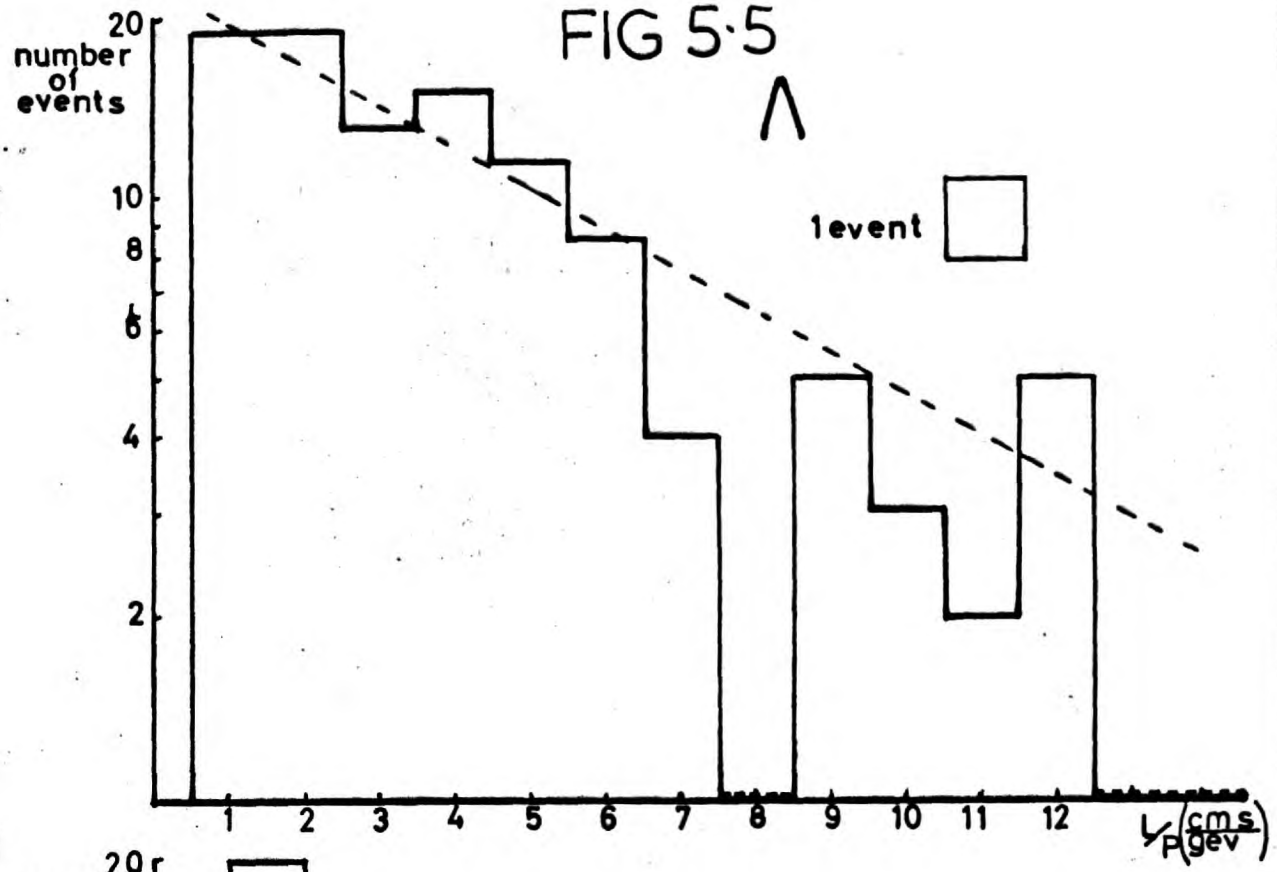
20
number of events
10
8
6
4
2
Λ
1event
1 2 3 4 5 6 7 8 9 10 11 12
1/P (cms/gev)

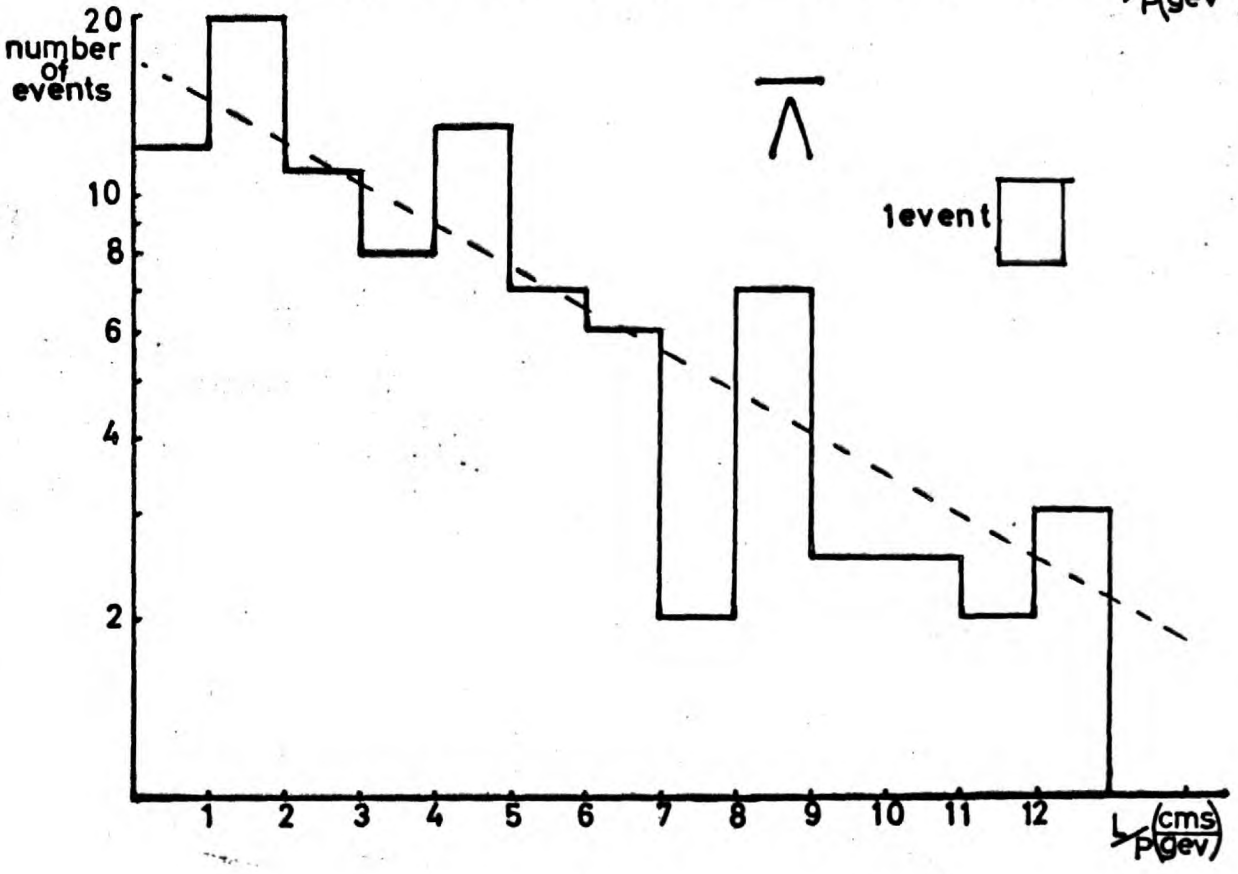
20
number of events
10
8
6
4
2
Λ̄
1event
1 2 3 4 5 6 7 8 9 10 11 12
1/P (cms/gev)

Previous experiments[20] had shown that the sigma plus has two dominant decay modes ($\Sigma^+ \rightarrow \begin{matrix} p + \pi^o \\ n + \pi^+ \end{matrix}$) whereas the sigma minus only one ($\Sigma^- \rightarrow n + \pi^-$). The corresponding antiparticles should therefore decay, $\overline{\Sigma^+} \rightarrow \begin{matrix} \bar{p} + \pi^o \\ \bar{n} + \pi^- \end{matrix}$ and $\overline{\Sigma^-} \rightarrow \bar{n} + \pi^+$.

There were therefore four classes of 220's corresponding to the two visible particles left after both decays. These were:-

		Event Numbers
A	$p + \bar{p}$	$N_1 = 20$
B	$\bar{p} + \pi^+$	$N_2 = 30$
C	$p + \pi^-$	$N_3 = 30$
D	$\pi^+ + \pi^-$	$N_4 = 69$

It is not necessary to weight the event numbers as the mode of decay is independent of momentum or distance travelled. The first three classes contain only the reactions

$$\bar{p} + p \rightarrow \Sigma^+ + \overline{\Sigma^+} + n\pi$$

whereas the last class contains a mixture of this reaction with

$$\bar{p} + p \rightarrow \Sigma^- + \overline{\Sigma^-} + n\pi.$$

The branching ratio of the Σ^+ into the $p + \pi^o$ mode is seen to be $\frac{N_1}{N_1 + N_2}$ and similarly for the $\bar{p} + \pi^o$ mode of the $\overline{\Sigma^+}$. The values obtained are $\Sigma^+ \rightarrow p + \pi^o = \cdot40 \pm \cdot07$ and $\overline{\Sigma^+} \rightarrow \bar{p} + \pi^o = \cdot40 \pm \cdot07$ both results being compatible with the accepted values of $\cdot5$. The lowness of both these ratios could well be due to a slight bias in class A which is by far the most difficult to observe at the scanning stage.

(b) Lambda, Antilambda branching ratios

The approach here is rather different as in each case one of the decay modes is into all neutrals and hence unobservable. Consider the reaction $\bar{p} + p \longrightarrow \Lambda + \bar{\Lambda}$, the probability of seeing the lambda decay in the chamber is $\Gamma_\Lambda (1 - e^{-Lm/Pc\tau_o})$ where Γ_Λ is the branching ratio into the visible mode; similarly for the antilambda. The probability of seeing this interaction as an 002 is $\Gamma_\Lambda \Gamma_{\bar{\Lambda}} (1 - e^{-Lm/Pc\tau_o})_\Lambda (1 - e^{-Lm/Pc\tau_o})_{\bar{\Lambda}}$. Replacing the kinematic factors by P_Λ and $P_{\bar{\Lambda}}$ gives $P_{002} = \Gamma_\Lambda \Gamma_{\bar{\Lambda}} P_\Lambda P_{\bar{\Lambda}}$. The probability of seeing the reaction as an 001 with a visible lambda (00^Λ) is $\Gamma_\Lambda P_\Lambda (1 - \Gamma_{\bar{\Lambda}}) + \Gamma_\Lambda P_\Lambda \Gamma_{\bar{\Lambda}} (1 - P_\Lambda)$. This is the sum of two terms, the probability of seeing the lambda with the antilambda decaying into the neutral mode, and of seeing the lambda with the antilambda decaying into the charged mode, but outside the chamber. A similar equation gives the probability of seeing an $00^{\bar{\Lambda}}$. The situation is rather more complicated than this as the 002's and 001's come from the reactions

$$\bar{p} + p \rightarrow Y + \bar{Y}, \qquad Y + K + \bar{n}, \qquad \bar{Y} + K + n, \qquad K + K \ .$$

The above technique for deriving the probabilities can be applied to each reaction separately. The values of the branching ratios were then used together with the calculated kinematic factors from the weighting process. In this way it was possible to predict from the 002's the number of events expected in each of the classes 00^Λ, $00^{\bar{\Lambda}}$, 00^K.

Using results from all groups it was found that whereas the $00\bar{\Lambda}$'s and 00K's agreed with the prediction, the 00Λ's did not, there being a significant excess of such events.

It was found, however, that if a shortened fiducial region was taken better agreement was obtained. The reason for this is probably the high average momentum of antilambdas, the mean free path being $\sim$ 23 cms. The original fiducial volume went to within 10 cm of the bottom of the chamber, which means that the weighting process is subject to much larger statistical fluctuation, than for a shorter region.

Even after reducing the fiducial volume there was still an excess of 00Λ's, however, which could have been caused if K^- particles were present in the beam. This seems unlikely as an estimate from the beam designers gives $\ll 1\%$ K^- in the beam. Also at lower energies the ratio $K^- \longrightarrow \frac{\Lambda + \text{neutrals}}{\Lambda + \pi^+ \pi^-} \sim \frac{1}{2}$ which means a large excess of lambdas should have been seen in the 201's, which was not the case.

5.7 Misinterpretation of Events

The main cause of misinterpretation is due to the inability of being able to fit more than one missing neutral particle.

The analysis below deals with a specific type of event but similar procedures were applied throughout the event types.

Determination of $\bar{p} + p \longrightarrow \Sigma^o + \bar{\Sigma}^o$ cross section

The reaction $\bar{p} + p \longrightarrow \Sigma^o + \bar{\Sigma}^o$ proceeds $\sim 10^{-20}$ secs into

$\Sigma^{o} + \overline{\Sigma^{o}} \rightarrow \Lambda + \overline{\Lambda} + \gamma + \gamma$ hence even if the subsequent decays of the Λ and $\overline{\Lambda}$ are seen the reaction cannot be fitted. Due to measurement errors however it is possible that such an event could be fitted as $\overline{p} + p \longrightarrow \Lambda + \overline{\Lambda} + \pi^{o}$ or $\Lambda + \overline{\Lambda} + \gamma$. It was necessary therefore to extract from the observed 002's the fraction due to $\overline{p} + p \longrightarrow \Sigma^{o} + \overline{\Sigma^{o}}$ using information not used explicitly in the fitting. This was done by computing for each 002 two missing mass squareds by firstly treating it as a 00_{Λ} then as a $00\overline{\Lambda}$. These two values $\mu^{2}{}_{\Lambda}$ and $\mu^{2}{}_{\overline{\Lambda}}$ where then plotted against each other. Calculations were then made to find the boundaries on such a plot within which points from various reactions must lie.

Figure 5.6 shows the various reactions and defines the quantities used in the calculation.

(a) $\overline{p} + p \longrightarrow \Lambda + \overline{\Lambda}$

$\mu^{2}{}_{\Lambda}$ should equal $M^{2}{}_{\overline{\Lambda}}$ and $\mu^{2}{}_{\overline{\Lambda}}$ should equal $M^{2}{}_{\Lambda}$. All points due to this reaction should lie ideally at one point. Due to measurement errors however, there is a certain spread about this point.

(b) $\overline{p} + p \longrightarrow \Lambda + \Sigma^{o}$ or $\overline{\Lambda} + \Sigma^{o}$

Looking at this reaction in the rest system of the $\overline{\Sigma^{o}}$ one can see that:-

$$\mu^{2}{}_{\overline{\Lambda}} = \left(\sqrt{P^{*2} + M_{\Lambda}{}^{2}} + P'\right)^{2} - \left(P^{*2} + P'^{2} + 2P^{*}P' \cos\theta\right).$$

For a given available energy in the overall C.M.S., P^{*} and P' are constant and therefore $\mu^{2}{}_{\overline{\Lambda}}$ has a maximum value at $\theta = 180^{o}$ and a minimum at $\theta = 0^{o}$.

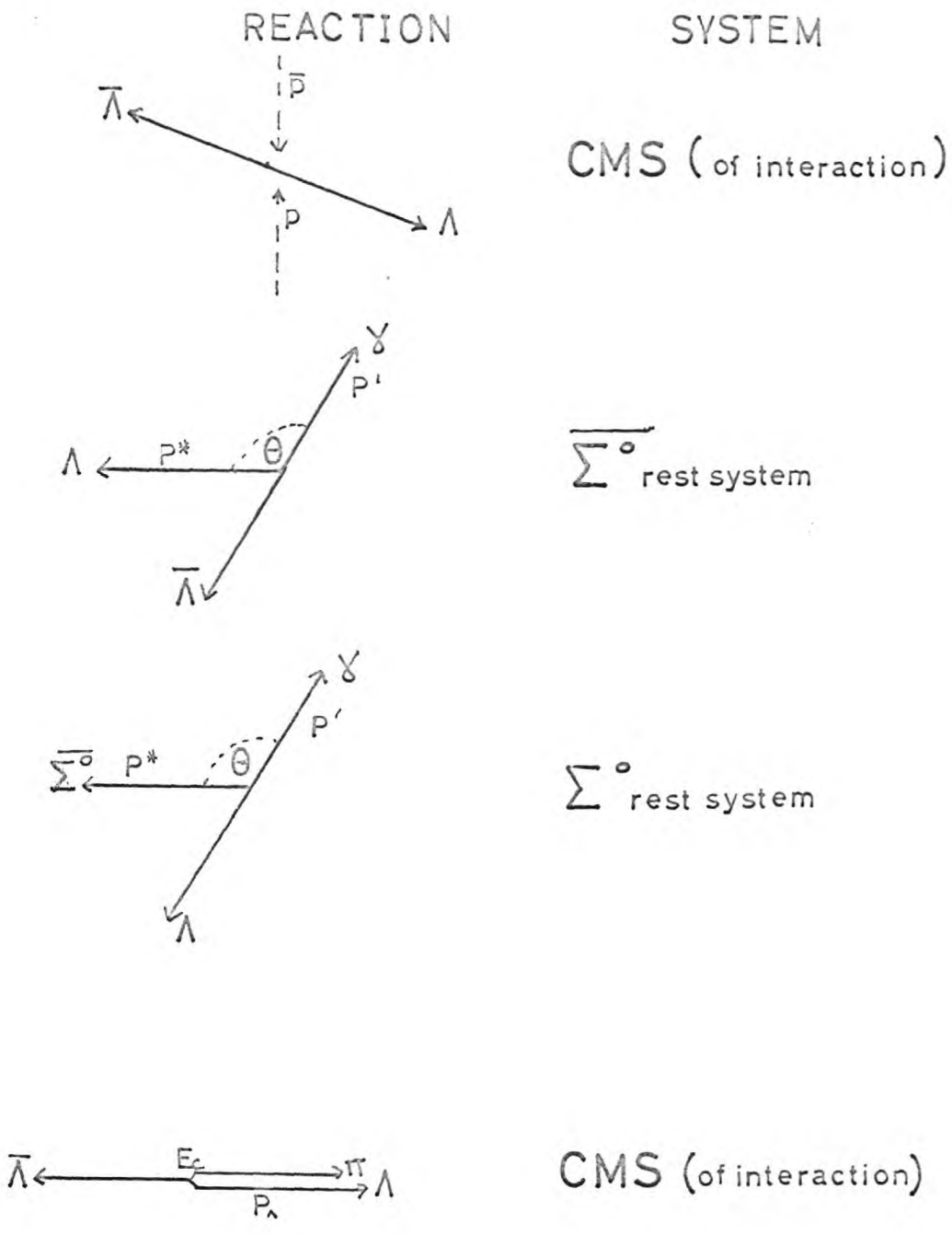
REACTION
SYSTEM
$\bar{p}$
$\bar{\Lambda}$
Λ
p
CMS (of interaction)
γ
P'
Λ
P*
θ
$\bar{\Lambda}$
$\overline{\Sigma^0}$ rest system
γ
P'
$\overline{\Sigma^0}$
P*
θ
Λ
Σ^0 rest system
$\bar{\Lambda}$
E_γ
π
Λ
P_Λ
CMS (of interaction)

FIG 5·6

μ^2_Λ on the other hand is always constant = $M^2_{\overline{\Sigma^0}}$. All events of the class $\Lambda + \overline{\Sigma^0}$ lie on a line parallel to the $\mu^2_{\overline{\Lambda}}$ axis and all events of the class $\overline{\Lambda} + \Sigma^0$ on a line parallel to the μ^2_Λ axis.

(c) $\underline{\overline{p} + p \longrightarrow \Sigma^0 + \overline{\Sigma^0}}$

This is a symmetrical system and the boundary on the μ^2 plot is symmetrical to the axes. Looking at the reaction from the rest system of the Σ^0 we find:-

$\mu^2_\Lambda = (\sqrt{P^{*2} + M^2_{\overline{\Sigma}}} + P')^2 - (P^{*2} + P'^2 + 2P^*P' \text{ Cos } \theta)$ once again P^*, P' are constant and μ^2_Λ can lie anywhere between the limits defined by Cos $\theta = \pm 1$. In this reaction, however, $\mu^2_{\overline{\Lambda}}$ can also lie between the same limits on the other axis. The allowed region is, therefore, a square.

(d) $\underline{\overline{p} + p \longrightarrow \Lambda + \overline{\Lambda} + \pi^0}$

The boundary condition in this case is for the Λ, $\overline{\Lambda}$ and π all to travelling along the same line in the overall c.m.s. As the momentum vectors of each are varied keeping $\sum \overline{P} = 0$ and $\sum E$ constant the boundary of a normal Dalitz plot is circulated.

Dalitz plots[21] for three body final states are very often represented using kinetic energies. In this case one would plot T_Λ versus $T_{\overline{\Lambda}}$. Using Figure 5.6 it is seen that $M^2_{\overline{\Lambda}\pi} = (Ec - E_\Lambda)^2 - P_\Lambda^2$ where Ec is the available energy in the overall c.m.s.

$\therefore M^2_{\overline{\Lambda}\pi} = Ec^2 - 2Ec\ E_\Lambda + E_\Lambda^2 - P_\Lambda^2$

$= Ec^2 - 2Ec\ (T_\Lambda + M_\Lambda) + M_\Lambda^2$

$\therefore M^2_{\overline{\Lambda}\pi} \propto T_\Lambda$ and all the properties possessed by a $T_\Lambda - T_{\overline{\Lambda}}$ plot

are possessed by a $\mu^2 \Lambda - \mu^2 \bar{\Lambda}$ plot.

(e) Density of points

With all the above reactions μ^2 is seen to be proportional to Cos Θ (as defined in Figure 5.6). Providing the probability for decay into each element of solid angle is constant then the density of points is isotropic in units of Cos Θ^*. This is so for the decay of a Σ^0 ($\overline{\Sigma}^0$), therefore, an isotropic distribution of points is expected along the $\Lambda \Sigma^0$ lines and within the $\Sigma^0 \overline{\Sigma}^0$ square. The density due to the $\Lambda \bar{\Lambda} \pi^0$ events is more difficult to predict due to the presence of resonances etc.

(f) Experimental Distribution

The distribution found at the three incident momenta are shown in Figures 5.7, 5.8 and 5.9. The μ^2's are calculated from the reconstructed single vertex fits of the Λ and $\bar{\Lambda}$, but the final kinematic fits found by GRIND are also indicated. As can easily be seen the fitting agrees very well with the measurements. A cluster of points occurs around the $\Lambda \bar{\Lambda}$ point and the $\Lambda \Sigma^0$ events do lie along the appropriate lines. It is rather more difficult to calculate the fraction of events which are really $\bar{p} + p \longrightarrow \Sigma^0 + \overline{\Sigma}^0$. An upper limit can be placed on this by assuming all the points inside the square are of this type. It is possible to take a more realistic approach in assigning events into the various channels. By excluding an area of the

FIG 5·7

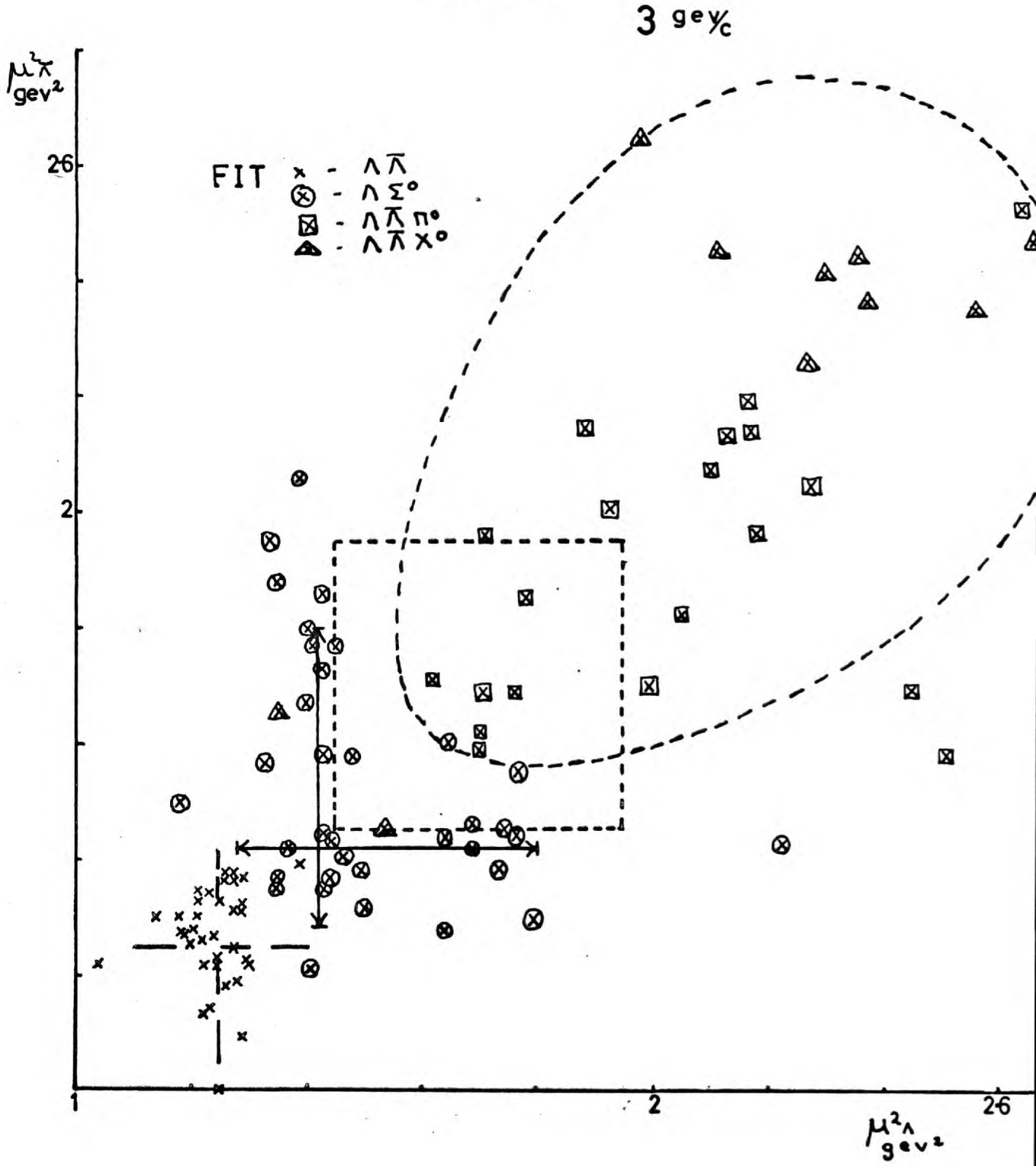

FIG 5·8

3·6 gev/c

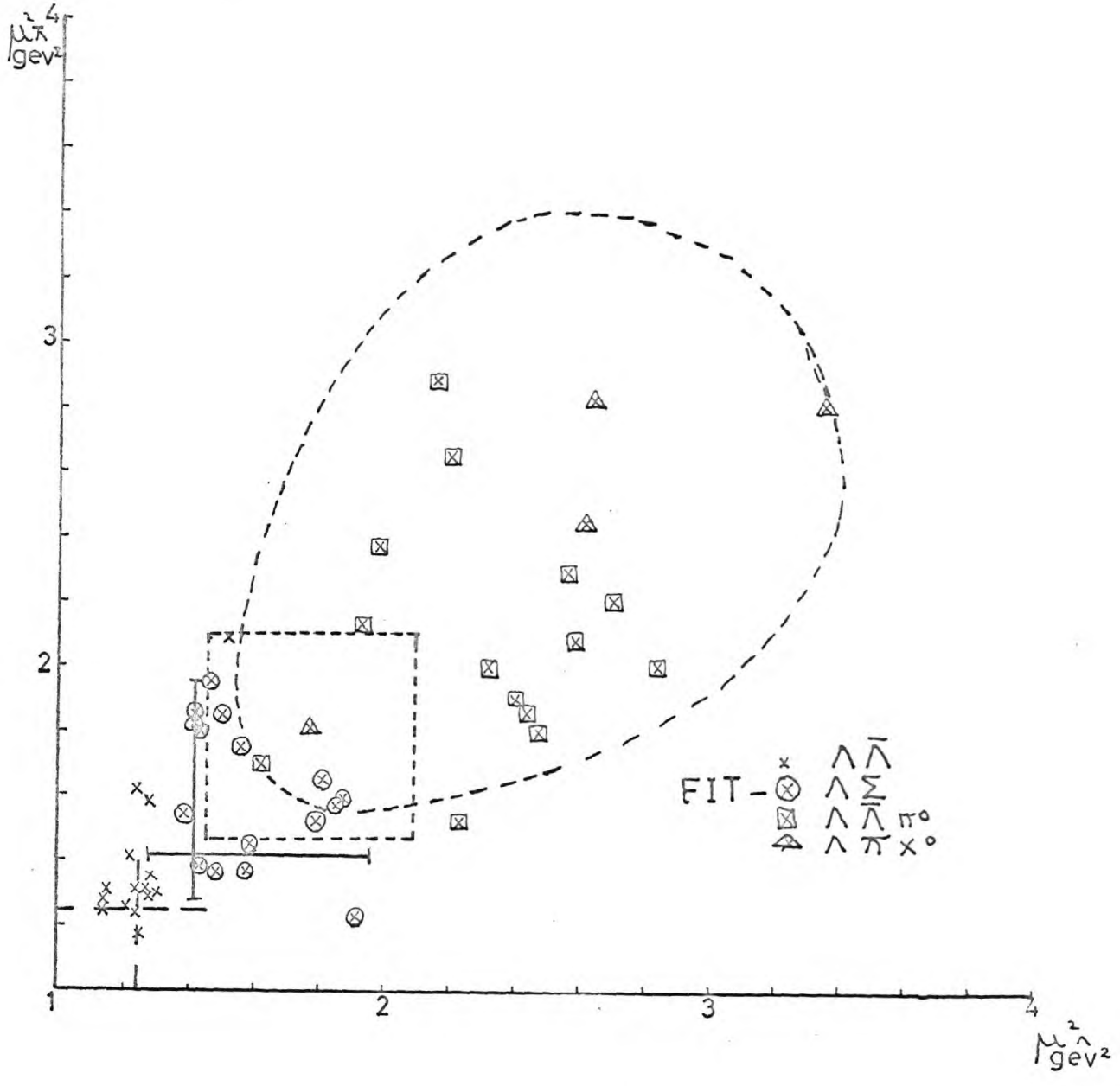

FIG 5·9

4 gev/c

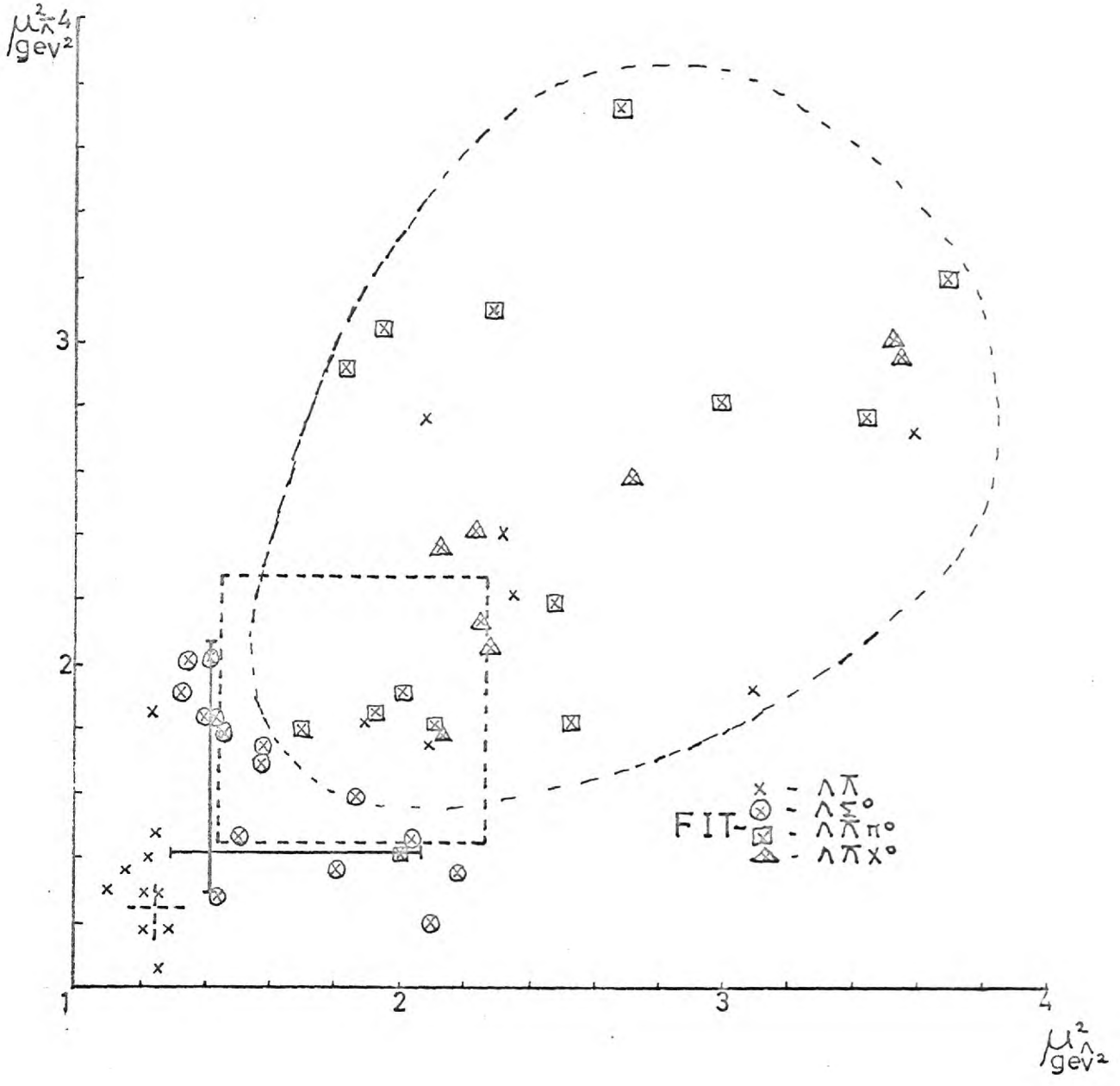

square near the $\Lambda\pi$ lines and extrapolating the density of points in the $\Lambda\Lambda\pi$ distribution outside the square, it appears that less than half the experimental points are due to $\Sigma^0 + \overline{\Sigma^0}$ production. A better estimation is not possible with the limited statistics available.

The plots show best of all the correctness of the assignments by the fitting programme.

5.8 Summary of Biases

The analysis above indicates that biases do exist in the combined data. Unfortunately no quantitative answer could be obtained for these deviations.

It was felt that the biases in the events with two decays were likely to be very much smaller than when only one had been observed. All events with only one decay were checked visually, and where possible kinematically, for other associated decays.

The following analysis is based purely on the two decay events and the only corrections applied are kinematic weighting and neutral decay modes. An extra correction was made in the events with a visible hyperon plus K meson decays to take into account $\sim 1\%$ π mesons contaminating the beam which can produce interactions of the type $\pi^- + p \longrightarrow \Lambda + K$.

5.9 Calculation of Cross Sections

All the cross-sections were calculated using those events with two visible decays. Following the notation of section 5.6 we can write the

probability of seeing two decays as $\Gamma_1\ \Gamma_2\ P_1\ P_2$ where Γ_1, Γ_2 are branching ratios into the visible modes and P_1 and P_2 are the kinematic factors. The observed number of events $N' = \sum_1^N \Gamma_1\ \Gamma_2\ P_1\ P_2$ where N events were truly produced. The weight of decay one is $1/P_1$ and of decay two $1/P_2$ $\therefore\ \Gamma_1\ \Gamma_2\ N = N' \sum W_1\ W_2$ $\therefore\ N = \frac{N'}{\Gamma_1\Gamma_2}$ x Weighted number observed

Γ_1 and Γ_2 were values known from previous experiments and the weights were calculated from the decay parameters. The formula to calculate a cross-section σi is

$$\sigma i = \frac{\text{(Total events produced)}}{\text{(Total track length) (Density of hydrogen) (Avogadros number)}}$$

The total length of beam track was calculated from the beam count at scanning and the length of fiducial volume used. The density of hydrogen used was that calculated by the chamber crew and independently checked at CERN.

Within the available statistics the cross-sections for a reaction and its charge conjugate were found to be equal and have not therefore been quoted separately.

$\underline{\bar{p} + p \longrightarrow \Sigma^- + \overline{\Sigma^-}}$ cross-section

The events in this class come from class D(cf Section 5.6) which also contains events of the class $\bar{p} + p \longrightarrow \Sigma^+ + \overline{\Sigma^+}$ (1). If branching ratios of ·5 are taken for the Σ^+ and $\overline{\Sigma^+}$ the expected number of events due to reaction (1) are in the ratio 1 : 1 : 1 : 1 for classes

A : B : C : D. Two approaches can be adopted, one is to decide no biases exist in classes A : B : C and optimize from the observed numbers in these classes the number expected in class D. The other is to estimate any biases present and then recalculate the number of events in D. The cross-sections quoted have been calculated using the former method. The correctness of doing this will be discussed with the derivation of the $\Sigma^- - \overline{\Sigma^-}$ angular distribution (cf P92)

Cross-Sections

Reaction Channel	3 Gev/c	3·6 Gev/c	4 Gev/c
$\Lambda\ \bar{\Lambda}$	123 ± 17	74 ± 18	38 ± 12
$\Lambda\ \bar{\Sigma}^{\circ}$	108 ± 16	62 ± 16	45 ± 13
$\Sigma^{\circ}\ \bar{\Sigma}^{\circ}$	<18	<41	<60
$\Sigma^{+}\ \bar{\Sigma}^{+}$	30 ± 5	21 ± 5	20 ± 5
$\Sigma^{-}\ \bar{\Sigma}^{-}$	8 ± 6	11 ± 6	9 ± 6
$\Xi^{-}\ \bar{\Xi}^{-}$	2 ± 1	<1	<1
3 body final States			
$\Sigma^{+}\ \bar{\Lambda}\ \pi^{-}$	60 ± 10	75 ± 13	50 ± 10
$\Sigma^{-}\ \bar{\Lambda}\ \pi^{+}$	27 ± 5	36 ± 12	25 ± 8
$\Sigma^{+}\ \bar{\Sigma}^{o}\ \pi^{-}$ / $\Sigma^{-}\ \bar{\Sigma}^{o}\ \pi^{+}$	25 ± 6	19 ± 6	43 ± 9
$\Lambda\ \bar{\Lambda}\ \pi^{\circ}$	56 ± 11	66 ± 16	64 ± 14
$\Lambda\ \bar{\Lambda}\ \chi^{\circ}$	19 ± 7	17 ± 7	32 ± 11
$\Lambda\ K^{\circ}\ N^{\circ}$	34 ± 12	45 ± 18	65 ± 20
$\Lambda\ K^{c}\ N^{c}$	26 ± 9	18 ± 6	45 ± 14
4 body final States			
$\Sigma^{c}\ \Lambda\ \pi^{c}\ \pi^{\circ}$	20 ± 20	21 ± 12	12 ± 4
$\Lambda\ \bar{\Lambda}^{o}\ \pi^{+}\ \pi^{-}$ / $\Lambda\ \bar{\Sigma}^{\circ}\ \pi^{+}\ \pi^{-}$	24 ± 9	58 ± 17	48 ± 9

Cross-sections are in microbarns and each channel includes a reaction and its charge conjugate.

CHAPTER 6

THE EXPERIMENTAL RESULTS

6.1 Production of Cascade-Anticascade Pairs

Prior to experiments with high energy antiprotons no examples of anticascade particles had been definitely observed. It was anticipated, however, that both the $\bar{\Xi}^-$ and $\bar{\Xi}^0$ did exist, as antiparticles had been observed for all other stable and quasi stable particles.

During the first scan of the film an example was seen of the reaction $\bar{p} + p \rightarrow \bar{\Xi}^- + \bar{\Xi}^-$. This was published[22] simultaneously with a similar interaction observed at Brookhaven[23]. No definite example was seen, however, in the entire film of an anticascade zero. Its presence could be inferred from observed interactions of the type $\bar{p} + p \rightarrow \bar{\Xi}^- + \bar{\Xi}^0 + \pi^+$ in which both the $\bar{\Xi}^-$ and the subsequent lambda were seen to decay. The antilambda from the decay of the $\bar{\Xi}^0$ was not observed. One example of the above reaction has been reported from Brookhaven[24] in which both the lambda and antilambda were observed, thus completing the expected list of antiparticles.

The event numbers observed in the various channels involving cascades were so few that no conclusions could be drawn about the mechanism of production.

6.2 Production of sigma antisigma pairs

As has been shown (cf section 5.7) the reaction $\bar{p} + p \rightarrow \Sigma^0 + \overline{\Sigma^0}$ cannot be uniquely identified and an approximate cross-section was the only quantity calculated.

The reaction $\bar{p} + p \rightarrow \Sigma^+ + \overline{\Sigma^+}$ could be identified providing one of the subsequent decays exhibited a visible nucleon (or antinucleon). If both decays had visible pi mesons, however, the possibility existed that the interaction was in fact $\bar{p} + p \longrightarrow \Sigma^- + \overline{\Sigma^-}$.

The angular distribution in the c.m.s. of the interaction, of the Σ^+ is shown in Figure 6.1 for the interactions known to be $\bar{p} + p \longrightarrow \Sigma^+ + \overline{\Sigma^+}$ (classes A + B + C, cf section 5.6). The angular distribution of the positively charged sigma (or antisigma) for the 'mixed' class is shown in diagram D. If branching ratios of ·5 are taken for the Σ^+ and $\overline{\Sigma^+}$ and it is assumed no biases exist, then the events of the type $\bar{p} + p \longrightarrow \Sigma^+ + \overline{\Sigma^+}$ in the 'mixed' class should have an angular distribution of the same shape but one third the magnitude of A + B + C. The result of this subtraction is shown in Figure 5.6 E, which is now the angular distribution of the reaction $\bar{p} + p \longrightarrow \Sigma^- + \overline{\Sigma^-}$.

The angular distribution of the Σ^+ is very sharply peaked in the backward direction, indicating that it tends to keep the character of the initial proton. The Σ^- distribution also exhibits a tendency for this to happen even though it is negatively charged.

It was expected that decays with a visible nucleon (antinucleon) would have been missed more easily at scanning than the charged pi decay mode. This is because of the small change in direction and momentum occurring in the former decay. The events subtracted, therefore, are a lower limit and could be significantly higher. If this is the case the angular distribution of the Σ^- would be even more peaked. This seems to be the most probable solution, although due to lack of knowledge of biases present, the cross-sections etc, have been calculated assuming no biases were present.

6.3 Production of neutral hyperon pairs

The angular distributions of the hyperons from the reactions $\bar{p} + p \rightarrow \Lambda + \bar{\Lambda}$ and $\bar{p} + p \longrightarrow \Lambda + \Sigma^0$ are shown in Figure 6.2. The latter has added to it the events of the class $\bar{p} + p \rightarrow \Sigma^0 + \bar{\Lambda}$. Once again the strong backward peaking can be seen.

6.4 Isobar Formation

As well as the quasi stable particles having lifetimes $\sim 10^{-10}$secs, many particles having lifetimes $\ll 10^{-20}$secs have recently been discovered. This decay time is so short that no visible decay can be seen in the bubble chamber. The presence in reactions of such particles (resonances) can be inferred by observation of preferred mass values for pairs or triplets of observed particles.

In particular in the work under discussion the presence of hyperon pion resonances was investigated in the reaction

$\bar{p} + p \longrightarrow Y + \bar{Y} + n\pi \quad (n = 1, 2)$.

(a) Three Body Final States

The usual method of showing the existence of the resonances is to draw a Dalitz plot. Figure 6.3 shows such plots of $M^2_{Y\pi}$ versus $M^2_{\bar{Y}\pi}$ for the interactions leading to $\Lambda + \Sigma^c + \pi^c$ final states. To obtain sufficient data events from all three momenta have been combined. This can be done on an M^2 plot as the position of any resonance is unaffected by the available c.m.s. energy. The existence of known resonances is marked and as can be seen significant production of each occurs. Due to the bands crossing on the plot the estimation of the fraction of events being produced in the resonance channels is complicated. This is because of possible interference effects in such crossing regions. The dotted lines shown indicate the available phase space at the three momenta. The full lines show the expected widths of the resonances[25].

Figure 6.4 shows projections on the two axes with the dotted line showing phase space. This shows clearly the significant production of the three resonances. Both Figures 6.3 and 6.4 contain all events of the class $\Lambda + \Sigma^c + \pi^c$ irrespective of whether the Σ^c is $\pm$ or an antiparticle. Figure 6.5, however, does show these projections for the particle and antiparticle combinations separately. As can be seen the distributions are very similar, the resonances being produced with

equal magnitude and widths in the two channels. Other projections from Dalitz plots for reactions of the type $\bar{p} + p \rightarrow Y + \bar{Y} + \pi$ are shown in Figures 6.6 and 6.7. These once again exhibit resonance formation.

Using the events lying within the resonance bands it is now possible to plot angular distributions for the pseudo two body processes $\bar{p} + p \longrightarrow Y + \bar{Y}^{*}$ or $\bar{Y} + Y^{*}$. These are shown plotted for the antisystem from the reactions in Figures 6.8 and 6.9. Once again the striking feature is the forward peaking of the antiparticle.

It is possible by using the known properties of Dalitz plots, to assign on a statistical basis, the events in the crossing region of two resonances into the two channels[26]. This has been done and the partial cross-sections found are:-

Reaction		σY_1^{*} μb	σY_{01}^{*} μb	σY_{02}^{*} μb
$\bar{p} + p \rightarrow$	$\Lambda \bar{\Lambda} \pi^{o}$	$11 \pm 2{\cdot}5$		
	$\bar{\Sigma}^{\mp} + \bar{\Lambda} \pi^{-}$	21 ± 4	17 ± 5	17 ± 5
	$\Sigma^{+} + \Lambda \pi^{+}$			
	$\bar{\Sigma}^{-} \bar{\Lambda} \pi^{+}$			
	$\Sigma^{-} \Lambda \pi^{-}$			
all	$\Sigma^{c} \Sigma^{o} \pi^{c}$	$2{\cdot}2 \pm 1{\cdot}5$	$6{\cdot}7 \pm 2$	$2{\cdot}9 \pm 1$
channels			σN^{*}	σY_{02}^{*}
all channels	ΛKN		20 ± 6	16 ± 5

This is the first experiment in which the decay $N^*_{\frac{1}{2}} \rightarrow \Lambda + K$ has been observed (mass 1688 Mev). Using the above values a branching ratio for $\frac{Y^*_{02} \rightarrow KN}{Y^*_{02} \rightarrow \Sigma\pi}$ of $\cdot 65 \pm \cdot 27$ is obtained, which is compatible with the presently accepted value of $\cdot 5$.

(b) Four Body Final States

The only class having enough events for quantitative analysis was $\bar{p} + p \rightarrow \Lambda + \bar{\Lambda} + \pi^+ + \pi^-$. In this reaction two pairs of effective masses can be formed. Invoking charge conjugation however, the $\Lambda\pi^+$ and $\bar{\Lambda}\pi^-$ distributions should be the same, as should $\Lambda\pi^-$ and $\bar{\Lambda}\pi^+$. Figure 6.10 shows a plot of these masses for both the above pairs. If a point from the first pair lies below OA it is reflected about OA, similarly if from the second pair a point lies above OA it is reflected and put below OA.

The positions of the resonances are shown, the crossing region showing where events of the type $\bar{p} + p \rightarrow \bar{Y}_1 + Y_1^*$ would lie. The projections onto the axes were made and a best fit was made using the phase spaces for $\bar{p} + p \rightarrow Y_1^* + \overline{Y_1^*}$, $Y_1^* + \bar{Y} + \pi$ (plus charge conjugate) and $Y + Y + \pi + \pi$ this being:-

$\bar{p} + p \rightarrow$	$Y_1^* \ \overline{Y_1^*}$	$40 \pm 12\%$
	$Y_1^* \bar{\Lambda}\pi + \overline{Y_1^*} \Lambda\pi$	$40 \pm 20\%$
	$\Lambda\bar{\Lambda}\pi\pi$	$20 \pm 20\%$

If we use all the events compatible with $Y_1^* \ \overline{Y_1^*}$ production one obtains

a ratio $\frac{Y_1^{*+}\ \overline{Y_1^{*+}}}{Y_1^{*-}\ \overline{Y_1^{*-}}}$ of $\frac{7}{3}$. No evidence was found for the production of a heavy meson decaying into $Y + \overline{Y}$.

6.5 Interpretation of Results

Recent experimental evidence[27] has pointed towards the importance of a long range interaction dominating some aspects of high energy elementary particle interactions. Theoretical models[28] try to interpret such aspects in terms of the exchange of one or more virtual particles, between the two particles in the initial state. Such models have had considerable success in fitting the observed data of $\pi + p$ and $p + p$ interactions.

Interactions described by such models are termed peripheral or single particle exchange interactions. In the events under consideration a particle or particles carrying strangeness must be exchanged. Although the particles exchanged are 'virtual' they can be described in terms of observed elementary particles. The least massive particles carrying strangeness are the K meson and the newly discovered K^* (Mass 880 Mev)[29] resonance. It was thought, therefore, that either of these particles could be the exchanged particle.

Figure 6.11 (a) shows a typical peripheral diagram for the reaction $\overline{p} + p \rightarrow \Lambda + \overline{\Lambda}$. Three quantities which are important in this type of interaction are the invariant four momentum transfer, the strangeness and

charge exchanged. Using Figure 6.11 we can see that Δ^2(4 momentum transfer) = $(\overrightarrow{P_P} + \overrightarrow{P_Y})^2 - (E_P + E_Y)^2$. In the c.m.s. of the interaction $\Delta^2 = P_P^2 + P_Y^2 + 2P_P P_Y \text{ Cos } \theta^* - (E_P + E_Y)^2$. For a two body final state at a given initial energy, all terms are constant, except Cos θ^*, and therefore Δ^2 distributions are very similar to the angular distributions plotted.

Figure 6.11 e, f and g show the production of two body final states for different charge exchanges. It is to be expected a priori that the cross-sections should decrease rapidly with the number of charges exchanged and with the number of units of strangeness exchanged.

(a) Fitting the results to Specific Models

If K meson exchange is assumed then it has been shown[30] that the angular distribution is proportional to $\Delta^2/\Delta^2 + m^2$ and, therefore, tends to zero at low Δ^2. This behaviour is not observed and most theoretical calculations have used K^* exchange in which this factor is $A/\Delta^2 + m^2$. Using such a model Watson[31] has predicted relationships between cross-sections and also specific forms of angular distribution.

It is found that cross-sections are proportional to the coupling constants at the two vertices. Using diagrams b, c, d (Figure 6.11) it is seen that $\sigma \Lambda \bar{\Lambda} \propto a^2$ $\sigma \Sigma \overline{\Sigma^\circ} \propto b^2$ $\sigma \Lambda \overline{\Sigma^\circ} \propto ab$

$\therefore$ $\sigma \Lambda \bar{\Lambda}$ $\sigma \Sigma \overline{\Sigma^\circ} = \sigma \Lambda \overline{\Sigma^\circ}$. Unfortunately the cross-section for $\Sigma \overline{\Sigma^\circ}$ production is difficult to estimate but it can be related to

$\sigma\ \Sigma^+\ \overline{\Sigma^+}$ by isotopic spin arguments. This gives:-

$$\sigma\ \Lambda\overline{\Lambda} \quad \sigma\ \Sigma^+\overline{\Sigma^+} = 4\ \sigma\ \Lambda\overline{\Sigma^0}^2 \qquad (1)$$

More extensive arguments based on Unitary Symmetry[32] have been used to try and find higher symmetries existing between sub groups of particles. Gell-Mann[33] has predicted using such a scheme, that the cross-sections $\sigma\ \Lambda\ \Lambda\ :\ \sigma\ \Lambda\ \overline{\Sigma^0} + \sigma\ \Sigma^0\ \overline{\Lambda^0}\ :\ \sigma\ \Sigma^+\ \overline{\Sigma^+}$ should have the ratio 9 : 6 : 4. Our results give:-

	3 Gev/c	3·6 Gev/c	4 Gev/c
$\dfrac{2\sigma\Lambda\ \overline{\Sigma^0}}{\sqrt{\sigma\ \Lambda\overline{\Lambda}\ \ \sigma\ \Sigma^+\ \overline{\Sigma^+}}}$ =	$1{\cdot}7 \pm {\cdot}2$	$1{\cdot}6 \pm {\cdot}3$	$1{\cdot}6 \pm {\cdot}4$

and $\sigma\ \Lambda\ \Lambda\ :\ \sigma(\Lambda\Sigma + \Sigma\Lambda):\ \sigma\Sigma^+\overline{\Sigma^+}$ 9 : 8 : 2·2 9 : 7·5 : 2·5 9 : 11 : 4·7

These results do indicate inconsistency with the predicted values. In all cases, if the $\Lambda\ \overline{\Sigma^0}$ cross-section was lower agreement would be reached with both predictions. This feature is a little disquieting as (1) appears to hold for most peripheral models providing all the interactions involve the same exchanged particle. The disagreement is not too significant, however, because of the large errors.

(b) Charge two exchange

If a K^* exchange model is assumed no interactions of the type $\overline{p} + p \rightarrow \sum^- + \overline{\sum^-}$ should be seen as this involves the exchange of two charges. In fact a number of such events have been seen exhibiting a fairly peripheral character, (Figure 6.1). A ratio of $\dfrac{\sum^+ \overline{\sum^+}}{\sum^- \overline{\sum^-}} \sim 3$ is observed with a similar ratio for the production of $\dfrac{Y_1^{*+}\ \overline{Y_1^{*+}}}{Y_1^{*-}\ \overline{Y_1^{=}}}$ all of these reactions being of a peripheral nature.

In the three body events the double charge exchange process was also looked for. If it exists then a number of $\bar{p} + p \rightarrow \Sigma^- + \overline{Y_1^{*-}}$ should be seen. Figure 6.12 shows the effective mass distribution from interactions of the type $\bar{p} + p \rightarrow \Lambda + \Sigma^c + \pi^c$ as can be seen there is no evidence for $\overline{Y_1^{*-}}$ or Y_1^{*-} production in the Σ^- ($\overline{\Sigma^-}$) events.

A striking feature of the reaction $\bar{p} + p \rightarrow \Sigma^- + \overline{\Sigma^-}$ is that its angular distribution is peaked indicating peripheralism but does go to zero very sharply for Cos Θ^* of the hyperon = - 1. No theoretical predictions exist for such processes as no single particle having double charge in the mass region required is known to exist.

(c) Charge Conjugate Reactions

Within the experimental errors all particles and antiparticles were produced with equal frequency momentum and spatial distributions. Thus confirming the predictions of charge conjugation invariance.

(d) Angular Distributions

All the two body final states coming from $\Delta Q = 0, 1$ $\Delta S = 1$ have strongly peaked forward backward angular distributions. These tend to broaden as the mass of the final state particles increases. This could be due to being not too far above threshold for the higher mass value reactions. Isotopic spin factors could also cause effects of this nature.

In order to compare with theoretical predictions, it is convenient to replot the angular distributions in terms of Δ^2. Figure 6.13 shows

this for all reactions of the type $\bar{p} + p \rightarrow Y^{o} + \bar{Y}^{o}$. The experimental slope appears to be rather sharper than the theoretical curve.

(e) Cross-Sections

Apart from the apparent discrepancy with predictions the cross-sections do exhibit other features. As is to be expected at each energy, the cross-section decreases with increase of number of particles in the final state. As well as this a distinct trend of decrease with increasing antiproton momentum is also apparent. This is not true of all channels, particularly those which are near threshold which would be expected to increase with available energy. Overall the cross-section for $Y\bar{Y}$ formation is a very small fraction of the total cross-section and is decreasing with increasing momentum. This is presumably due to the falling total $\bar{p} + p$ cross-section and new channels becoming available.

A further disagreement occurs in the reactions $\bar{p} + p \rightarrow \begin{matrix} \Lambda + K^{o} + n^{c} \\ \Lambda + K^{c} + n^{c} \end{matrix}$ which should have equal cross-sections. The ratio being $1{\cdot}7 \pm {\cdot}4$. The analysis is incomplete, however, and this ratio may improve. The lowness of the cross-sections of those events with a $\sum^{o}$ compared to those of a Λ^{o} is also a prediction of unitary symmetry[34].

6.6 Summary

The analysis has shown the low cross-section for hyperon antihyperon production which is dominated by peripheral processes. These

processes are in qualitative agreement with the predictions of K^* exchange and the Gell-Mann model.

The predominance of interactions involving lambdas (antilambdas) over those involving sigma (antisigma) zeros may in part be due to the low branching ratio of the Y_1^* into the $\Sigma^0\pi$ mode.

The preponderance of $\Sigma^+ \Lambda \pi^c$ over $\Sigma^- \Lambda \pi^c$ is probably a consequence of the fact that the former can be produced for $\Delta Q = 0$ or 1 but the latter requires $\Delta Q = 1$ or 2 ($\Delta Q = 0,1$ occurs frequently but $\Delta Q = 2$ is essentially zero).

The existence of the charge two exchange ($\Delta Q = 2$) particularly in $\bar{p} + p \longrightarrow \Sigma^- + \bar{\Sigma}^-$ is also interesting, as in the new decay mode of the $N_{\frac{1}{2}}^* \longrightarrow \Lambda + K$. The existence of the anticascades and the predictions of charge conjugation have been confirmed.

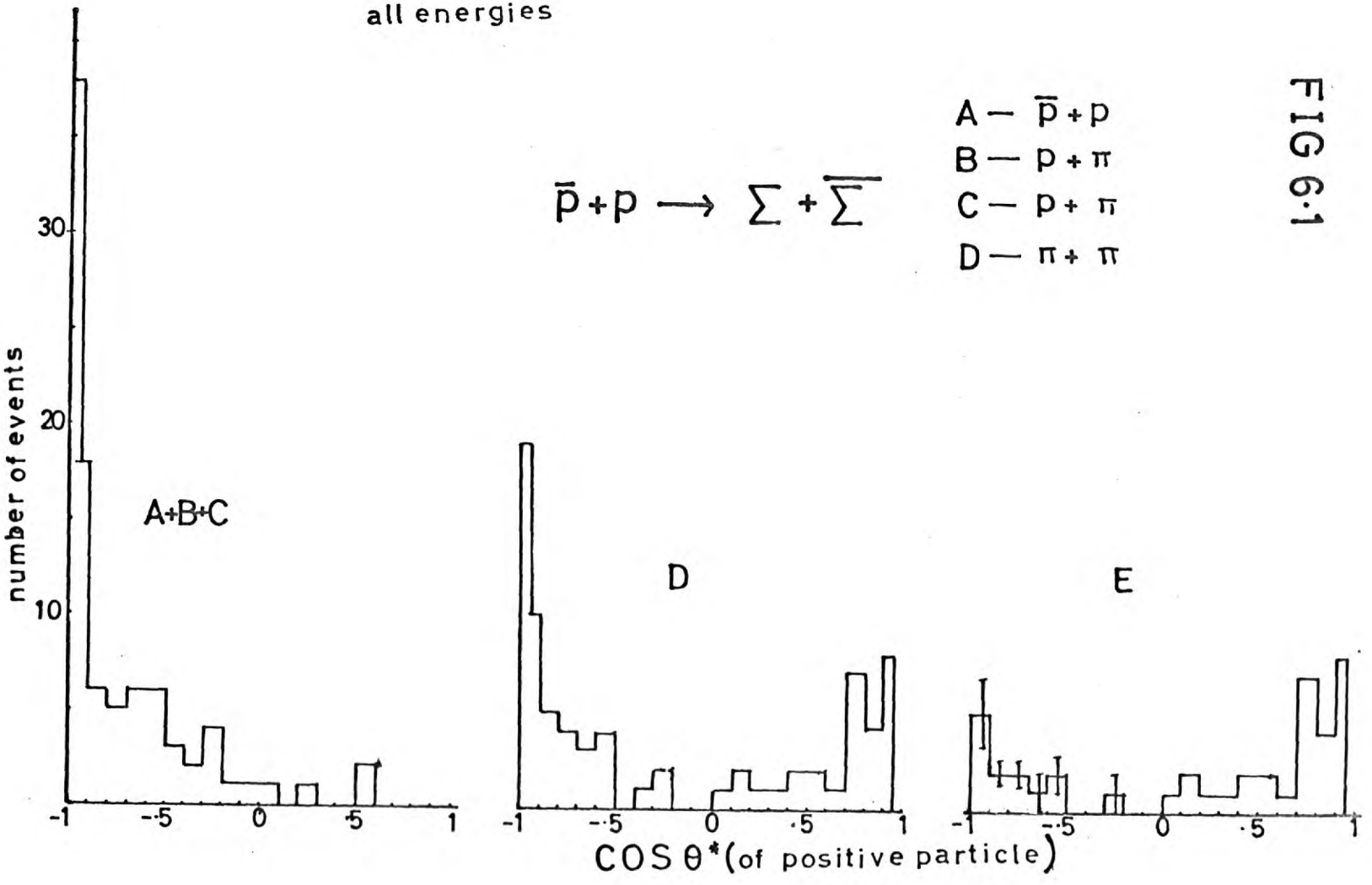
all energies
$\bar{p}+p \longrightarrow \Sigma+\overline{\Sigma}$
A — $\bar{p}+p$
B — $p+\pi$
C — $p+\pi$
D — $\pi+\pi$
number of events
30
20
10
A+B+C
D
E
-1
-.5
0
.5
1
COS θ*(of positive particle)

FIG 6.1

FIG 6·2

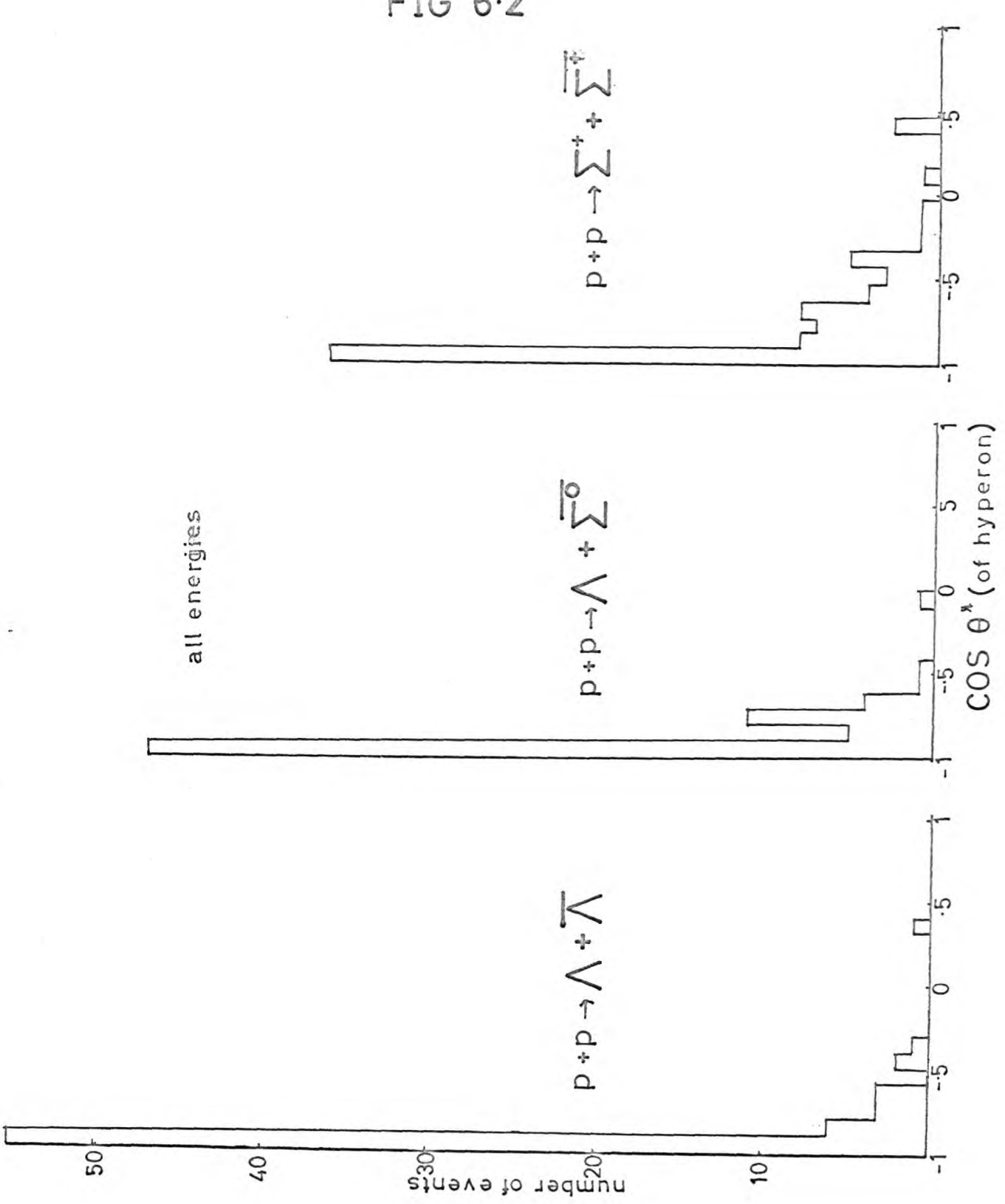
all energies
number of events
50
40
30
20
10
-1
-.5
0
.5
1
COS θ* (of hyperon)
p + p → Λ + K+
p + p → Σ0 + K+
p + p → Σ+ + K0

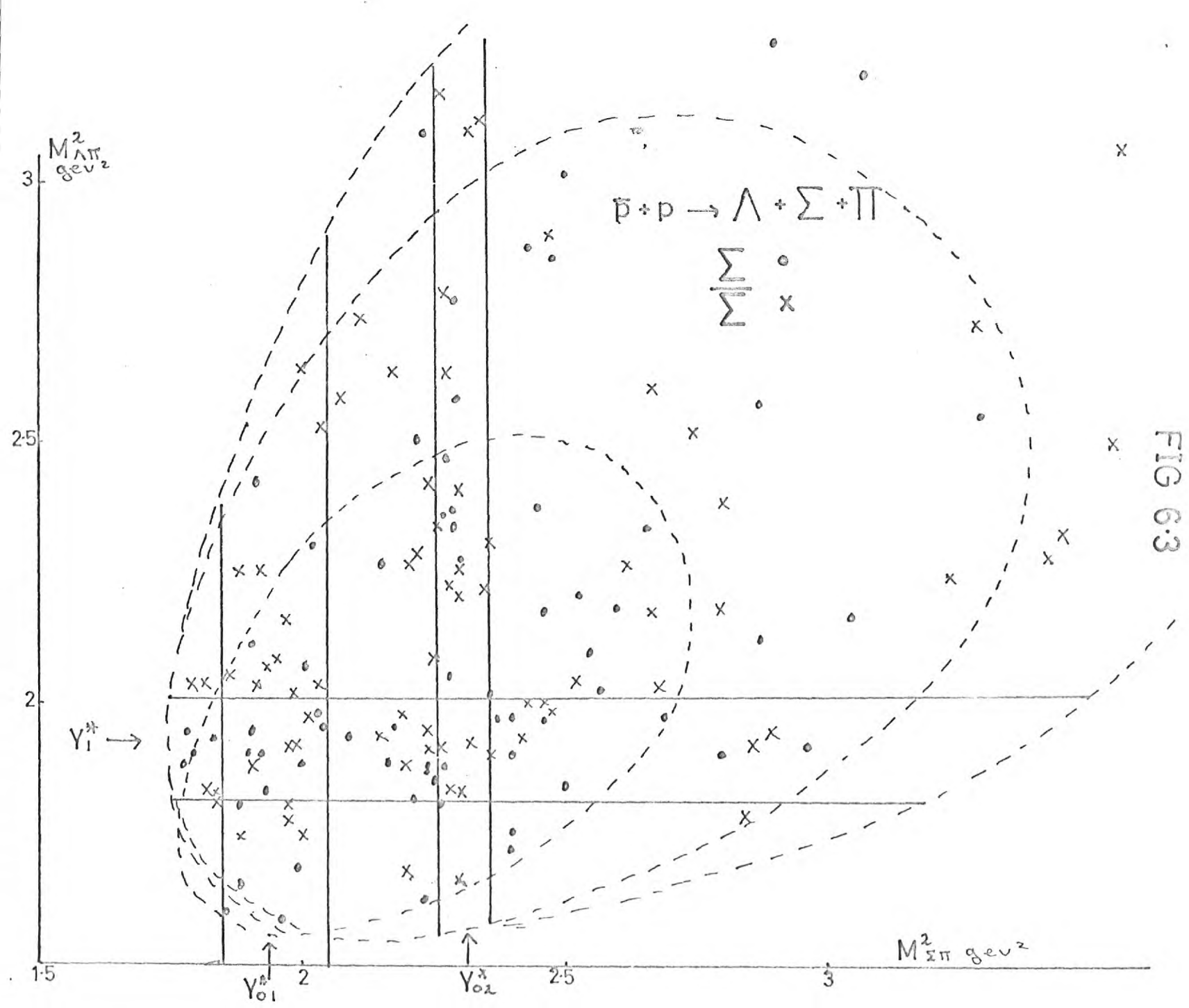
$M^2_{\Lambda\pi}$ gev^2
3
2·5
2
1·5
Y_1^* →
Y_{o1}^*
Y_{o2}^*
2
2·5
3
$M^2_{\Sigma\pi}$ gev^2
$\bar{p} + p \rightarrow \Lambda + \Sigma + \overline{\Pi}$
Σ
$\overline{\Sigma}$

FIG 6.3

FIG 6·4

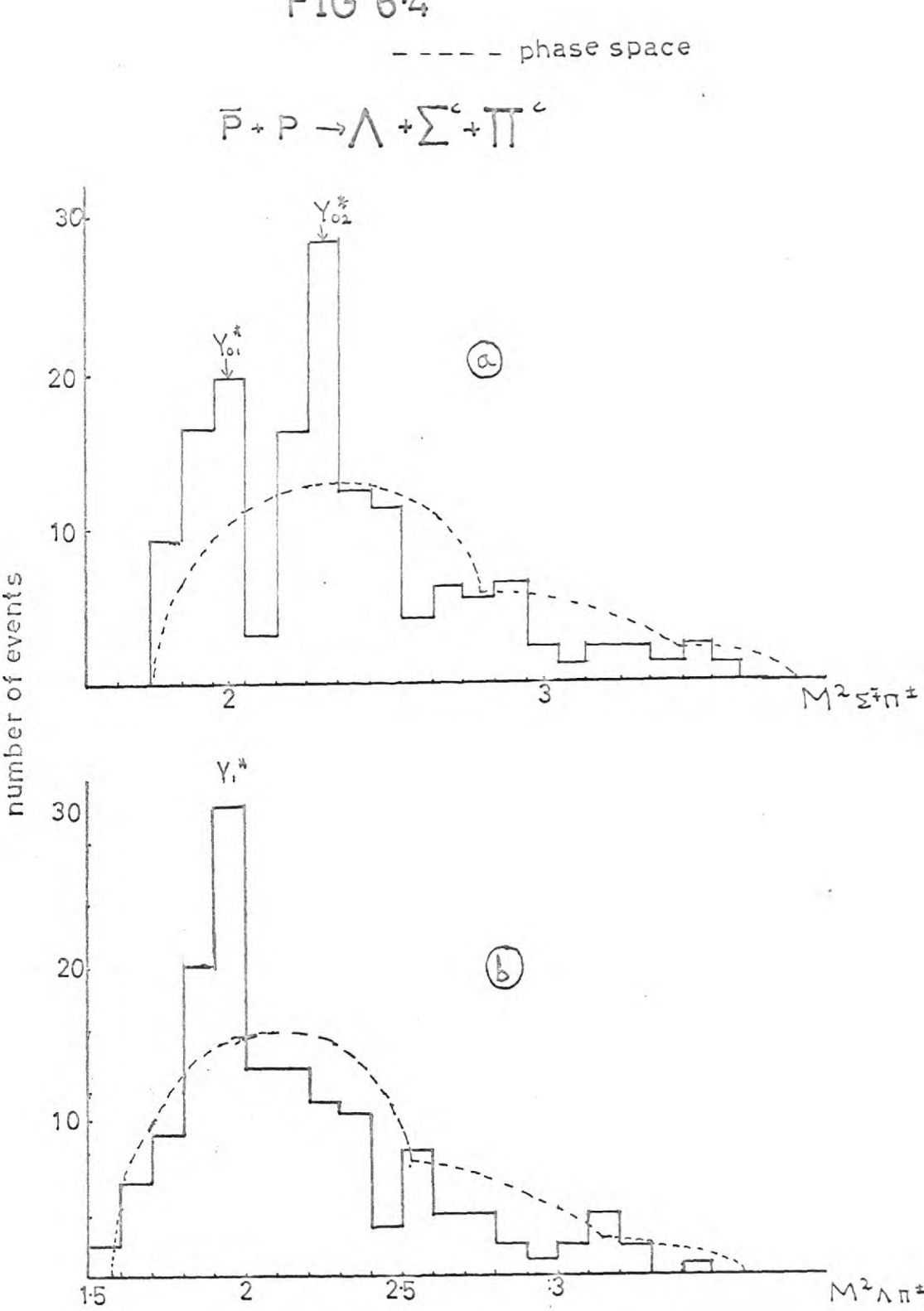
- - - - phase space
$\bar{P} + P \rightarrow \Lambda + \Sigma^{c} + \Pi^{c}$
number of events
30
20
10
Y_{02}^{*}
Y_{01}^{*}
a
2
3
$M^2 \Sigma^{\mp} \pi^{\pm}$
Y_1^{*}
30
20
10
b
1·5
2
2·5
3
$M^2 \Lambda \pi^{\pm}$

FIG 6·5

$\bar{p} + p \rightarrow \Lambda + \Sigma^{\pm} + \pi^{\mp}$

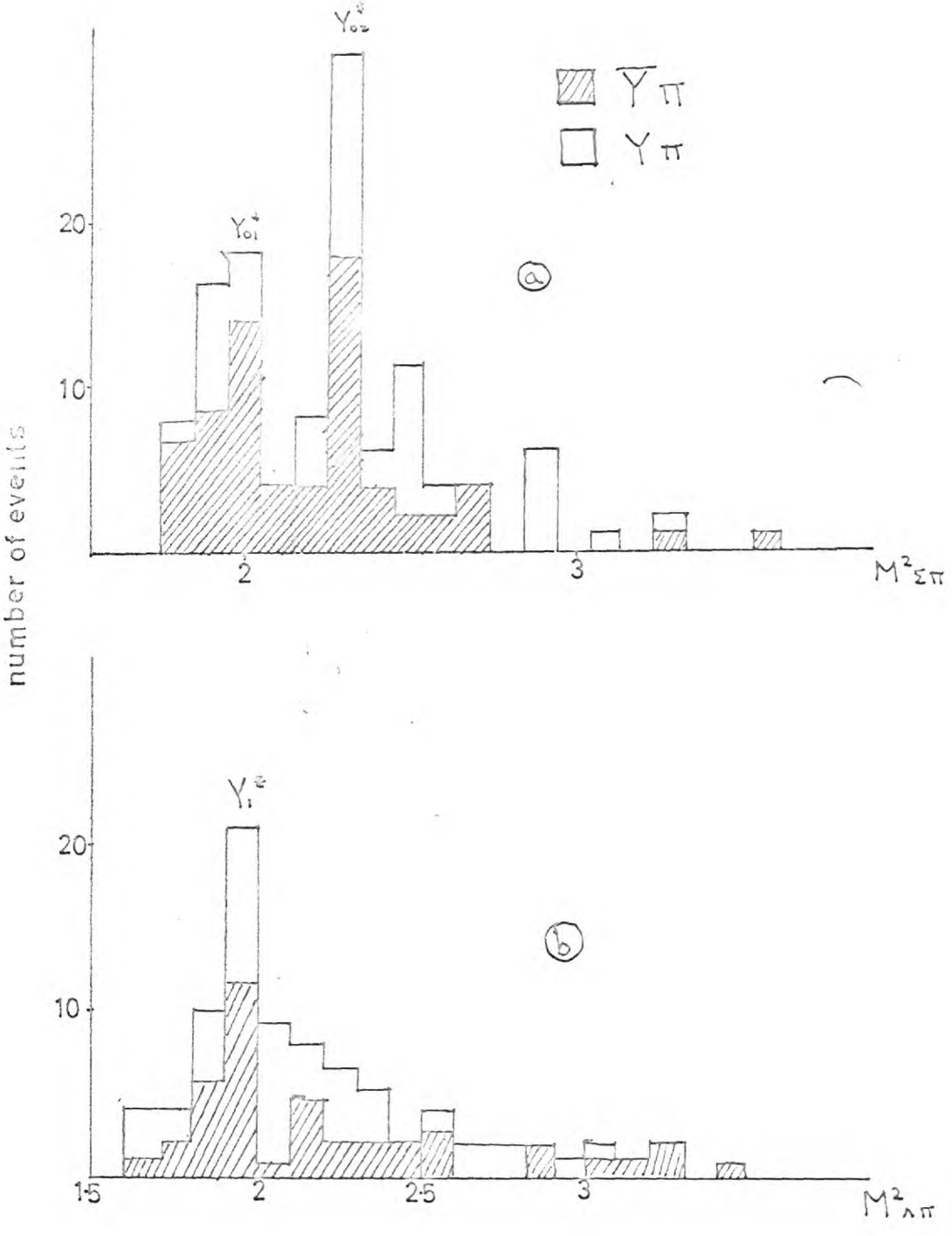

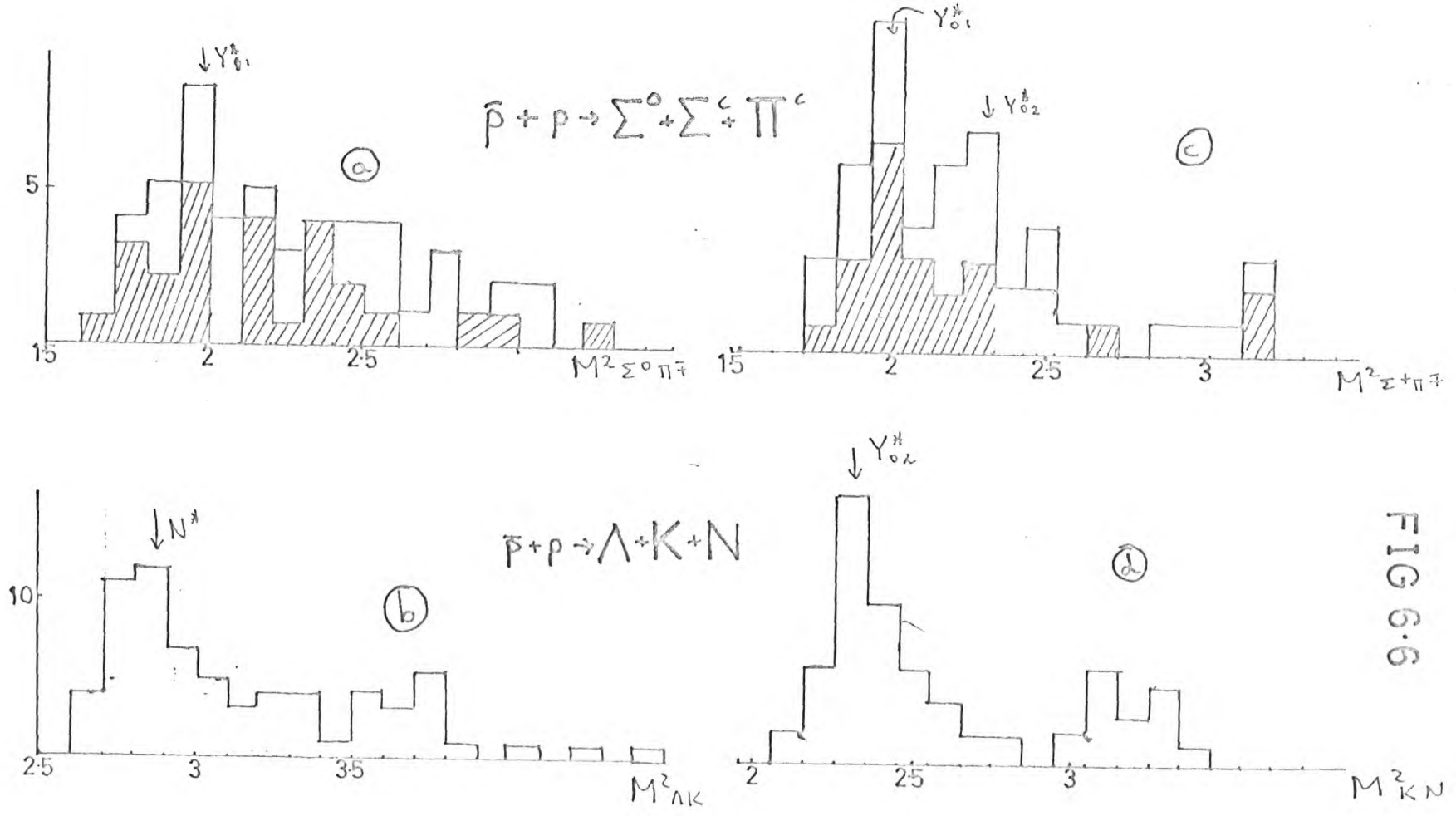
$\bar{p}+p \to \Sigma^0+\Sigma^c+\pi^c$
$\bar{p}+p \to \Lambda+K+N$
Y^*_{01}
Y^*_{02}
$Y^*_{0\Lambda}$
N^*
a
b
c
d
5
10
1·5
2
2·5
3
3·5
$M^2_{\Sigma^0\pi^-}$
$M^2_{\Sigma^+\pi^-}$
$M^2_{\Lambda K}$
M^2_{KN}

FIG 6.6

FIG 6.7

$\bar{p} + p \rightarrow \Lambda + \bar{\Lambda} + \pi^0$
15
10
5
1·5
2
2·5
3
$M^2_{\Lambda\pi^0}$

IN Y_{01}^* (a)
$\bar{p} + p \to \Sigma^0 + \Sigma^c + \Pi^c$
IN Y_{01}^*
(c)
$\bar{p} + p \to \Lambda + \Sigma^c + \Pi^c$
$\cos\theta^* - (\overline{\Sigma^\pm}\,\pi^\pm)$
1 event
$\Delta Q = 1$
IN Y_{02}^* (b)
IN Y_{02}^* (d)
-1
0
+1

FIG 6.8

$\bar{p} + p \to \Lambda + \Sigma^c + \pi^c$
$\Delta Q = 0$
IN Y_1^* (a)
-1
0
+1
$\cos\theta^*_{-(\Lambda\pi^+)}$
1 EVENT
$\Delta Q = 2$
IN Y_1^* (b)
-1
0
+1
$\bar{p} + p \to \Lambda + \bar{\Lambda} + \pi^0$
IN Y_1^* (c)
-1
0
+1
(d)
IN $\bar{N}^*$
-1
0
+1
$\bar{p} + p \to \Lambda + K^c + N^c$
(e)
IN Y^*_{02}
-1
0
+0

FIG 6.9

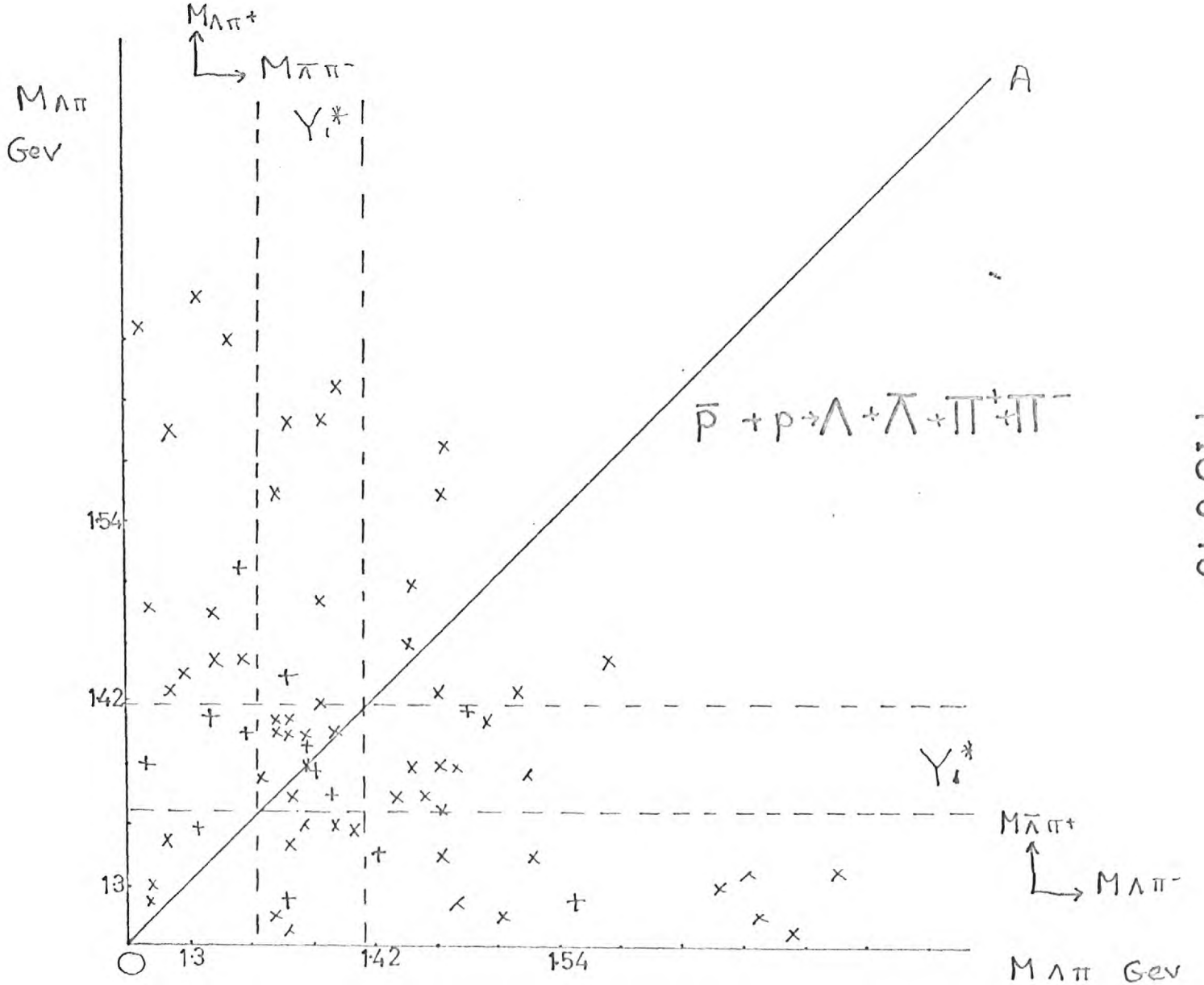
$M_{\Lambda\pi^+}$
$M_{\bar{\pi}\pi^-}$
$M_{\Lambda\pi}$ Gev
Y_1^*
A
$\bar{p} + p \to \Lambda + \bar{\Lambda} + \pi^+ + \pi^-$
1·54
1·42
1·3
Y_1^*
$M_{\bar{\Lambda}\pi^+}$
$M_{\Lambda\pi^-}$
O
1·3
1·42
1·54
$M_{\Lambda\pi}$ Gev

FIG 6·10

FIG 6·11

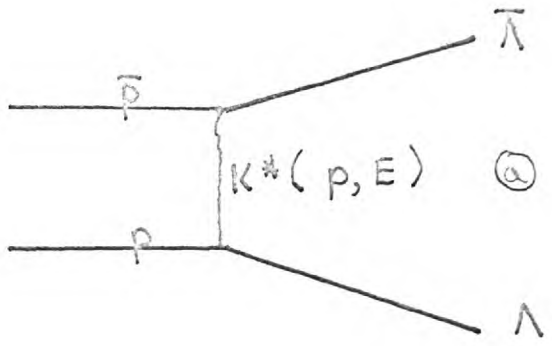
$\bar{\Lambda}$
$\bar{p}$
$K^*(p,E)$ (a)
p
Λ

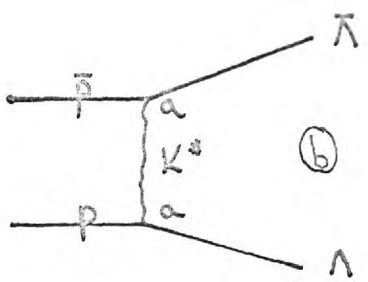
$\bar{\Lambda}$
$\bar{p}$
a
K^* (b)
p
a
Λ

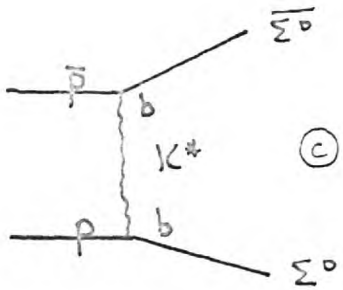
$\bar{\Sigma^0}$
$\bar{p}$
b
K^* (c)
p
b
Σ^0

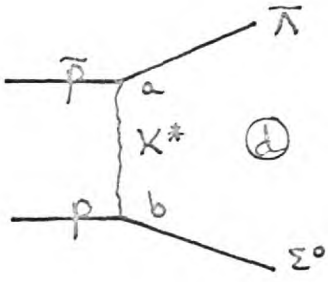
$\bar{\Lambda}$
$\bar{p}$
a
K^* (d)
p
b
Σ^0

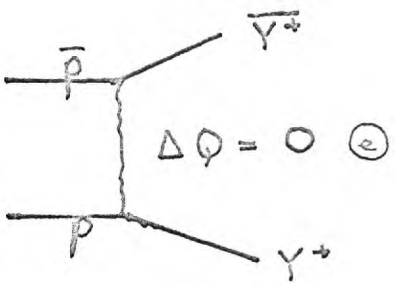
$\bar{Y^+}$
$\bar{p}$
$\Delta Q = 0$ (e)
p
Y^+

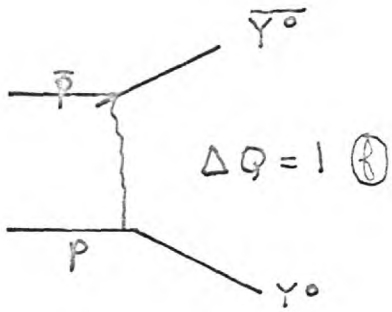
$\bar{Y^0}$
$\bar{p}$
$\Delta Q = 1$ (f)
p
Y^0

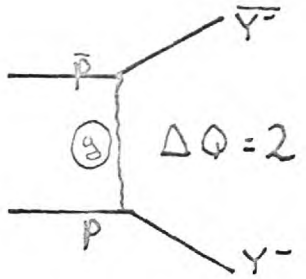
$\bar{Y^-}$
$\bar{p}$
(g) $\Delta Q = 2$
p
Y^-

FIG 6·12

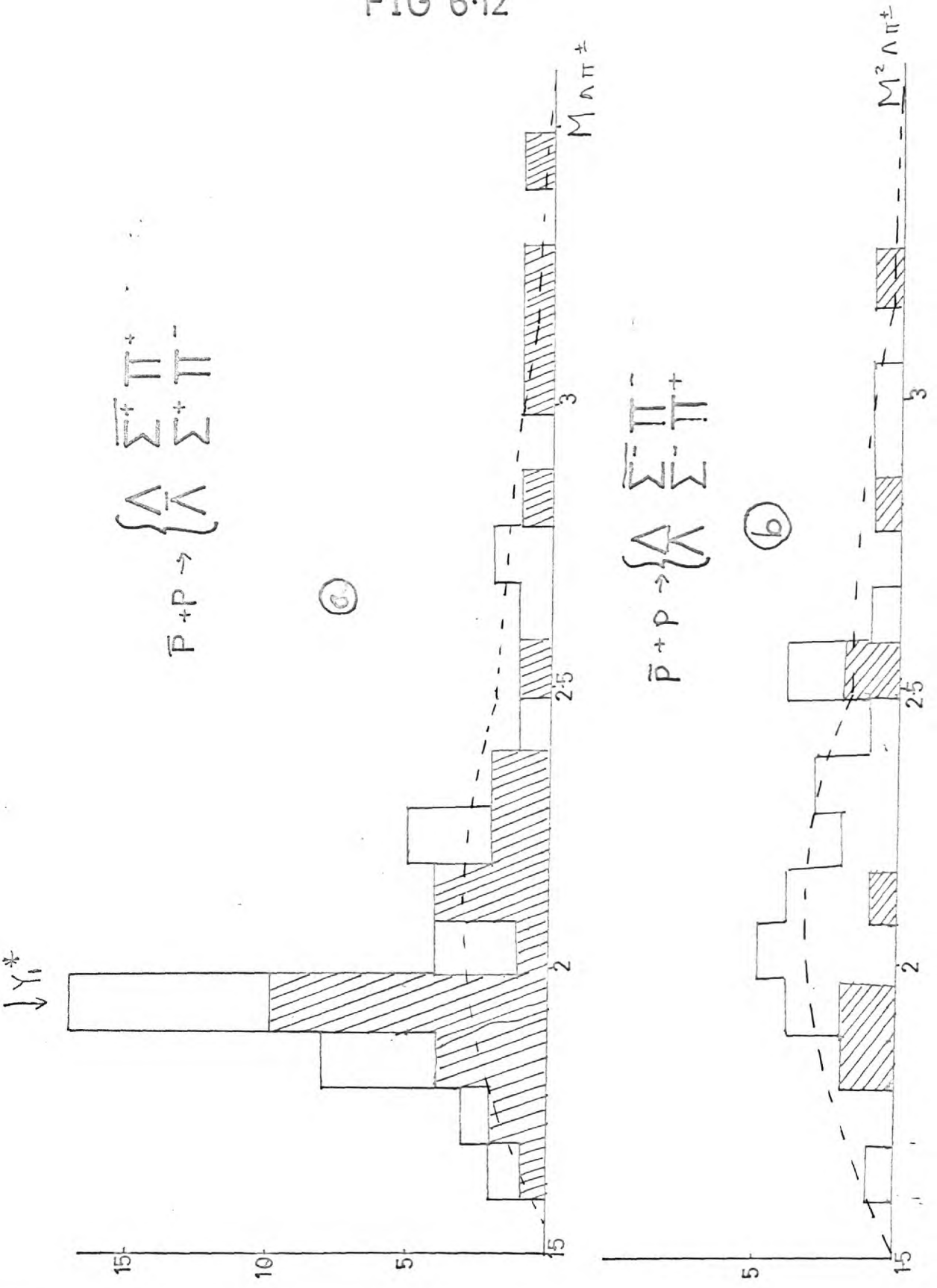
$\bar{p}+p \to \{\bar{\Lambda}\Sigma^+\pi^-, \bar{\Sigma}^+\Sigma^+\pi^-\}$
(a)
$M_{\Lambda\pi^\pm}$
$\downarrow Y_1^*$
$\bar{p}+p \to \{\bar{\Lambda}\Sigma^+\pi^-, \bar{\Sigma}^-\Sigma^+\pi^-\}$
(b)
$M^2_{\Lambda\pi^\pm}$

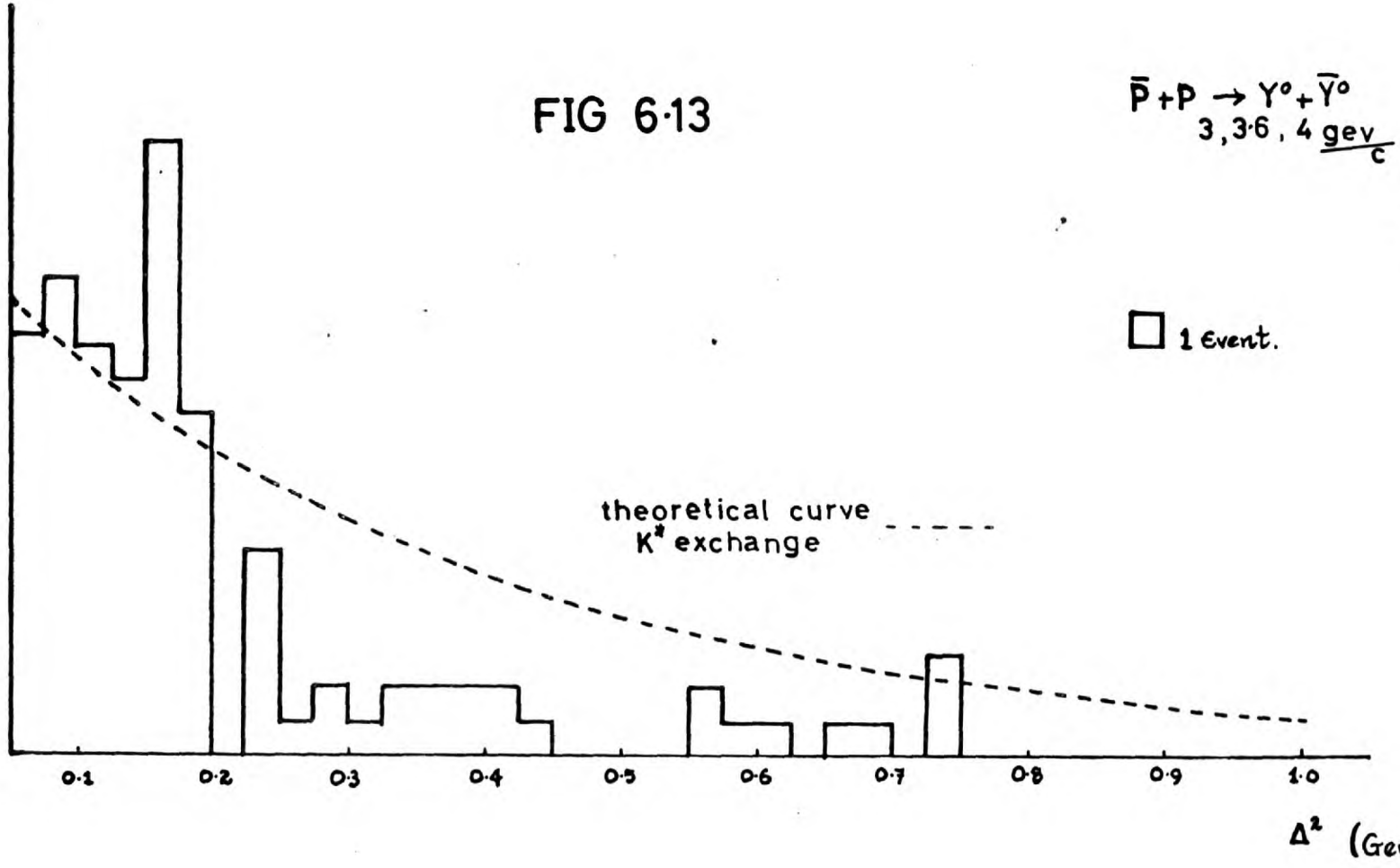
FIG 6·13
$\bar{P}+P \rightarrow Y^0+\bar{Y}^0$
3, 3·6, 4 gev/c
1 event.
theoretical curve
K^* exchange
0·1
0·2
0·3
0·4
0·5
0·6
0·7
0·8
0·9
1·0
Δ^2 (Gev/c)^2

Figure Captions for Chapter 6

6.1 Angular distributions for the reaction $\bar{p} + p \rightarrow \Sigma + \bar{\Sigma}$.

6.2 Angular distribution for the reactions $\bar{p} + p \rightarrow Y + \bar{Y}$.

6.3 Dalitz plots at all three energies for the reactions $\bar{p} + p \rightarrow \Lambda + \Sigma^c + \pi^c$, $M^2_{\Lambda\pi} - M^2_{\Sigma\pi}$.

6.4 Effective mass squareds of the $\Sigma\pi$ and $\Lambda\pi$ systems from the reactions $\bar{p} + p \rightarrow \Lambda + \Sigma^c + \pi^c$.

6.5 (Effective mass)^2 distributions from $\bar{p} + p \rightarrow \bar{\Lambda} + \Sigma^o + \pi^c$ showing the division of hyperon and antihyperon systems.

6.6 (Effective mass)^2 histograms for the reactions $\bar{p} + p \rightarrow \bar{\Sigma}^o + \Sigma^c + \pi^c$ (diagrams (a) and (c)) and $\bar{p} + p \rightarrow \Lambda + K + N$ (diagrams (b) and (d).

6.7 $\Lambda\pi^o$ and $\bar{\Lambda}\pi^o$ (effective mass)^2 histograms from $\bar{p} + p \rightarrow \Lambda + \Lambda + \pi^o$

6.8 Angular distributions within the resonance regions for $\bar{p} + p \rightarrow \Sigma^o + \Sigma^c + \pi^c$ and $\bar{p} + p \rightarrow \Lambda + \Sigma^c + \pi^c$, Cos θ^* for $\bar{\Sigma}^{\mp}\pi^{\pm}$ system is shown in each case.

6.9 Angular distributions of:-

(a) $\bar{\Lambda}\pi$ in Y_1^* region for $\Lambda + \Sigma^c + \pi^c$ $\Delta Q = 0$

(b) $\bar{\Lambda}\pi$ in Y_1^* region for $\Lambda + \Sigma^c + \pi^c$ $\Delta Q = 2$

(c) $\bar{\Lambda}\pi^o$ in Y_1^* region for $\Lambda + \bar{\Lambda} + \pi^o$

(d) $\bar{N}^*$ in $\Lambda + K^c + N^c$.

(e) Y_{02}^* in $\Lambda + K^c + N^c$.

6.10 $M_{(Y\pi)^+} - M_{(Y\bar{\pi})^-}$ from $\bar{p} + p \rightarrow \Lambda + \bar{\Lambda} + \pi^+ + \pi^-$.

6.11 Peripheral diagrams for possible production mechanisms.

6.12 (Effective mass)^2 histograms of $\Lambda\pi$ system for $\Delta Q = 0$ and $\Delta Q = 2$ from $\bar{p} + p \rightarrow \Lambda + \Sigma^c + \pi^c$.

6.13 Δ^2 distribution $\bar{p} + p \rightarrow Y^{o+} \overline{Y^o}$.

In all the above, unless otherwise stated distributions include the charge conjugate reactions. In the case of angular distributions a reflection about $\text{Cos}\,\theta^* = 0$ is made before the charge conjugate reactions are plotted.

APPENDIX 1

Relationships between particles and antiparticles

Property	Particle	Antiparticle
Mass	m	m
Lifetime	τ_o	τ_o
Charge	e	-e
Spin	s	s
Strangeness	S	-S
Magnetic Moment	μ	$-\mu$
Baryon number		opposite
Leptonic number	L	opposite -L
Parity		opposite

APPENDIX 2

Reactions producing hyperon antihyperon pairs, possible in this experiment

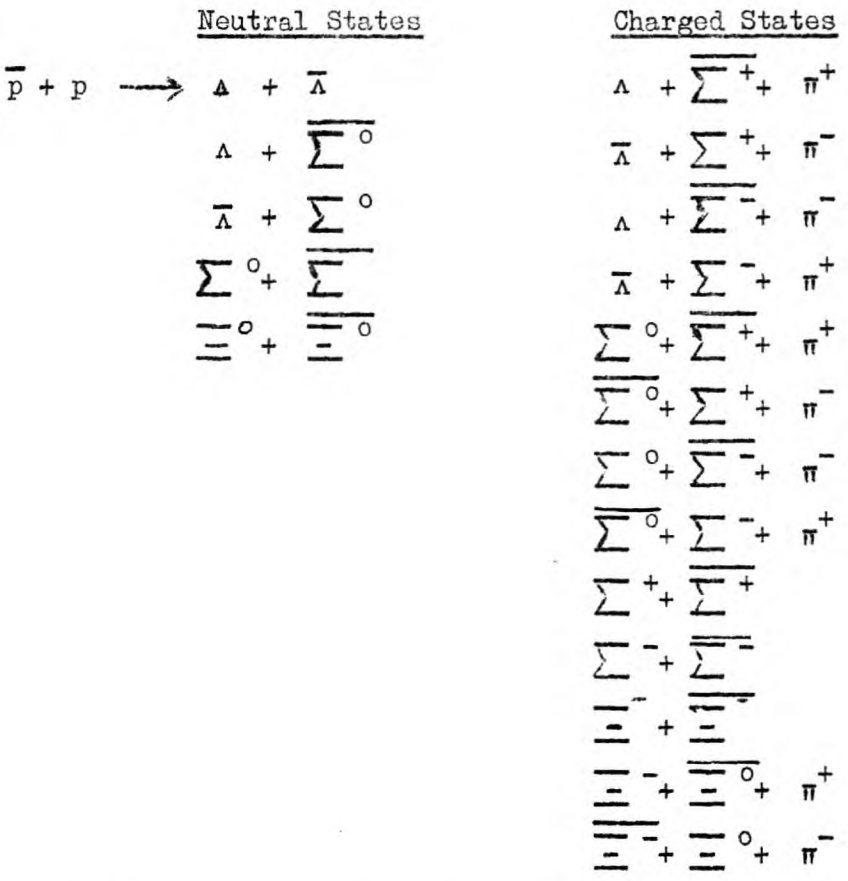

In addition extra pi mesons could be produced in the majority of the above interactions. The available energies at the three momenta being:-

3 Gev/c = 2·77 gev 3·6 Gev/c = 2·97 gev 4 Gev/c = 3·06 gev.

APPENDIX 3

DEFINITIONS OF TERMS USED

The normal units used are shown in each case

M - mass in gev.

E - energy in gev.

P - momentum in gev/c.

τ_o - meanlife in seconds.

β - velocity in units of c.

ρ - radius of curvature centimetres.

λ, ψ - angles of dip and azimuth for a track (radians).

S(s) - Sagitta of a track microns.

H - Magnetic field (kilogauss).

Page 14 y deflection in metres;
e, m, v charge mass and velocity of particle (M.K.S.).
F electric field (M.K.S.).

APPENDIX 4

HYPOTHESES USED IN GRIND

(a) Neutral Decay Λ , $\bar{\Lambda}$, K, γ

(b) Charged Decay Σ , K, $\bar{\Xi}$, $\bar{\pi}$

(c) 001's $\bar{p} + p \longrightarrow \Lambda\bar{\Lambda}$, $\Lambda\bar{\Sigma}^{o}$, $K^{o}K^{o}$

(d) 002's $\Lambda\bar{\Lambda}$, $\Lambda\bar{\Lambda}\pi^{o}$, Λ KN, KK, KK$\bar{\pi}^{o}$

(e) 201's ΛKN, ΛKNπ^{o}, Σ^{o}KN

(f) 202's $\Lambda\bar{\Lambda}\pi^{+}\pi^{-}$, $\Lambda\bar{\Lambda}\pi^{+}\pi^{-}\pi^{o}$, ΛKN π Λ KN $\pi\pi^{o}$

(g) 211's $\Lambda\Sigma\bar{\pi}$, $\Lambda\Sigma\pi\pi^{o}$, $\Sigma^{o}\Sigma\pi$, ΛKN , ΛKNπ, ΣKN,
ΣKNπ^{o} $\bar{\Xi}^{-}$ $\bar{\Xi}^{o}\pi$

(h) 220's $\Sigma\Sigma$, $\Sigma\bar{\Sigma}\pi^{o}$, ΣKN, KK, KK π^{o}.

Charge conjugate reactions were also used as well as testing for $\bar{\pi}^{-}$ interactions.

APPENDIX 5

Parity Conservation

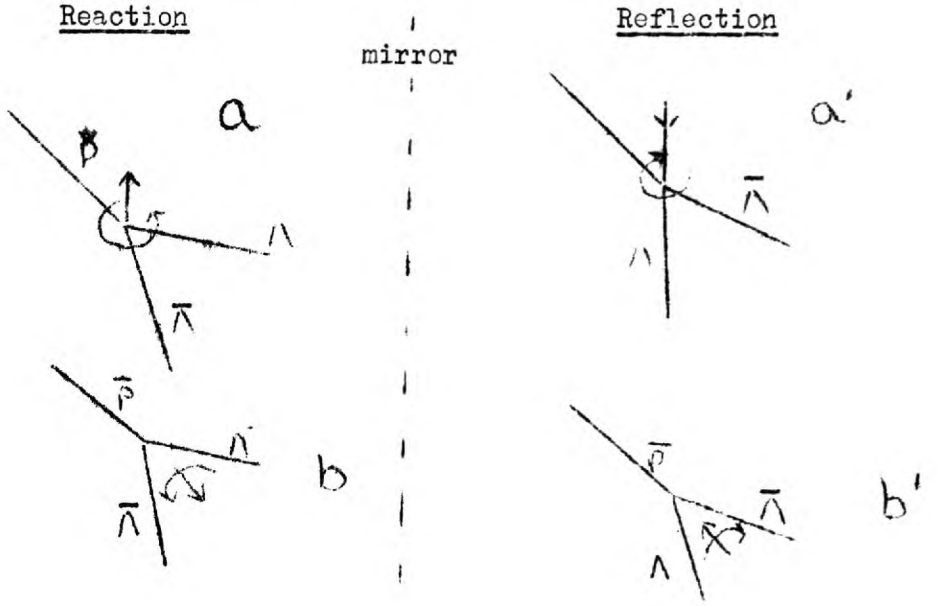

Diagram a shows a production process with a shown polarization vector perpendicular to the plane of production. Its reflection is an identical reaction only having a rotation of 180°.

Diagram b shows a similar reaction with the vector now in the plane. This does not give the same reaction on reflection, i.e. parity is not conserved.

Parity conservation is believed to hold in strong interactions and hence no polarization can be present in the plane of production.

ACKNOWLEDGEMENTS

The author would like to thank Professor P.M.S. Blackett for the opportunity of working in his laboratory and Professor C. C. Butler for his supervision of this work.

The author is very grateful to those who contributed directly to the success of the experiment. The C.E.R.N. organization and members of the collaboration in particular.

Within the Imperial College group the author is particularly grateful to Dr. S. J. Goldsack for his encouragement and constructive criticism. The work done by the other members of the group, especially S. Borenstein is gratefully acknowledged.

The careful and accurate work of the team of technical assistants, in particular Miss M. T. Gough, is also acknowledged.

The author wishes to thank D.S.I.R. for a maintenance grant during the period 1960-63.

REFERENCES

1. Chamberlain et al;
   Physical Review V.100,P.947.
2. Lynch et al;
   Reviews of Modern Physics V.33,P.395.
3. Lindebaum et al;
   Physical Review Letters V.7, P.185.
4. Proceedings of the Rochester Conference 1963 P.69 and P.90.
5. CERN Report 60-22.
6. L'Onde Electrique Vol.XLI No.417, P.1001.
7. TRAMP: A tracking and matching Programme. Internal Report
   National Institute for Nuclear Science, Didcot.
8. Proceedings of the Rochester Conference P.84, (1962).
9. Rossi;
   High Energy Particles.
10. Ritson;
    Techniques of High Energy Physics.
11. H. Sherman;
    Thesis presented for the Degree of Doctor of Philosophy,
    London University, October 1962.
12. CERN Report 60-33.
13. Internal CERN Report; GAP 1 Kernan et al.
14. CERN Report 61-29.
    GRIND MANUAL published at CERN compiled by Boch et al.
15. A.Muller;Private communication (CERN visiting Fellow).
16. Y. S. Liu;
    Thesis presented for the Degree of Doctor of Philosophy,
    London University, 1963.
17. See Reference 14.
18. Crawford et al;
    P. R. L. V.2, P.11.
    Jones et al;
    Proceedings of the Physical Society V.72, P.429.

19. Introduction to Elementary Particles, W. Williams.

20. Barkas and Rosenfeld;
Data for Elementary Particle Physics UCRL.8030.

21. Properties of Dalitz Plots, UCRL Physics Memo 439.

22. P. R. L. V.8,257.

23. P. R. L. V.8, P.255.

24. Baltay et al;
Internal Publication at Brookhaven National Laboratory.

25. Taken from Data on Elementary Physics, UCRL Report 8030.

26. Eberhard et al;
P. R. L. V.10, P.351.

27. E. Ferrari;
P. R. L. 7, P.387.

Proceedings of the Rochester Conference 1962.

28. E. Ferrari et al;
Nuovo Cim. (Suppl.) V.24, P.453.

29. M. Alston et al;
P. R. L. V.6, P.300.

30. Bessis et al;
Nuovo Cim. V.27, P.376.

31. H. Watson;
Hyperon Pair Production, Preprint Imperial College,
Theoretical Group.

32. M. Gell-Mann;
Phys. Rev. V.125, P.1067.

Y. Ne'eman;
Nuclear Phys. V.26, P.222.

33. Goldberg;
$\bar{p} + p \rightarrow B\bar{B}$ reaction, Israel Atomic Energy Commission
Laboratory Preprint.

34. Selleri;
Private Communcation, Centre D'Etudes Nucleaires, Saclay.